ib

Una publicación de:

SOMIB
Sociedad Mexicana
de Ingeniería Biomédica

Revista Mexicana de
Ingeniería Biomédica

New publishing model

Continuous publication:
as soon as an article is prepared,
it will be released online

SOMIB
Sociedad Mexicana de Ingeniería Biomédica

Sociedad Mexicana de Ingeniería Biomédica

La Mesa Directiva de la Sociedad Mexicana de Ingeniería Biomédica hace una extensa invitación a las personas interesadas en participar, colaborar y pertenecer como Socio Activo de la SOMIB. La SOMIB reúne a profesionistas que se desarrollan en áreas de Ingeniería Biomédica, principalmente ingenieros biomédicos, así como otros profesionistas afines con el desarrollo de tecnología para la salud.

Membresía Estudiante
$1,400.00 *PESOS MXN*
15% de descuento para grupos de 5 o más personas.

Membresía Profesionista
$2,400.00 *PESOS MXN*
15% de descuento para grupos de 5 o más personas.

Membresía Institucional
$11,600.00 *PESOS MXN*
No aplica descuento.

Membresía Empresarial
$20,000.00 *PESOS MXN*
No aplica descuento.

EL PAGO CUBRE UN AÑO DE CUOTA. EN CASO DE REQUERIR FACTURA
FAVOR DE SOLICITARLA, ADJUNTANDO COMPROBANTE DE PAGO Y ESPECIFICANDO CONCEPTO,
AL CORREO ELECTRÓNICO: *gerencia@somib.org.mx*

ib Revista Mexicana de Ingeniería Biomédica

AUTORES

Los trabajos a publicar en la RMIB, deben ser originales, inéditos y de excelencia. Los costos de publicación para autores son los siguientes:

NO SOCIOS:	**$200** *DÓLARES AMERICANOS*
SOCIOS:	**$150** *DÓLARES AMERICANOS*

PUBLICIDAD

A las empresas e instituciones interesadas en publicitar su marca o productos en la RMIB, los costos por número son los siguientes:

MEDIA PLANA:	**$4,999.00** *PESOS MXN (INCLUYE I.V.A.)*
UNA PLANA:	**$6,799.00** *PESOS MXN (INCLUYE I.V.A.)*
CONTRAPORTADA:	**$7,799.00** *PESOS MXN (INCLUYE I.V.A.)*
FORROS INTERIORES:	**$7,799.00** *PESOS MXN (INCLUYE I.V.A.)*

DESCUENTO DEL **20%** AL CONTRATAR PUBLICIDAD EN DOS O MÁS NÚMEROS.

Para ser socio

› Realiza el pago de derechos, de acuerdo a la categoría que te corresponde.

› Ingresa a *www.somib.org.mx/ membresias* y elige el tipo de membresía por el cual realizaste el pago de derechos.

› Completa el formulario correspondiente y envíalo.

› Se emitirá carta de aceptación y número de socio por parte de la mesa directiva (aprobada la solicitud).

› Para mayor información sobre beneficios, ingresa a *www.somib.org.mx*; o escribe a *gerencia@somib.org.mx.*

Datos bancarios

› **Beneficiario:** *Sociedad Mexicana de Ingeniería Biomédica A. C.*

› **Banco:** *Scotiabank*

› **Referencia:** *1000000333*

› **Cuenta:** *11006665861*

› **CLABE Interbancaria:** *044770110066658614*

La inserción de la publicidad será publicada en el libro electrónico y en el área de patrocinios en el sitio Web de la revista (RMIB), disponible en:

http://rmib.mx

SOMIB
Sociedad Mexicana de Ingeniería Biomédica

MESA DIRECTIVA

Ing. Francisco Javier Aceves Aldrete
PRESIDENTE

Mtra. Natalia Gabriela Sámano Lira
VICEPRESIDENTA

Mtra. Verónica Guadalupe Castillo Sánchez
TESORERA

Ing. Janetthe Mariana Tarín León
SECRETARÍA GENERAL

Dra. Dora-Luz Flores Gutiérrez
EDITORA DE RMIB

Afiliada a:
International Federation of Medical and Biological Engineering (IFMB-IUPSM-ICSU)
Federación de Sociedades Científicas de México, A.C. (FESOCIME)
Consejo Regional de Ingeniería Biomédica para América Latina (CORAL)

SOMIB
Juan Vázquez de Mella #481, Polanco I Sección, Alc. Miguel Hidalgo, C. P. 11510, Ciudad de México, México (555) 574-4505
www.somib.org.mx

Disponible en línea:
www.rmib.mx

CONTENTS
CONTENIDO

Dora-Luz Flores
EDITOR-IN-CHIEF 2022-2023

EDITOR'S LETTER

Dear readers,

It is a great honor and pleasure to present this issue of the Revista Mexicana de Ingeniería Biomédica (RMIB). This 2022 edition of RMIB brings even more pioneering research content from Mexico and Latin America in the broad area of Biomedical Engineering. Despite continuing to live in a pandemic caused by covid-19, the RMIB continues to show results from the authors who decide to take this journal as their option for publication.

Our primary focus continues to be publishing quality research and review articles that help health professionals to have more tools for decision-making. I thank all the authors who submitted their work and have worked hard to produce and make RMIB their journal of choice. We hope that the RMIB will continue to provide this established field in Mexico and Latin America with an academic and research voice and a venue for discourse that propels us toward continued growth.

We have dedicated a great deal of effort and work to developing this magazine, and I believe that it will be reflected in this edition by the impact it will have in these areas. Like other quality academic journals, I assure you that RMIB uses blind peer review with rigorous evaluation criteria. Our editorial board represents a wide field of knowledge. I am very proud of our board members and am fortunate to harness their broad individual and group judgment, talent, and disciplinary expertise to advance RMIB's worldwide engagement.

I want to take this opportunity to express my gratitude to the editorial board and the editorial office for their collective effort and dedication to the Mexican Journal of Biomedical Engineering. Additionally, on behalf of the RMIB staff, I also thank the Sociedad Mexicana de Ingeniería Biomédica administration for their support of this effort.

ABOUT THE EDITOR-IN-CHIEF
Dora-Luz Flores, PhD
Professor at The Universidad Autónoma de Baja California, Ensenada, Mexico

Revista Mexicana de Ingeniería Biomédica

Detection of COVID-19 Lung Lesions in Computed Tomography Images Using Deep Learning

Detección de lesiones pulmonares por COVID-19 en imágenes de tomografía computarizada mediante aprendizaje profundo

Joy Ingrid Arreola Minjarez ⓘ, *José David Díaz Román* ⓘ, *Boris Jesús Mederos Madrazo* ⓘ, *José Manuel Mejía Muñoz* ⓘ, *Lidia Hortencia Rascón Madrigal* ⓘ, *Juan de Dios Cota Ruiz* ⓘ

Universidad Autónoma de Ciudad Juárez

ABSTRACT

The novel coronavirus (COVID-19) is a disease that mainly affects the lung tissue. The detection of lesions caused by this disease can help to provide an adequate treatment and monitoring its evolution. This research focuses on the binary classification of lung lesions caused by COVID-19 in images of computed tomography (CT) using deep learning. The database used in the experiments comes from two independent repositories, which contains tomographic scans of patients with a positive diagnosis of COVID-19. The output layers of four pre-trained convolutional networks were adapted to the proposed task and re-trained using the fine-tuning technique. The models were validated with test images from the two database's repositories. The model VGG19, considering one of the repositories, showed the best performance with 88% and 90.2% of accuracy and recall, respectively. The model combination using the soft voting technique presented the highest accuracy (84.4%), with a recall of 94.4% employing the data from the other repository. The area under the receiver operating characteristic curve was 0.92 at best. The proposed method based on deep learning represents a valuable tool to automatically classify COVID-19 lesions on CT images and could also be used to assess the extent of lung infection.

Corresponding author

TO: **José David Díaz Román**

INSTITUTION: **Universidad Autónoma de Ciudad Juárez**

ADDRESS: **Av. Plutarco Elías Calles #1210,**
Col. Fovissste Chamizal, C.P. 32310, Ciudad Juárez,
Chihuahua, México

CORREO ELECTRÓNICO: **david.roman@uacj.mx**

INTRODUCTION

Coronavirus disease 2019 (COVID-19) is caused by the severe acute respiratory syndrome coronavirus type 2 (SARS-CoV-2). It primarily affects the human respiratory system and represents the seventh member of the coronavirus family that infects humans [1]. The first case, identified as viral pneumonia until then, appeared in late December 2019 in Wuhan, China. According to the records issued by the World Health Organization, until September 1st, 3,341,264 cases have been registered in Mexico and 217,558,771 around the world [1] [2] [3]. It is known that the COVID-19 infection has an incubation period from 1 to 14 days, which varies depending on some human characteristics like the status of the immune system and the age [1]. In Mexico, coronavirus cases are classified by stages according to their severity, clinical stage and signs presented: stage 1 (early infection), stage 2 (pulmonary stage) and stage 3 (hyperinflammatory stage) [4].

The reverse transcription - polymerase chain reaction (RT-PCR) tests represent the main method to detect COVID-19, providing results with a specificity close to 100% [5]; however, when using this standard test as a reference, some drawbacks must be considered. For example, a low sensitivity (59% - 79%) has been observed during the early phase of the disease [5] [6] [7]. Due to the continuous evolution and genetic diversity that the new coronavirus has presented, the results of clinical tests can be affected by the variation in the viral ribonucleic acid (RNA) sequence [8]. Also, it is import to remark that the diagnostic period can vary from 5 to 72 hours [9].

The study presented by Uysal *et al.* [10] found that 25% of asymptomatic patients, diagnosed with an RT-PCR test, did not show signs of lesions on their computed tomography (CT) scans, while the rest showed abnormal findings associated with lesions similar to those in patients with symptoms. The most common signs were ground glass opacity (GGO), pure or with consolidation or crazy-paving patterns. Thus, due those findings some authors emphasize over the importance of performing RT-PCR tests in conjunction with imaging procedures such as CT to increase the accuracy of the diagnosis, injury identification, and in this way provide an adequate patient management [11].

To confirm the coronavirus disease, the chest CT in conjunction with clinical manifestations and the epidemiological evidence have become a fundamental diagnostic tool. However, discrepancies have been reported between the results of laboratory tests and the characteristics observed in diagnostic images [12].

Recently, some studies have shown that the CT scan of patients (asymptomatic or those in whom the result of RT-PCR test was negative) depicts abnormal signs that can be useful for the disease detection, where these studies have reported a sensitivity between 88% and 98% [5] [6] [13] [14]. The advantage of CT diagnosis lies in its short exploration time and the high resolution of the acquired image, useful for detecting and classifying lung lesions.

At present, most of the expert researchers in the clinical applications of Artificial Intelligence (AI) have focused on the diagnosis of patients with COVID-19 through the processing of medical images, addressing the analysis of findings observed in chest x-rays and/or CT scans [15] [16]. There are several approaches that aim to take advantage of machine learning (ML), especially deep learning, to diagnose CT scans using binary pathway convolutional neural networks (CNN) (positive vs. negative) or multiple classification (healthy vs. COVID-19 versus other types of pneumonia) [16]. An example of this is the COVNet architecture performed by Li *et al.*, which classifies positive results for COVID-19, community acquired pneumonia or negative for any lung disease through a three-dimensional CNN constituted by the ResNet50 architecture, resulting in 90% of sensitivity and a specificity of 96% [17]. Similarly, Yang *et al.* in [13], built a publicly available database of

CT scans of COVID-19 patients that could be used to train deep learning models. This database was subsequently used to develop an algorithm to classify COVID-19 patients in a binary way, obtaining an accuracy of 83% and an area under the receiver operating characteristic curve (AUC-ROC) of 0.95. Other work that uses deep learning techniques developed a model called CTnet-10 obtaining an accuracy of 82.1%. The authors also tested models such as DenseNet169, VGG16, ResNet50, InceptionV3 and VGG19, obtaining an accuracy of 94.52% with the latest network [18]. On the other hand, in [19] the authors attempted to segment lung lesions associated with COVID-19, reaching specificity values of up to 100% in specific tasks and models tested, but with a very low sensitivity (between 1.2% and 64.8%).

As mentioned before, a large percentage of asymptomatic patients already have abnormal findings on their CT scan images whose lesion patterns are similar to those found in symptomatic patients. In this sense, it is very important to detect these patterns in CT images to allow physicians to know if a patient has lung lesions and thus guide their treatment.

The purpose of this investigation is to detect the presence or absence (i.e., a binary classification) of lung lesions due to COVID-19 in images originated from chest CT studies using deep learning. It could be useful when it is desired to identify whether the lesions are disseminated in a large part of the lung tissue, indicating that the lesions occur in many slices of the CT study; this detection can even be valuable in assessing the evolution of lung tissue damage, and thus provide adequate treatment to the patients.

MATERIALS AND METHODS

The database used in this research corresponds to "COVID-19 CT Lung and Infection Segmentation Dataset" [20]. The images are in NIfTI (Neuroimaging Informatics Technology Initiative) format and were prepared through the collection of 20 public CT scans of patients with COVID-19 belonging to the Coronacases Initiative and Radiopaedia repositories. All cases present COVID-19 infection in the lungs; however, the percentage of slices per patient showing abnormal findings (related to infection) ranges from 0.01% to 59%. Abnormal findings on the chest CTs are: GGO, lung consolidation, pleural effusion, and mixed GGO with crazy-paving pattern or consolidation.

Figure 1 shows different patterns of abnormal findings present in the images of the database: a) GGO, b) consolidation, c) pleural effusion, d) GGO with crazy-paving pattern, and e) GGO with consolidation, where GGO is indicated with green arrows, consolidation is surrounded by segmented red ovals, pleural effusion is pointed with a yellow arrow, and crazy-paving pattern is enclosed by a blue line (also indicated by the blue arrow). In Figure 1, the images (a, b, c) belong to the Coronacases Initiative repository, and the images (d, e) correspond to the Radiopaedia repository.
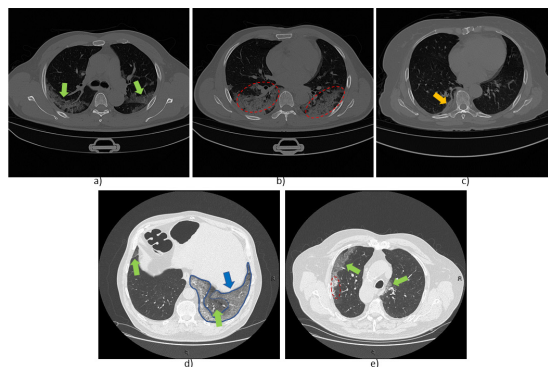
FIGURE 1. **Images with different abnormal findings from CT scans of the database. GGO is indicated with green arrows in a), d) and e); consolidation is enclosed by segmented red ovals in b) and e); pleural effusion is indicated with yellow arrow in c); and crazy-paving pattern is enclosed by a blue line in d).**

There are images that present inconspicuous abnormalities that could be challenging for both an inexperienced radiologist and an automatic detection model.

For instance, Figure 2 shows an example of two images from a CT scan of the same patient. The slice in a) shows slight evidence of GGO, while in b) no abnormalities or lesions are observed. Thus, the detection system must be able to identify negligible lesions that commonly appear at the early stage of the disease.
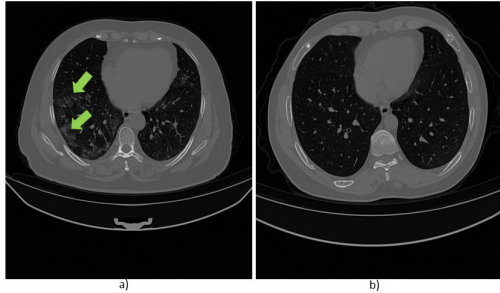
FIGURE 2. Images obtained from a CT scan of a patient of the database. a) Slice with lesion (GGO indicated with green arrows), b) slice without lesion.

The resolution for the x and y axes is 512x512 pixels for the scans obtained from the Coronacases Initiative repository and 630x630 pixels for the Radiopaedia repository, except for case 5 "radiopaedia_14_85914_0" with 630x401 pixels. The CT scans have between 39 and 418 slices, with a total of 3,520 images. The database was grouped by counting images with lesions due to COVID-19 infection and without lesions, obtaining a total of 1,844 and 1,676, respectively.

The database of 20 patient scans was divided into training (80%, N = 16) and test (20%, N = 4) sets. The data were partitioned in such a way that there were the same number of cases from the Coronacases Initiative and Radiopaedia repositories in the training and test sets. The total of images (slices) was 3020 for training and 500 for testing. The purpose of this division was to have a balanced number of images between slices with and without lesions in both sets. A 15% (N = 483) of the training data was considered for internal validation during the training phase of the models used. Table 1 shows the division of the data set into subsets: training, validation, and testing.

TABLE 1. Number of images for the training, validation, and test subsets (Coronacases + Radiopaedia repositories).

Images	With lesions	Without lesions	Total
Training	1339	1198	2537
Internal validation	255	228	483
Test	250	250	500
Total	1844	1676	3520

The CT volumes belonging to the Radiopaedia database were previously pre-processed with a pulmonary window [-1250, 250] HU [19]. The image format was converted from NIfTI to 8-bit grayscale png (Portable Network Graphics). The pixel values were normalized from [0-255] to [0-1]. After normalization, a resizing was applied to finally have images of size 128x128 pixels (or 331x331 in the case of one of the networks used).

Implementation of convolutional neural networks

The algorithm was developed in Python. The implementation of the network models was carried out by means of transfer learning and subsequent fine-tuning. Transfer learning is a technique that takes advantage of existing knowledge to solve problems from a source domain to a destination domain in which, although the same task is not performed, both tasks have a certain similarity. Thus, the purpose is to solve a learning problem using the knowledge acquired by solving similar tasks [21]. On the other hand, the fine-tuning process applied in the context of deep learning model training is a way of applying learning transfer, but especially it consists of fine-tuning the weights of the pretrained model to fit to new observations. Transfer learning and fine-tuning techniques have been used in other investigations to identify and / or differentiate patients with COVID-19 from patients without pulmonary pathology or with pneumonia using chest x-ray images, where this methodology has

Model	Acc (%)	RE (%)	SP (%)	F1 (%)	ROC
RN50	70.8	77.6	64.0	72.7	0.749
RN50 + F-T	68.5	72	64.8	69.5	0.733
VGG16	**79.6**	**93.6**	63.6	**81.4**	**0.880**
VGG16 + F-T	74.8	84.6	68.1	76.4	0.861
VGG16 + F-T/SGD	77.4	86.0	68.8	79.2	0.872
IRNV2	79.0	77.6	**80.4**	78.7	0.862
IRNV2 + F-T	76.6	81.6	71.6	77.7	0.826
NNL	73.0	78.0	68.0	74.3	0.818
NNL +	73.0	84.6	72.4	78.0	0.822
Hard Voting	78.0	84.0	72.0	79.2	--
Soft Voting	78.6	84.4	72.8	79.8	0.867

provided accuracy values between 89% and 99% [22] [23] [24]. Also, Perumal *et al.* used the learning transfer technique with pre-trained models of the ResNet50, VGG16 and InceptionV3 networks to differentiate patients with COVID-19, viral and bacterial pneumonia, and healthy patients. In their models, they combined CT images and chest x-ray images where the best performance was achieved with the VGG16 model with an accuracy of 93% [25].

In this work, the transfer learning technique was implemented using four pretrained models belonging to the following networks: ResNet50 (RN50) [26], VGG16 [27], InceptionResNetV2 (IRNV2) [28], and NASNetLarge (NNL) [29]. These networks were chosen due the well performance in large scale image recognition tasks, and their architectures and weights of pretrained networks are publicly available. Likewise, these networks have been used in numerous medical image classification applications [18] [22] [23] [24] [30]. For each of these networks, they employed weights obtained from training using data from the ImageNet repository [31]. ImageNet corresponds to a dataset widely used for object recognition purposes. Figure 3 shows the general configuration of the architectures used for the construction of each model. The last fully connected layer from each base model (used for ImageNet data classification) was excluded, and the top of the architecture was configured to classify only two classes as follows: An average subsampling layer (GlobalAveragePooling2D) was included, followed by a fully connected dense layer (Dense) of size 1024 with a ReLu activation function and, finally, a Dense layer with two neurons (one for each class) with a Softmax activation function. The input dimension was set to 128x128 pixels, except for the IRNV2 architecture that used 331x331 pixels.

Initially, only the last added Dense layers of each model (the layers enclosed in the red segmented box in Figure 3) were trained for 100 epochs using the ADAM optimizer with a learning rate of 0.001. The

categorical crossentropy loss was used as cost function. The weights of the trained models were saved for testing and subsequent training.
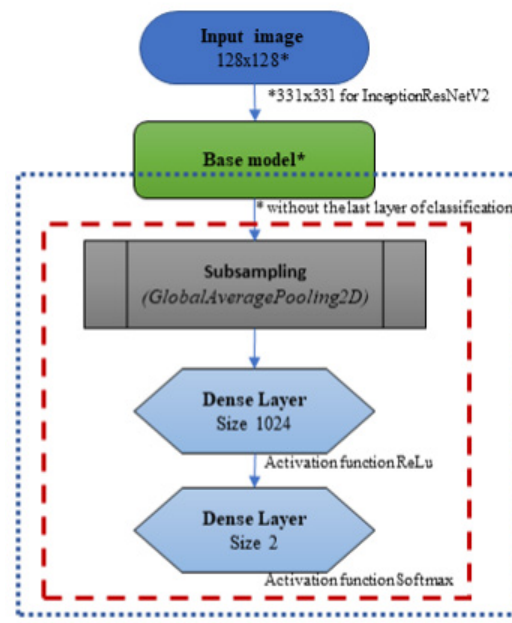
FIGURE 3. **General diagram of the architecture of the models used in the training process**.

Once the training process considering the last layers of the models was carried out, the fine-tuning (F-T) technique was applied, unfreezing a certain number of layers at the end of the base model (of each network) for training together with the layers trained in the previous stage; In Figure 3, the layers enclosed by the dotted blue box are those involved in the fine-tuning of the models. For the RN50 architecture, the layers were unfrozen from the fifth convolutional block onwards; for the VGG16, the unfrozen of the layers started from the fourth block; in the IRNV2, it started from the layer 547th; and in the NNL architecture, it started from the layer 902nd. For training with F-T, the learning rate of the optimizer was decreased to 0.0001 using the ADAM optimizer. In summary, eighth models were built, two for each network (models without and with F-T). Also, with the goal to observe the effect caused by a different optimizer in the learning process, the stochastic descending gradient (SGD) opti-

mizer was applied to the VGG16 network during the fine-tuning phase. Finally, the models were evaluated using five metrics: accuracy (Acc), recall (RE), specificity (SP), F1-Score (F1) and AUC-ROC.

Majority voting ensemble

In terms of classification, majority voting (hard voting) is an ensemble machine learning model that combines the predictions of multiple models. It seeks to optimize the performance of the classification based on consensus, which takes into account the sum of the votes of independent models. The hard voting ensemble used the five models that had the highest accuracy in the validation set: RN50, VGG16, IRNV2, IRNV2 with fine-tuning and NNL without fine-tuning.

A variant of the hard voting arrangement is the ensemble of soft voting, which seeks to get a classification based on the probability values of belonging to a class given by the classifiers used. The labeling (0 or 1) is done after all the probabilities of the models have been considered. The models used for this ensemble are the same as those ones used in the hard voting scheme.

Creation and evaluation of models with separate data repositories

As an additional experimentation, the division of the data by sources (Coronacases Initiative and Radiopaedia repositories) was proposed in order to assess the performance when evaluating the models with the data from the repositories separately. For these tests, both repositories were inspected with the intention of finding and removing low-quality images. In this process, 77 slices with high opacity were excluded, possibly due to an inadequate reconstruction of the tomographic image. Finally, there were 3443 images where 2504 belong to Coronacases and 939 to Radiopaedia. The organization of the training and test sets for the case of Coronacases consisted of using eight scans (2,080 slices) and two scans (424 slices) for training and testing, respectively. In the case of Radiopaedia, seven scans were used for training (792 slices) and three for testing (147 slices). For both cases, 15% of the training data was considered for internal validation. Tables 2 and 3 specify the number of cases, training, validation and testing of the models with the separate data repositories.

Images	With lesions	Without lesions	Total
Training	921	847	1768
Internal validation	162	150	312
Test	205	219	424
Total	1288	1216	2504

TABLE 2. Number of images for the training, validation, and test subsets for the Coronacases repository.

Images	With lesions	Without lesions	Total
Training	367	319	686
Internal validation	54	52	106
Test	72	75	147
Total	493	446	939

TABLE 3. Number of images for the training, validation, and test subsets for the Radiopaedia repository.

The same criteria (the five models that had the highest accuracy in the validation set) were used in the selection of models for the hard voting and soft voting ensembles. For Coronacases, the best models were RN50, VGG16, VGG16 with fine-tune, IRNV2 with fine-tune and NNL. In the case of Radiopaedia, RN50, IRNV2, NNL, VGG16 (all the above with fine-tune) and VGG16 with fine-tune and the SGD optimizer were used.

RESULTS AND DISCUSSION

Table 4 shows the performance of the trained architectures in their different stages (without and with F-T). They were evaluated with the test set of the "COVID-19 CT Lung and Infection Segmentation" data-

Model	Acc (%)	RE (%)	SP (%)	F1 (%)	AUC-ROC
RN50 + F-T	66.8	72.6	64.8	68.5	0.718
RN50	68.5	72	64.8	69.3	0.739
VGG16	79.6	93.6	65.6	81.4	0.860
VGG16 + F-T/SGD	74.8	86.6	68.0	76.2	0.862
VGG16 + F-T/SGD	79.4	77.6	80.4	78.2	0.862
IRNV2 + F-T			81.6		0.826
IRNV2	76.8	86.0			0.808
NNL	73.0	78.6	68.0	74.9	0.848
NNL + F-T	78.0	84.6	72.4	78.9	0.822
Hard Voting	78.8	84.9	72.8	79.3	0.867
Soft Voting	78.6	84.4	72.8	79.8	0.867

Images	With lesions	Without lesions	Total
Training	921	847	1768
Internal validation	162	150	312
Test	205	219	424
Total	1288	1216	2504

base (including both repositories). It is observed that the VGG16 architecture presents the highest values of accuracy and recall, however, the specificity metric is slightly lower than other models, and the Inception-ResNetV2 network presents the best performance in this metric. The VGG16 model has the highest F1-score value above 81%, followed by the model implemented with soft voting. The highest value of the AUC-ROC (0.880) is also obtained by the VGG16 model.

Images	With lesions	Without lesions	Total
Training	354	312	666
Internal validation	67	59	126
Test	72	75	147
Total	493	446	939

TABLE 4. Performance of the models evaluated with the test set (Coronacases + Radiopaedia), where the best performances of the models are bold remarked.

Model	Acc (%)	RE (%)	SP (%)	F1 (%)	AUC-ROC
RN50	70.8	77.6	64.0	72.7	0.749
RN50 + F-T	68.5	72	64.8	69.5	0.733
VGG16	**79.6**	**93.6**	63.6	**81.4**	**0.880**
VGG16 + F-T	74.8	81.6	68.0	76.4	0.863
VGG16 + F-T/SGD	77.4	86.0	68.8	79.2	0.872
IRNV2	79.0	77.6	**80.4**	78.7	0.862
IRNV2 + F-T	76.6	81.6	71.6	77.7	0.826
NNL	73.0	78.0	68.0	74.3	0.818
NNL + F-T	77.0	81.6	72.4	78.0	0.822
Hard Voting	78.0	84.0	72.0	79.2	--
Soft Voting	78.6	84.4	72.8	79.8	0.867

A good classification of CT slices with COVID-19 lesions is observed, with an accuracy equal to or greater than 78% in four of the nine models evaluated. It is also important to mention that only one of the models presents a SP greater than 80%, which indicates that in most models, there is a tendency to misclassify the negative class (images without lesions).

Figure 4 shows the accuracy performance of the nine models, which were trained with the training set (that includes data from both repositories) but evaluated with the test sets of each repository independently. For purposes of better identification, data from the Coronacases Initiative repository is named as DB1 and data from Radiopaedia named as DB2. As it is observed in Figure 4, the accuracy in the classification of the DB1 images was superior in six of the nine models evaluated.
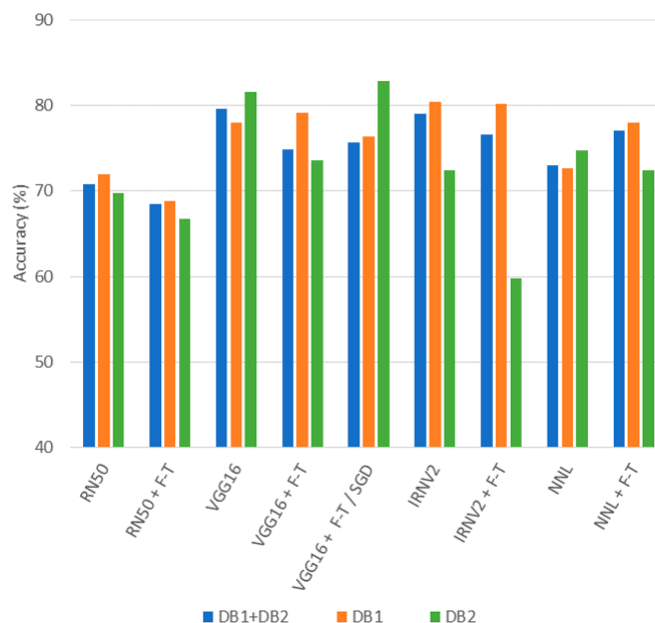
FIGURE 4. Accuracy of the models evaluated with a mixed set of data (DB1+DB2), and independent data sets (DB1 and DB2).

It can be observed from Figure 4 that the models do not show a consistent fit to the data from both repositories separately; this may be due to the lung window preprocessing previously applied to the images of the Radiopaedia repository.

Table 5 presents the performance evaluation of the models trained only using data from the Coronacases repository. The VGG16 architecture (without F-T) shows the best performance with 88% of accuracy, 90.2% of recall, a specificity greater than 85% and an F1-score above 87% (AUC-ROC of 0.929). The IRNV2 + F-T network presents a good assessment in all the metrics evaluated, just below, in average, to the VGG16

model. On the other hand, even though the ResNet50 network obtains an excellent recall of 98.5%, its specificity is around 57% making it unreliable to classify cases without lesions.

TABLE 5. Evaluation of the models with data from the Coronacases Initiative repository.

Model	Acc (%)	RE (%)	SP (%)	F1 (%)	AUC-ROC
RN50	77.4	**98.5**	57.5	80.8	0.912
RN50 + F-T	76.4	86.8	66.7	78.0	0.806
VGG16	**88.0**	90.2	**85.8**	**87.8**	0.929
VGG16 + F-T	80.4	93.7	68.0	82.3	**0.936**
VGG16 + F-T/SGD	80.2	96.6	64.8	82.5	0.925
IRNV2	75.9	69.3	82.2	73.6	0.861
IRNV2 + F-T	85.9	92.7	79.5	86.4	0.899
NNL	75.7	87.8	64.4	77.8	0.871
NNL + F-T	65.1	60.0	69.9	62.4	0.782
Hard Voting	81.6	93.7	70.3	83.1	--
Soft Voting	80.2	92.7	68.5	81.9	0.925

Finally, Table 6 shows the performance evaluation of the models trained only using data from the Radiopaedia repository. As observed, the model built with the soft voting ensemble presents the best performance, reaching an accuracy of 84.4%, a high recall of 94.4% and the highest F1-score of 85.5%, with moderate specificity higher than 74%. The models VGG16 and VGG16+F-T (using the ADAM optimizer), obtain the greatest specificity compared with the rest of the networks; however, they present a low recall making such models not appropriate to detect cases with lung lesions in CT images.

In general terms, training and testing with separated data repositories show a better performance in the models evaluated in this study, which is evidenced by the maximum accuracy values obtained with the Coronacases repository (88% in the VGG16 model), and Radiopaedia repository (84.4% in the soft voting model) when compared with the models trained using data from both repositories together (79.6% for the VGG16 model).

TABLE 6. Evaluation of the models using data from the Radiopaedia repository.

Model	Acc (%)	RE (%)	SP (%)	F1 (%)	AUC-ROC
RN50	73.5	91.7	56.0	77.2	0.873
RN50 + F-T	79.6	87.5	72.0	80.8	0.914
VGG16	78.2	66.7	**89.3**	75.0	0.892
VGG16 + F-T	80.3	73.6	86.6	78.5	0.883
VGG16 + F-T/SGD	79.6	83.3	76.0	80.0	0.887
IRNV2	77.6	88.9	66.7	79.5	0.841
IRNV2 + F-T	78.9	**94.4**	64.0	81.4	0.874
NNL	73.5	83.3	64.0	75.5	0.845
NNL + F-T	74.8	84.7	65.3	76.7	0.840
Hard Voting	83.0	91.7	74.7	84.1	--
Soft Voting	**84.4**	**94.4**	74.7	**85.5**	**0.920**

Other investigations that seek to identify the presence of lesions on CT images using transfer learning have reported an accuracy of 99%. Such is the case of Ahuja et al. [32], who used different versions of the ResNet and the SqueezeNet networks; They worked with a data set of 746 images of which 349 showed signs of COVID-19 lesions, obtained from 216 patients. However, unlike to our research, where all images from the CT studies were used and all patients had the disease, they did not use the full CT study for their experiments, just a few selected images of patients with the infection. In a similar task, Dey et al. [33] used an algorithm based on a segmentation and feature extraction scheme in CT images to detect COVID-19 lesions. Testing different classifiers, its algorithm reached a maximum accuracy of 87.75%.

It is important to mention that the studied networks presented a high classification error or misclassification in slices that were located at the beginning or at the end of the scans (at the cephalocaudal ends). It could be due to the fact that these images show a reduced area of lung tissue while the rest of the tissue can generate structures similar to abnormality findings suggesting a pulmonary lesion. An example of this issue can be seen in Figure 5. Here, two cases of slices located in the apex region of the upper lobes of the lungs are observed. The image in a) shows signs of consolidation in the left lung (enclosed with a segmented red oval), and the image in b) does not show signs of abnormality, however, in both cases the models classify the images with the presence of lesions.
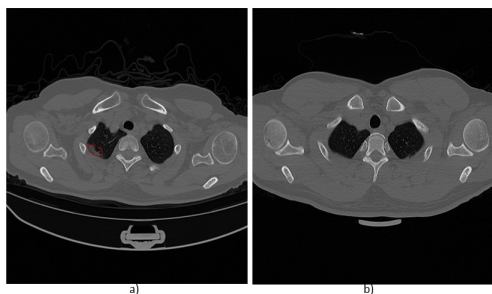

FIGURE 5. CT images from the apex region of the upper lobes of the lungs. a) CT slice that presents consolidation in the right lung (enclosed with a red segmented red oval), b) CT slice that does not show abnormal signs.

CONCLUSIONS

The objective of the present work was to detect the presence or absence of lung lesions in chest computed tomography images of patients with COVID-19 infection using deep learning models. In our study, the VGG16 model using the Coronacases Initiative repository presented the best results with an accuracy of 88%, AUC-ROC of 0.929 and F1-score of 87.8%. On the other hand, the soft voting ensemble, using the Radiopaedia repository, reached an accuracy of 84.4%, AUC-ROC of 0.92 and F1-score of 85.5%. The results of both models represent a good trade-off between the recall, specific-

ity and precision of the classifiers. It should be remarked that the management of the repositories, used independently of each other, improved the adjustment of the models, showing a greater generalization.

The model VGG16 with FT reached an accuracy of 80.3% using the Radiopaedia repository, however this performance was improved using combination models such as the soft voting and hard voting ensembles, with 84.4% and 83% of accuracy, respectively (both models with a high recall). It must be noted that this combination scheme was only satisfactory for this repository.

This research demonstrates that deep learning models can be useful to detect lung lesions of COVID-19 with high sensitivity and specificity for diagnosis; it can be valuable when considering the possible high false positive rate of clinical tests. In this way, an automatic detection model can serve as reference in radiology, allowing a quick localization of the lesion from a CT study with greater precision.

We must emphasize that in the present research, all the CT scans of the database included patients with a positive diagnosis of COVID-19, so the abnormality patterns found in the images are assumed to be indicative of lesions due to this disease. This represents a limitation in the present study since certainly other lung diseases such as interstitial pneumonia, sarcoidosis, alveolar proteinosis, carcinoma, etc., can produce similar patterns in CT scans to those found in patients with COVID-19 [10] [34]. Therefore, as future work, it is necessary to advance in this research to include patients with different lung diseases and classify the lesions according to their pathology of origin.

AUTHOR CONTRIBUTIONS

J.A.M. contributed to the writing of the original draft of the manuscript, performed data curation, organization, and annotation, and performed the experiments. J.D.D. conceptualized the project, designed, and devel-

oped the methodology, participated in the design of specialized software, carried out statistical analysis and writing of the manuscript. B.M.M. contributed to the design and development of the experiments and participated in the programming of the software for the implementation of deep learning models. J.M.M. contributed to the implementation of the computer algorithms, tested the codes for the reproducibility of the results and verified the organization of the data for the training, validation and testing of the imple-

mented models. L.R.M. participated in all the writing stages of the manuscript (preparation of the original draft, review, and edition of the final version), elaborated the images, carried out statistical analysis and contributed providing material and computer resources. J.C.R. supervised the development of the methodology, contributed to writing the draft and final version of the manuscript, designed the statistical tests and analysis. All authors reviewed and approved the final version of the manuscript.

REFERENCES

[1]   Rothan H, Byrareddy S. The epidemiology and pathogenesis of coronavirus disease (COVID-19) outbreak. J Autoimmun [Internet]. 2020;109:102433. Available from: **https://doi.org/10.1016/j.jaut.2020.102433**

[2]   Palacios Cruz M, Santos E, Velázquez Cervantes MA, León Juárez M. COVID-19, a worldwide public health emergency. Rev Clin Esp [Internet]. 2021;221(1):55-61. Available from: **https://doi.org/10.1016/j.rce.2020.03.001**

[3]   World Health Organization. Coronavirus Disease (COVID-19) Dashboard [Internet]. WHO Coronavirus Disease (COVID-19) Dashboard; 2021. Available from: *https://covid19.who.int/*

[4]   Instituto Mexicano del Seguro Social. Algoritmos interinos para la atención del COVID-19. Gobierno de México [Internet]. 2020; 1-31. Available from: *http://educacionensalud.imss.gob.mx/es/system/ files/Algoritmos_interinos_COVID19_CTEC.pdf*

[5]   He JL, Luo L, Luo ZD, Lyu JX, et al. Diagnostic performance between CT and initial real-time RT-PCR for clinically suspected 2019 coronavirus disease (COVID-19) patients outside Wuhan, China. Respir Med [Internet]. 2020;168:105980. Available from: **https://doi.org/10.1016/j.rmed.2020.105980**

[6]   Ai T, Yang Z, Hou H, Zhan C, et al. Correlation of Chest CT and RT-PCR Testing for Coronavirus Disease 2019 (COVID-19) in China: A Report of 1014 Cases. Radiology [Internet]. 2020;296(2):E32-40. Available from: **https://doi.org/10.1148/radiol.2020200642**

[7]   Rubin GD, Ryerson CJ, Haramati LB, Sverzellati N, et al. The Role of Chest Imaging in Patient Management During the COVID-19 Pandemic: A Multinational Consensus Statement From the Fleischner Society. Radiology [Internet]. 2020;296(1):172-180. Available from: **https://doi.org/10.1148/radiol.2020201365**

[8]   Shen M, Zhou Y, Ye J, AL-maskri AAA, et al. Recent advances and perspectives of nucleic acid detection for coronavirus. J Pharm Anal [Internet]. 2020;10(2):97-101. Available from: **https://doi.org/10.1016/j.jpha.2020.02.010**

[9]   Araujo Oliveira B, Campos de Oliveira L, Cerdeira Sabino E, Okay TS. SARS-CoV-2 and the COVID-19 disease: A mini review on diagnostic methods. Rev Inst Med Trop Sao Paulo [Internet]. 2020;62:e44. Available from: **https://doi.org/10.1590/S1678-9946202062044**

[10] Uysal E, Kilinçer A, Cebeci H, Özer H, et al. Chest CT findings in RT-PCR positive asymptomatic COVID-19 patients. Clin Imaging [Internet]. 2021;77:37-42. Available from: **https://doi.org/10.1016/j.clinimag.2021.01.030**

[11] Tahamtan A, Ardebili A. Real-time RT-PCR in COVID-19 detection: issues affecting the results. Expert Rev Mol Diagn [Internet]. 2020;20(5):453-4. Available from: **https://doi.org/10.1080/14737159.2020.1757437**

[12] Li X, Zeng W, Li X, Chen H, et al. CT imaging changes of corona virus disease 2019(COVID-19): A multi-center study in Southwest China. J Transl Med [Internet]. 2020;18:154. Available from: **https://doi.org/10.1186/s12967-020-02324-w**

[13] Yang X, He X, Zhao J, Zhang Y, et al. COVID-CT-Dataset: A CT Scan Dataset about COVID-19. arXiv:2003.13865 [Preprint]. 2020. Available from: *https://arxiv.org/abs/2003.13865*

[14] Bernheim A, Mei X, Huang M, Yang Y, et al. Chest CT findings in coronavirus disease 2019 (COVID-19): Relationship to duration of infection. Radiology [Internet]. 2020;295(3):685-91. Available from: **https://doi.org/10.1148/radiol.2020200463**

[15] Naudé W. Artificial intelligence vs COVID-19: limitations, constraints and pitfalls. AI Soc [Internet]. 2020;35(3):761-765. Available from: **https://doi.org/10.1007/s00146-020-00978-0**

[16] Bullock J, Luccioni A, Pham KH, Lam C, et al. Mapping the Landscape of Artificial Intelligence Applications against COVID-19. arXiv:2003.11336 [Preprint]. 2020;1-32. Available from: *http://arxiv.org/abs/2003.11336*

[17] Li L, Qin L, Xu Z, Yin Y, et al. Using Artificial Intelligence to Detect COVID-19 and Community-acquired Pneumonia Based on Pulmonary CT: Evaluation of the Diagnostic Accuracy. Radiology [Internet]. 2020;296(2):E65-71. Available from: **https://doi.org/10.1148/radiol.2020200905**

[18] Shah V, Keniya R, Shridharani A, Punjabi M, et al. Diagnosis of COVID-19 using CT scan images and deep learning techniques. Emerg Radiol [Internet]. 2021;28: 497-505. Available from: **https://doi.org/10.1007/s10140-020-01886-y**

[19] Ma J, Wang Y, An X, Ge C, et al. Toward data-efficient learning: A benchmark for COVID-19 CT lung and infection segmentation. Med Phys [Internet]. 2021;48(3):1197-1210. Available from: **https://doi.org/10.1002/mp.14676**

[20] Jun M, Cheng G, Yixin W, Xingle A, et al. COVID-19 CT Lung and Infection Segmentation Dataset [Data set]. Zenodo. 2020. Available from: **https://doi.org/10.5281/zenodo.3757476**

[21] Karimpanal TG, Bouffanais R. Self-organizing maps for storage and transfer of knowledge in reinforcement learning. Adapt Behav [Internet]. 2019;27(2):111-126. Available from: **https://doi.org/10.1177%2F1059712318818568**

[22] Nefoussi S, Amamra A, Amarouche IA. A Comparative Study of Deep Learning Networks for COVID-19 Recognition in Chest X-ray Images. In 2020 2nd International Workshop on Human-Centric Smart Environments for Health and Well-being (IHSH) [Internet]. Boumerdes: IEEE; 2021;237-41. Available from: **https://doi.org/10.1109/IHSH51661.2021.9378703**

[23] Shazia A, Xuan ZT, Chuah JH, Usman J, et al. A comparative study of multiple neural network for detection of COVID-19 on chest X-ray. EURASIP J Adv Signal Process [Internet]. 2021;2021(1):50. Available from: **https://doi.org/10.1186/s13634-021-00755-1**

[24] Perumal, V, Narayanan V, Rajasekar SJS. Detection of COVID-19 using CXR and CT images using Transfer Learning and Haralick features. Appl Intell [Internet]. 2021;51:341-358. Available from: **https://doi.org/10.1007/s10489-020-01831-z**

[25] Rahaman MM, Li C, Yao Y, Kulwa F, et al. Identification of COVID-19 samples from chest X-Ray images using deep learning: A comparison of transfer learning approaches. J Xray Sci Technol [Internet]. 2020;28(5):821-39. Available from: **https://doi.org/10.3233/xst-200715**

[26] He K, Zhang X, Ren S, Sun J. Deep Residual Learning for Image Recognition. In 2016 IEEE Conference on Computer Vision and Pattern Recognition (CVPR) [Internet]. Las Vegas: IEEE; 2016:770-778. Available from: **https://doi.org/10.1109/CVPR.2016.90**

[27] Simonyan K, Zisserman A. Very Deep Convolutional Networks For Large-Scale Image Recognition.   arXiv:1409.1556 [Internet]. 2015. Available from: *https://arxiv.org/abs/1409.1556*

[28] Szegedy C, Ioffe S, Vanhoucke V, Alemi AA. Inception-v4, inception-ResNet and the impact of residual connections on learning. In Proceedings of the Thirty-First AAAI Conference on Artificial Intelligence [Internet]. San Francisco:AAAI Pres; 2017:4278-4284. Available from: **https://dl.acm.org/doi/10.5555/3298023.3298188**

[29] Zoph B, Brain G, Vasudevan V, Shlens J, Le Google Brain Q V. Learning Transferable Architectures for Scalable Image Recognition. In 2018 IEEE/CVF Conference on Computer Vision and Pattern Recognition [Internet]. Salt Lake City :IEEE; 2018:8697-8710. Available from: **https://doi.org/10.1109/CVPR.2018.00907**

[30] Sahlol AT, Kollmannsberger P, Ewees AA. Efficient Classification of White Blood Cell Leukemia with Improved Swarm Optimization of Deep Features. Sci Rep [Internet]. 2020;10(1):2536. Available from: **https://doi.org/10.1038/s41598-020-59215-9**

[31] Russakovsky O, Deng J, Su H, Krause J, et al. ImageNet Large Scale Visual Recognition Challenge. Int J Comput Vis [Internet]. 2015;115:211-52. Available from: **https://doi.org/10.1007/s11263-015-0816-y**

[32] Ahuja S, Panigrahi BK, Dey N, Rajinikanth V, et al. Deep transfer learning-based automated detection of COVID-19 from lung CT scan slices. Appl Intell [Internet]. 2021;51:571-585. Available from: **https://doi.org/10.1007/s10489-020-01826-w**

[33] Dey N, Rajinikanth V, Fong SJ, Kaiser MS, et al. Social Group Optimization-Assisted Kapur's Entropy and Morphological Segmentation for Automated Detection of COVID-19 Infection from Computed Tomography Images. Cogn Comput [Internet]. 2020;12:1011-1023. Available from: **https://doi.org/10.1007/s12559-020-09751-3**

[34] Franquet, T. Diagnóstico por imagen de las enfermedades Pulmonares difusas: Signos y patrones diagnósticos básicos. Med respir. 2012;5(3):49-67

Healing of Wounds Treated with Chitosan Hydrogels with Extracts from *Aloe vera* and *Calendula officinalis*

Cicatrización de Heridas Tratadas con Hidrogeles de Quitosano con Extractos de *Aloe vera* y *Calendula officinalis*

Arturo Kenzuke Nakamura-García[1] (iD), Elba del Carmen Santos-Garfias[1] (iD), Daniela Israeely Alonso-Martínez[1] (iD), Teresa Itandehui Garambullo-Peña[1] (iD), José Fernando Covián-Nares[1] (iD), Mariana Gómez-Barroso[2] (iD), Rocío Montoya-Pérez[2] (iD)

[1]Departamento de Ingeniería Química y Bioquímica, Tecnológico Nacional de México, campus Morelia
[2]Instituto de Investigaciones Químico Biológicas, Universidad Michoacana de San Nicolás de Hidalgo

ABSTRACT

This project's purpose was to evaluate the healing effects of chitosan (CS) hydrogels loaded with extracts from *Aloe vera* (CS+AV) and *Calendula officinalis* (CS+CO) on wounds of diabetic and non-diabetic Wistar rats. A total of 24 rats were used; animals were randomly divided into three diabetic and three non-diabetic groups (one control and two treated groups) and monitored for 13 days. A biopsy on the wound site was recovered to assess the collagen and n-acetyl glucosamine content. The wound area ratio was reduced since day 1 on both non-diabetic treated groups. A similar effect was observed on the diabetic group treated with CS+AV, while the diabetic group treated with CS+CO showed a reduction in wound area compared to the diabetic control until day 11 after being wounded. Collagen and n-acetyl glucosamine content were higher in every treated group. Further studies are needed to clarify the underlying mechanisms through which they promote wound healing. These results suggest that the hydrogels prepared are potential material to be used as wound dressings.

RESUMEN

El propósito de este proyecto fue evaluar los efectos curativos de los hidrogeles de quitosano con extractos de *Aloe vera* (CS + AV) y *Calendula officinalis* (CS + CO) en heridas en ratas Wistar diabéticas y no diabéticas. Se utilizaron un total de 24 ratas; los animales fueron divididos aleatoriamente en tres grupos diabéticos y tres no diabéticos (un grupo control y dos tratados) y se monitorearon durante 13 días. Se recuperó una biopsia del sitio de la herida para evaluar el contenido de colágeno y n-acetilglucosamina. El área de la herida se redujo desde el día 1 en ambos grupos no diabéticos tratados. Se observó un efecto similar en el grupo diabético tratado con CS + AV, mientras que el grupo diabético tratado con CS + CO mostró una reducción del área de la herida en comparación al control diabético hasta el día 11 después de la creación de la herida. El contenido de colágeno y n-acetilglucosamina fue mayor en todos los grupos tratados. Se necesitan más estudios para aclarar los mecanismos subyacentes a través de los cuales estos tratamientos promueven la cicatrización de heridas. Estos resultados sugieren que los hidrogeles preparados son materiales con potencial para usarse como apósitos para heridas.

PALABRAS CLAVE: *Aloe vera*, *Calendula officinalis*, Quitosano, Herida diabética, Modelo animal

Corresponding author

TO: **Rocío Montoya-Pérez**

INSTITUTION: **Universidad Michoacana de San Nicolás de Hidalgo, Instituto de Investigaciones Químico-Biológicas**

ADDRESS: **Francisco J. Múgica S/N, Col. Felicitas del Río, C. P. 58030, Morelia, Michoacán, México**

CORREO ELECTRÓNICO: **rocio.montoya@umich.mx**

INTRODUCTION

Diabetes mellitus is a chronic disorder defined by impaired insulin secretion or insulin resistance of target tissues, resulting in high blood glucose levels. Diabetic Foot Ulcer (DFU) is a complication of this disorder; it is defined as a full-thickness chronic wound located at a level distal to the diabetic patient [1]. DFU is responsible for amputating a lower limb in the world every 30 s [2], and any diabetic patient has a 25% chance of developing this wound [3].

The wound healing process comprises four overlapping phases:

Hemostasis: This stage aims to prevent further bleeding immediately upon injury, but in the long-term, this process provides a matrix for cells needed in later phases [4] [5] [6].

Inflammation: This stage establishes an immune barrier against pathogens [4] [6] [7]. The wound healing process is impaired in chronic wounds, typically presenting a self-perpetuating inflammation state [7] with abundant neutrophil infiltration, which increases proteases and reactive oxygen species (ROS) levels that further damage the tissue [8], thus a frequent goal on wound management is to reduce inflammation [9].

Proliferation: This phase forms a granulation tissue [6]. Consisting primarily of macrophages, fibroblasts and blood vessels, its function is to provide a barrier to infection and a matrix for cellular migration [10]. Re-epithelialization and angiogenesis also occur in this phase [11] [12] [13].

Remodeling: The remodeling process gradually transforms the granulation tissue into scar tissue [14]. The wound's tensile strength increases as the unarranged type III collagen deposited on the granulation tissue is degraded and replaced with type I collagen, organized in parallel bundles along tension lines and

becomes highly cross-linked [10] [15] [16]. Other structural components of the extracellular matrix (ECM) that were primarily produced in earlier phases of wound healing diminishes as well, such as fibronectin, proteoglycans and glycosaminoglycans [5] [15].

Wound management involves using different materials such as films, sponges, fibers, nanoparticles and hydrogels [17]. Wound dressings should protect the wound from contamination and moisture loss and provide a structure that allows oxygen permeability and mimics ECM properties [17] [18]. Hydrogels are three-dimensional structures composed primarily of water and a cross-linked polymer network. Their high water content provides physical properties that resemble the ECM, giving them excellent biocompatibility [19] [20] [21].

Chitosan is a heteropolysaccharide made up of glucosamine and n-acetyl glucosamine derived from chitin [22]. It has many properties such as biocompatibility, biodegradability, antimicrobial and hemostatic capability, and bio-adhesiveness [23] [24]. Furthermore, it enhances wound healing by averting the accumulation of exudate, promoting gas exchange and drainage of the wound, and improving re-epithelization and the functions of polymorphonuclear leukocytes (PMN), macrophages and fibroblasts [17] [23] [25].

Plant extracts contain growth factors and compounds with antioxidant, antimicrobial and anti-inflammatory potential, representing a viable alternative to lessen the financial burden of long-term use of antibiotics and to be used in a topical wound treatment [26]. *Aloe vera* plant enhances fibroblasts and leukocyte's activity, and its wound healing mechanism has been positively correlated with glucomannan and acemannan [27] [28] [29]. Extracts of *C. officinalis* have shown positive effects on wound healing, enhancing the proliferation of fibroblasts and keratinocytes, increasing angiogenesis, reducing collagenase activity, and having antibacterial, anti-inflammatory and antioxidant activity [30] [31] [32].

Glucosaminoglycans (GAGs) are mainly formed by repeated units of an amino sugar attached to a uronic acid. In the early stages of healing, they are secreted to create the fundamental substance on which collagen and elastin deposition takes place to form the extracellular matrix [33] [34]. N-acetyl glucosamine (NAGA) is a monosaccharide and a basic component of hyaluronic acid and keratin sulfate on the cell surface, promotes the proliferation of keratinocytes and fibroblasts and increases the production of hyaluronic acid in the skin; it has also been successfully used to heal wounds. In the wound healing process, in the late stages of fibroplasia, the maturation of collagen fibers reduces the cellularity of the wound and increases tensile strength [10] [35]. Collagens are the most abundant protein family in the extracellular matrix. The main types of collagen present in the skin are type I (80%) and type III (15%). During the early stages of the formation of granulation tissue, the expression of Collagen III increases, from 20% to 50%. Later, during the maturation of the wound, Collagen III content decreases to normal levels, increasing the content of Collagen I, which contributes to the recovery of the tensile strength of the tissue [6] [16] [36]. In the present research article, we investigated the effect of chitosan hydrogels loaded with plant extracts on the wound healing process of full-thickness cutaneous wounds of diabetic and non-diabetic animals by analyzing wound contraction rates and the biochemical assessment (NAGA and collagen content) of wounded tissues.

MATERIALS AND METHODS

Materials

Chitosan with a 75-85% deacetylation and low molecular weight degree was purchased from Sigma-Aldrich. *Aloe vera* plants were purchased from a local greenhouse in Morelia and dried *Calendula officinalis* flowers were purchased from a local market in Morelia. All other reagents used were of analytical grade. Deionized water was used throughout this study.

Hydrogels and plant extract preparation

Chitosan solution was obtained by dissolving chitosan in an aqueous solution of 1% v/v of acetic acid, which was further mixed with a 1% m/v solution of CaCl2 in a 3:1 proportion, obtaining the chitosan hydrogel (CS) (Figure 1a). This chitosan hydrogel was mixed in a 9:1 proportion with the plant extracts, obtaining the CS+AV and CS+CO treatments. The final concentration of chitosan in the hydrogels was 35.99 mg/ml [37].

Healthy leaves of *Aloe vera* (AV) (2 years old) were processed as previously reported [38]. Briefly, *Aloe vera* leaves were washed with soap and tap water, and a longitudinal incision was performed on them to extract the *Aloe vera* gel, which was ground and heated on a water bath at 50 °C for 7 min (Figure 1b). After the water bath, the gel was filtered using sterile gauze and immediately mixed with the CS gel (obtaining the CS+AV treatment) (Figure 1d).

A macerate of dried *Calendula officinalis* (CO) flowers was prepared using a 95% ethanol aqueous solution, mixing 1 g of dried flowers per 10 ml of solvent for 48 h, after which the mixing was filtered using sterile gauze. The resulting macerate was dried at room temperature for 5 h to remove the ethanol, obtaining an oil (Figure 1c) that was mixed with the CS gel (obtaining the CS+CO treatment) (Figure 1d).

In vivo wound healing study Experimental design

In this study, a total of 24 Wistar male rats weighing between 260 and 320 g were used. The animals were kept in individual cages in a room with a constant temperature of 25 ± 1 °C with a 12 h light/dark cycle. All rats had free access to water and standard laboratory chow. All animal procedures were conducted following the Mexican Federal Regulations for Animal Experimentation and Care (NOM-062- ZOO-1999).
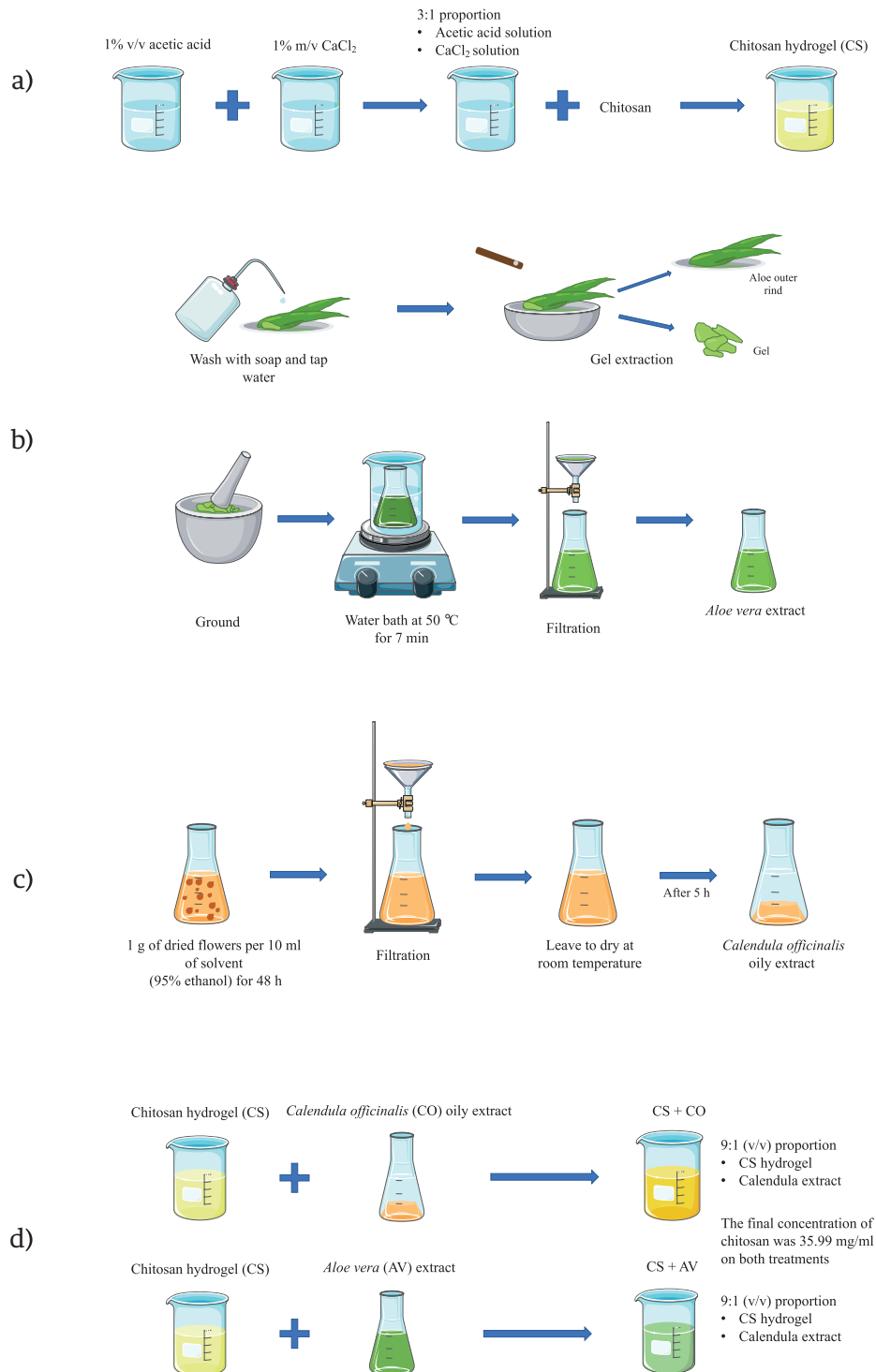
FIGURE 1. A scheme cartoon of the process to obtain the treatments employed in this research.
(a) Process to obtain the chitosan hydrogel (CS). (b) Process to obtain the *Aloe vera* extract (AV).
(c) Process to obtain the *C. officinalis* extract (CO). (d) Process to obtain the CS+AV and CS+CO hydrogels.
The majority of the schematic art pieces in this figure were provided by Servier Medical Art (smart.servier.com).
Servier Medical Art by Servier is licensed under a Creative Commons Attribution 3.0 Unported License.

Diabetic model protocol

As reported in previous studies [3] [39] [40] [41], diabetes was induced after fasting for 12 h, by intraperitoneal (i.p.) injection of 45 mg/kg body weight (BW) streptozotocin dissolved in 0.1 M citrate buffer (pH 4.5). To confirm that the diabetic model was successfully established, blood was drawn by a small incision on the rat tail using a blood lancet and it was absorbed using blood glucose test strips to determine the blood glucose levels using a glucometer (AccuCheck). When the glucose level was higher than 200 mg/ml, the diabetic model was established.

Incisional wound model

Animals were anesthetized with an i.p. injection of 50 mg/kg BW pentobarbital, after which the hairs on the back of the animals were shaved using an electric clipper. A fold was created on the skin dorsum, which was then cut using a 6-mm sterilized biopsy punch, creating a full-thickness round wound on each side of the dorsum.

Animals were divided into six experimental groups (n=4), three of them with streptozotocin-induced diabetic animals:

- I: diabetic control group (no treatment)
- II: diabetic group topically treated with CS+AV
- III: diabetic group topically treated with CS+CO
- IV: non-diabetic control group (no treatment)
- V: non-diabetic group topically treated with CS+AV
- VI: non-diabetic group topically treated with CS+CO

Wounds were treated topically with 100 µl of the correspondent hydrogel. Each animal was monitored for 13 days from the day of injury induction (Day 0), after which the animals were euthanized by injection of a lethal dose of pentobarbital (100 mg/kg BW). Full-thickness biopsies were retrieved from the wound site for further biochemical analysis.

Wound healing analysis

Wound kinetics and data analysis

Wound kinetics were recorded using a 13 MP digital camera and were quantified using AutoCAD to measure wound area daily. The wound area was expressed as a percentage of the initial wound area (100%).

Biochemical assessment of wounds

Samples were dried at 48 °C for 24 h, after which they were hydrolyzed in 5 ml of concentrated HCl/acetic acid solution (4:1 vol/vol) at 70 - 80 °C for 3 h. After being cooled with tap water, hydrolyzates were diluted in distilled water with a final concentration of 50% v/v for use in estimating hydroxyproline (Hyp) and n-acetyl glucosamine (NAGA). Collagen content in the skin was calculated from the Hyp content by multiplying it by a factor of 7.46 [42]. The assessment was carried out using a reaction with Erhlich's reagent; briefly, a pyrrole ring was formed on both compounds (by oxidative dehydrogenation in Hyp [43] and NAGA by alkaline treatment [44]) that reacts with Ehrlich's reagent to form a quinoid chromophore that can be quantified by UV-Vis spectroscopy.

Hydroxyproline and Collagen estimation. The hydrolyzates were subjected to oxidation by the addition of 1 ml of a Chloramine-T solution (1 part of Chloramine-T solution at 7% w/v and 4 parts of buffer (pH 6) of 0.42 M sodium acetate, 0.127 M sodium citrate and 0.026 M citric acid) and 1 ml of isopropanol. After 4 minutes, 2 ml of Ehrlich reagent (prepared as previously described by Cheng [45]) were added. The mixtures were heated in a water bath at 60 °C for 25 min. After cooling with tap water, absorbances were read at 557 nm. A standard solution of Hydroxyproline (Hyp) was obtained by diluting 25 mg of Hyp (purchased from Sigma Aldrich) in 250 ml of water (100 µg/ml) and was used to prepare a calibration curve. Aliquots of 5, 25, 50, 75 and 100 µl were taken and diluted in distilled water to a final volume of 5 ml, obtaining solutions with 0.1, 0.5, 1, 1.5

and 2 μg/ml. These solutions were treated with the same procedure as the hydrolyzates to get a Hyp calibration curve at 557 nm. Hyp content was estimated by linear interpolation. As stated before, Collagen content was calculated by multiplying the Hyp content by a factor of 7.46.

N-acetyl glucosamine (NAGA) estimation. Briefly, 0.5 ml of the hydrolyzates solutions were added 0.5 ml of potassium tetraborate 0.1 M and heated on boiling water for 3 min; afterward, 3 ml of Ehrlich reagent (prepared as described by Reissig, Strominger & Leloir [46]) were added. The mixtures were heated on a water bath at 36-38 °C for 20 min. After cooling with tap water, absorbances were read at 545 nm. The values of NAGA were estimated using the molar extinction coefficient of 21,000 [46].

Statistical analysis

Statistical analysis of wound kinetics and biochemical assessment was performed with one-way ANOVA with a post-hoc Tuckey analysis. A value of $P \leq 0.05$ was considered statistically significant.

RESULTS AND DISCUSSION

Results

Wound kinetics. Figures 2 and 3 show the wound kinetics and wound area ratios for both diabetic and non-diabetic groups, respectively. Both diabetic and non-diabetic groups treated with CS+AV showed a reduced wound area compared to the respective control groups from day 1 after wounding, while CS+CO treatment reduced wound area from day 1 only on the non-diabetic group in comparison to the group IV. Groups V and VI showed remarkable differences in wound area ratios compared to group IV, reducing the wound area up to 40 ~ 60 % on day 1 and resulting in a smaller wound area ratio than the control group by the end of the study. On the other hand, group II showed a decrease in wound area ratio of ~29% on day 1 and
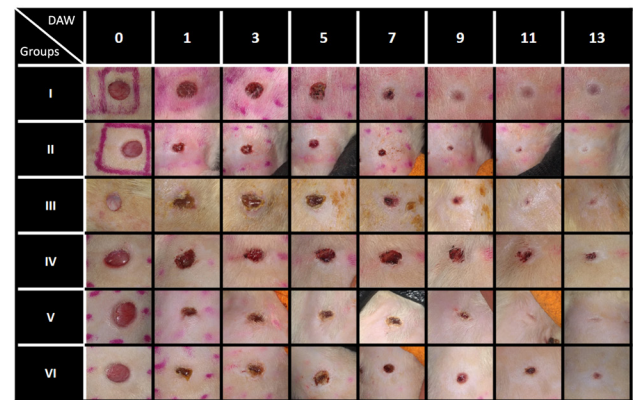
FIGURE 2. Wound kinetics of full-thickness wounds on various days during the healing process. DAW = Day After Wounded.
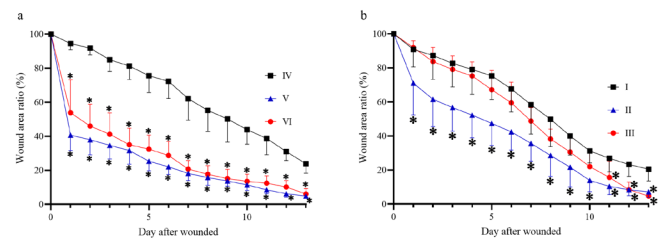
FIGURE 3. Wound area ratio during the wound healing process. (a) Wound area ratio on non-diabetic groups. (b) Wound area ratio on diabetic groups. *$P \leq 0.05$ compared to the corresponding control group.

group III behaved very similarly compared to diabetic control. Nevertheless, groups III and II showed a 13 ~ 15% decrease in wound area compared to group I on the last day of the study.

Hydroxyproline and Collagen estimation. Figure 4 (a and b) shows the results of the assessment of the collagen content. The groups treated, both diabetic and non-diabetic, show a higher collagen content compared to their respective control groups. Interestingly, diabetic groups show a higher content of collagen compared to the non-diabetic groups.

N-acetyl glucosamine (NAGA) estimation. NAGA content increased in the groups treated with both gels compared to the control groups; however, only the

diabetic group treated with CS+AV (group II) presented a statistically significant difference compared to the control group. Similarly, as in the collagen content, the diabetic groups showed a slightly higher NAGA content than the non – diabetic groups (Figure 4c and 4d).
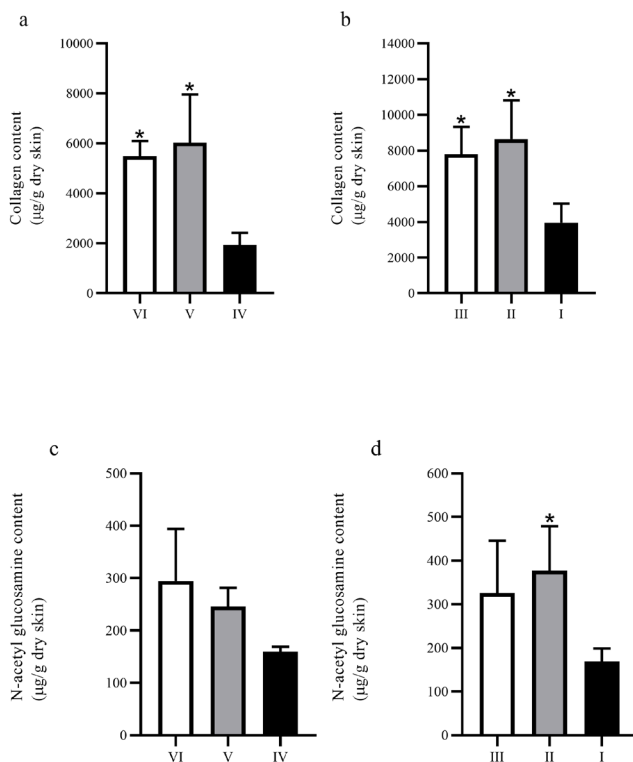
FIGURE 4. Collagen and NAGA content on biopsies from full-thickness wounds. (a) and (b) show the collagen content on biopsies from non-diabetic and diabetic groups, respectively; (c) and (d) show the NAGA content on biopsies from non-diabetic and diabetic groups, respectively. *P ≤ 0.05 compared to the corresponding control group.

Discussion

This study investigated the wound healing process of wounds treated with two chitosan hydrogels loaded with different plant extracts of *Aloe vera* and *Calendula officinalis*. Our results showed that treatment with both hydrogels accelerates wound contraction and enhances ECM's components' deposition, and are by previous studies involving chitosan, *C. officinalis* and A. vera [31] [33] [42] [47] [48]. Speed of contraction is signifi-

cant in decreasing the wound's area in full-thickness injuries [49]. The quantitative analysis data of the wound area ratio suggests that the best treatment at achieving this was CS+AV since it showed better performance at reducing the wound area ratio in both diabetic and non-diabetic groups. Although the diabetic and non-diabetic control groups did not have a significant difference between them, the comparison between the groups treated with CS+CO suggests that the diabetic model has a slower wound contraction and less sensitivity to this treatment in contrast to the non-diabetic model. Myofibroblasts are differentiated fibroblasts that exhibit an actin microfilaments rich cytoskeleton and are the primarily responsible cells for wound contraction [4] [5] [7] [12]. Wound area ratio results suggest treatments might have enhanced myofibroblasts differentiation and activity in the early stages of wound healing (except on the group III, in which a significant wound contraction was only seen until day 11 after wounded). Further studies comparing the effect of chitosan and plant extracts are necessary to clarify the mechanisms and components accountable for this effect.

Accelerated wound healing can also be detected by analyzing ECM's deposition dynamics, particularly glycosaminoglycans (GAGs) and collagen [15] [50]. GAGs are mainly composed of repeating units of an amino sugar (e.g., n-acetyl glucosamine or n-acetyl galactosamine) attached to a uronic acid. During early wound healing, the ground substance is composed mainly of GAGs that regulate early inflammation, fibroblast migration and form scaffolds for collagen polymerization and maturation [16] [42] [51]. Subsequently, the content of GAGs in the tissue is reduced, and collagen production increases [33] [34]. In late fibroplasia stages, collagen fiber maturation reduces wound cellularity and increases tensile strength [10] [35] [52]. The low levels of NAGA observed in all groups in proportion to collagen content suggest that the wounds were in a middle or late stage of fibroplasia, in which collagen is

mainly produced in the ECM [42] [49] [53]. It should be noted that the high collagen content observed in the treated groups may have been produced by an increase in the content of GAGs in the early stages of healing since collagen synthesis is influenced by the mucopolysaccharides of the ground substance of the ECM.

In the skin, the main types of collagen present are type I (80%) and type III (15%); the ratio of these two proteins changes during the early phases of wound healing. During the formation of granulation tissue, the expression of Collagen III increases to Collagen I expression, from 20% to 50%. Later, during wound maturation, the proportion decreases again to normal levels, increasing Collagen I's content, which contributes to the recovery of the tissue's tensile strength [6] [16] [36]. The high collagen levels observed in the treated groups suggest that the formulations improve the healing process since the increase in the collagen content in this process has been correlated with the maturation of the tissue, with the decrease in total cellularity (which is a sign of decreased inflammation) and with the development of blood vessels [42] [53]. Although collagen's overproduction could produce a keloid or hypertrophic scar [54], this pathology was not observed in either animal group of this study.

These results could be attributed to the different types of bioactive compounds present in the plant extracts that were employed. The anti-inflamatory and fibroblast stimulating activity of calendula has been attributed to its high terpenoids content, some of the identified terpenoids on calendula's extracts are: sitosterols, ursadiol, calenduladiol esters, calendulosides, calenduladiol, faradiol, among others [30] [55] [56]. In addition to this, these extracts are also especially rich in flavonoids, like quercetin, isorhamnetin, isoquercitin, narcissin, calendoflaside, calendoflavoside and calendoflavobioside, among others. The flavonoid content confers the extracts of its antimicrobial and antioxidant properties [31] [55] [57]. Meanwhile, the *Aloe vera* possess 75 potential bioactive phytochemicals. Its immuno-stimulatory activity has been attributed to the polysaccharides present in the pulp [58], like gluco-mannan and acemannan; the former is considered as a very strong immunomodulator of plant origin, while the latter is responsible for augmenting the collagen production by enhancing fibroblast proliferation. Other type of bioactive phytochemical present in *Aloe vera* are anthraquinones, which have anti-inflamatory and antioxidant activity [58] [59]. Although the extracts have many bioactive compounds with different properties, it is possible that the beneficial effects of the extracts are a result of the interaction between these various compounds. Further experiments with the separate components of the treatments of this study (Chitosan, *Aloe vera* and *Calendula officinalis*) are needed to identify which component is responsible for the different effects observed. Also, the characterization of these components could help to elucidate if one chemical compound could be specifically responsible for the major benefits observed or if these are the result of a synergic effect from the various bioactive phytochemicals and the chitosan.

CONCLUSIONS

In conclusion, data collected in this study shows that chitosan hydrogels loaded with plant extracts of *Aloe vera* and *Calendula officinalis* have a beneficial effect on the wound healing process of full-thickness wounds in both diabetic and non-diabetic models. The CS+AV treatment showed a remarkable performance on the diabetic model in comparison to the CS+CO treatment. Nevertheless, the biochemical results suggest that both treatments were able to reduce inflammation and accelerate fibroplasia. Hence, this study shows that the developed hydrogels are potential materials to treat skin wounds, particularly DFU, given the observations on the treated diabetic model. Further studies are required to understand the specific effects that the treatments have on each wound-healing phase and which component of the therapy is responsible for each outcome.

ETHICAL STATEMENT

All animal procedures were conducted following the Mexican Federal Regulations for Animal Experimentation and Care (NOM-062-ZOO-1999, México) and were approved by the Institutional Committee of the Instituto de Investigaciones Químico-Biológicas of the Universidad Michoacana de San Nicolás de Hidalgo for the Use and Care of Animals (7-09-2021, Ref. No. 08/2020).

AUTHOR CONTRIBUTIONS

A.K.N.G. conceptualized the research, defined the scope and goals of the project; designed and defined methodology and performed analyses; developed the methods of the analyses for the biochemical assessment of the wounds, performed the wound image analysis in AUTOCAD, and carried out the statistical analyses in GraphPad Prism; edited the original draft and addressed the commentaries of editorial review; created figures 1 to 4, and the graphical abstract of the paper. E.C.S.G. conceptualized the research; defined the scope and goals of the project; designed and defined methodology, especially for the diabetic and incisional wound models and to biochemical assessment of the wounds. Conducted and performed analyses; edited the original draft and addressed the commentaries of editorial review; created figures 1 and 4, and the graphical abstract of the paper. D.I.A.M. contributed to the design and development of methodology for the study; prepared materials and conducted analyses; contributed to create the Figure 2. T.I.G.P. Contributed to the original proposal of the project and helped to define the scope and goals; provided instruments and reagents; coordinated and supervised the preparation of material at several stages of the study; acquired funding from Tecnológico Nacional de Méxi-

co campus Morelia. J.F.C.N. Contributed to the original proposal of the project and helped to define the scope and goals; provided instruments and reagents; coordinated and supervised the preparation of material at several stages of the study; acquired funding from Tecnológico Nacional de México campus Morelia. M.G.B. contributed to the design and development of protocols and the design of methods for the modelling studies; participated in the development of in vivo studies; carried out the statistical analysis of wound healing kinetics on GraphPad Prism; oversaw the diabetes model protocol. R.M.P. contributed to the development of the initial proposal and helped to define the scope and goals; provided reagents for the diabetic and incisional wound protocols as well as instruments and lab animals for in vivo studies; coordinated and oversaw the in vivo wound healing study; acquired funding from the Universidad Michoacana de San Nicolás de Hidalgo. All authors participated equally in the writing and approval of the different stages of the manuscript.

The authors declare no conflict of interest.

REFERENCES

[1] Amin N, Doupis J. Diabeti Amin N, Doupis J. Diabetic foot disease: From the evaluation of the "foot at risk" to the novel diabetic ulcer treatment modalities. World J Diabetes [Internet]. 2016;7(7):153-164. Available from: **https://doi.org/10.4239/wjd.v7.i7.153**

[2] Amoah VMK, Anokye R, Acheampong E, Dadson HR, et al. The experiences of people with diabetes-related lower limb amputation at the Komfo Anokye Teaching Hospital (KATH) in Ghana. BMC Res Notes [Internet]. 2018;11:66. Available from: **https://doi.org/10.1186/s13104-018-3176-1**

[3] Dwita LP, Hasanah F, Srirustami R, Repi, et al. Wound healing properties of Epiphyllum oxypetalum (DC.) Haw. leaf extract in streptozotocin-induced diabetic mice by topical application. Wound Med [Internet]. 2019;26(1):100160. Available from: **https://doi.org/10.1016/j.wndm.2019.100160**

[4] Guillamat-Prats R. The Role of MSC in Wound Healing, Scarring and Regeneration. Cells [Internet]. 2021;10(7):1729. Available from: **http://dx.doi.org/10.3390/cells10071729**

[5] Cañedo-Dorantes L, Cañedo-Ayala M. Skin Acute Wound Healing: A Comprehensive review. Int J Inflam [Internet]. 2019;2019:3706315. Available from: **https://doi.org/10.1155/2019/3706315**

[6] Gushiken LFS, Beserra FP, Bastos JK, Jackson CJ, et al. Cutaneous Wound Healing: An Update from Physiopathology to Current Therapies. Life (Basel) [Internet]. 2021;11(7):665. Available from: **https://dx.doi.org/10.3390%2Flife11070665**

[7] Zhao R, Liang H, Clarke E, Jackson C, et al. Inflammation in Chronic Wounds. Int J Mol Sci [Internet]. 2016;17(12):2085. Available from: **https://doi.org/10.3390/ijms17122085**

[8] Ellis S, Lin EJ, Tartar D. Immunology of Wound Healing. Curr Dermatol Rep [Internet]. 2018;7(4):350-358. Available from: **https://doi.org/10.1007/s13671-018-0234-9**

[9] Barreto RSS, Albuquerque-Júnior RLC, Pereira-Filho RN, Quintans JSS, et al. Evaluation of wound healing activity of atranorin, a lichen secondary metabolite, on rodents. Rev Bras Farmacogn [Internet]. 2013;23(2):310-319. Available from: **http://dx.doi.org/10.1590/S0102-695X2013005000010**

[10] Theoret C. Physiology of Wound Healing. In: Theoret C, Schumacher J (eds.). Equine Wound Management [Internet]. Third ed. Ames, Iowa: John Wiley & Sons, Inc; 2016. 1-13p. Available from: **https://doi.org/10.1002/9781118999219.ch1**

[11] Pastar I, Stojadinovic O, Yin NC, Ramirez H, et al. Epithelialization in Wound Healing: A Comprehensive Review. Adv Wound Care [Internet]. 2014;3(7):445-64. Available from: **https://doi.org/10.1089/wound.2013.0473**

[12] Landén NX, Li D, Ståhle M. Transition from inflammation to proliferation: a critical step during wound healing. Cell Mol Life Sci [Internet]. 2016;73(20):3861-85. Available from: **https://doi.org/10.1007/s00018-016-2268-0**

[13] Gonzalez ACDO, Andrade ZDA, Costa TF, Medrado ARAP. Wound healing - A literature review. An Bras Dermatol [Internet]. 2016;91(5):614-620. Available from: **https://doi.org/10.1590/abd1806-4841.20164741**

[14] Minossi JG, Oliveira LA, Caramori CA, Hasimoto CN, et al. Alloxan diabetes alters the tensile strength, morphological and morphometric parameters of abdominal wall healing in rats. Acta Cir Bras [Internet]. 2014;29(2):118-124. Available from: **https://doi.org/10.1590/S0102-86502014000200008**

[15] Olczyk P, Mencner Ł, Komosinska-Vassev K. The Role of the Extracellular Matrix Components in Cutaneous Wound Healing. BioMed Res Int [Internet]. 2014:747584. Available from: **https://doi.org/10.1155/2014/747584**

[16] Xue M, Jackson CJ. Extracellular Matrix Reorganization During Wound Healing and Its Impact on Abnormal Scarring. Adv Wound Care [Internet]. 2015;4(3):119-136. Available from: **https://doi.org/10.1089/wound.2013.0485**

[17] Okur ME, Karantas ID, Şenyiğit Z, Üstündağ Okur N, et al. Recent trends on wound management: New therapeutic choices based on polymeric carriers. Asian J Pharm Sci [Internet]. 2020;15(6):661-684. Available from: **https://doi.org/10.1016/j.ajps.2019.11.008**

[18] Ehterami A, Salehi M, Farzamfar S, Vaez A, et al. In vitro and in vivo study of PCL/COLL wound dressing loaded with insulin-chitosan nanoparticles on cutaneous wound healing in rats model. Int J Biol Macromol [Internet]. 2018;117(1):601-609. Available from: **https://doi.org/10.1016/j.ijbiomac.2018.05.184**

[19] Daly AC, Riley L, Segura T, Burdick JA. Hydrogel microparticles for biomedical applications. Nat Rev Mater [Internet]. 2020;5(1):20-43. Available from: **http://dx.doi.org/10.1038/s41578-019-0148-6**

[20] Li J, Mooney DJ. Designing hydrogels for controlled drug delivery. Nat Rev Mater [Internet]. 2016;1(12):16071. Available from: **http://dx.doi.org/10.1038/natrevmats.2016.71**

[21] Chai Q, Jiao Y, Yu X. Hydrogels for Biomedical Applications: Their Characteristics and the Mechanisms behind Them. Gels [Internet]. 2017;3(1):6. Available from: **https://doi.org/10.3390/gels3010006**

[22] Azuma K, Izumi R, Osaki T, Ifuku S, et al. Chitin, Chitosan, and Its Derivatives for Wound Healing: Old and New Materials. J Funct Biomater [Internet]. 2015;6(1):104-142. Available from: **http://dx.doi.org/10.3390/jfb6010104**

[23] Dai T, Tanaka M, Huang Y-Y, Hamblin MR. Chitosan preparations for wound-healing effects. Expert Rev Anti Infect Ther [Internet]. 2011;9(7):857-879. Available from: **http://dx.doi.org/10.1586/eri.11.59**

[24] El-Kased RF, Amer RI, Attia D, Elmazar MM. Honey-based hydrogel: In vitro and comparative In vivo evaluation for burn wound healing. Sci Rep [Internet]. 2017;7(1):9692. Available from: **http://dx.doi.org/10.1038/s41598-017-08771-8**

[25] Matica MA, Aachmann FL, Tøndervik A, Sletta H, et al. Chitosan as a Wound Dressing Starting Material: Antimicrobial Properties and Mode of Action. Int J Mol Sci [Internet]. 2019;20(23):5889. Available from: **https://doi.org/10.3390/ijms20235889**

[26] Sivamani RK, Ma BR, Wehrli LN, Maverakis E. Phytochemicals and Naturally Derived Substances for Wound Healing. Adv Wound Care [Internet]. 2012;1(5):213-217. Available from: **https://doi.org/10.1089/wound.2011.0330**

[27]   Burusapat C, Supawan M, Pruksapong C, Pitiseree A, et al. Topical Aloe Vera Gel for Accelerated Wound Healing of Split-Thickness Skin Graft Donor Sites: A Double-Blind, Randomized, Controlled Trial and Systematic Review. Plast Reconstr Surg [Internet]. 2018;142(1):217-226. Available from: https://doi.org/10.1097/PRS.0000000000004515

[28]   Hashemi SA, Madani SA, Abediankenari S. The Review on Properties of Aloe Vera in Healing of Cutaneous Wounds. Biomed Res Int [Internet]. 2015;2015:714216. Available from: https://doi.org/10.1155/2015/714216

[29]   Darzi S, Paul K, Leitan S, Werkmeister JA, et al. Immunobiology and Application of Aloe vera-Based Scaffolds in Tissue Engineering. Int J Mol Sci [Internet]. 2021;22(4):1708. Available from: https://doi.org/10.3390/ijms22041708

[30]   Givol O, Kornhaber R, Visentin D, Cleary M, et al. A systematic review of Calendula officinalis extract for wound healing. Wound Repair Regen [Internet]. 2019;27(5):548-561. Available from: https://doi.org/10.1111/wrr.12737

[31]   Dinda M, Mazumdar S, Das S, Ganguly D, et al. The Water Fraction of Calendula officinalis Hydroethanol Extract Stimulates In Vitro and In Vivo Proliferation of Dermal Fibroblasts in Wound Healing. Phyther Res [Internet]. 2016;30(10):1696-1707. Available from: https://doi.org/10.1002/ptr.5678

[32]   Buzzi M, de Freitas F, de Barros Winter M. Therapeutic effectiveness of a Calendula officinalis extract in venous leg ulcer healing. J Wound Care [Internet]. 2016;25(12):732-739. Available from: https://doi.org/10.12968/jowc.2016.25.12.732

[33]   Chithra P, Sajithlal GB, Chandrakasan G. Influence of Aloe vera on the glycosaminoglycans in the matrix of healing dermal wounds in rats. J Ethnopharmacol [Internet]. 1998;59(3):179-186. Available from: https://doi.org/10.1016/S0378-8741(97)00112-8

[34]   Kosir MA, Quinn CCV, Wang W, Tromp G. Matrix Glycosaminoglycans in the Growth Phase of Fibroblasts: More of the Story in Wound Healing. J Surg Res [Internet]. 2000;92(1):45-52. Available from: https://doi.org/10.1006/jsre.2000.5840

[35]   Smith QT. Collagen Metabolism in Wound Healing. In: Day SB (eds). Trauma [Internet]. Boston: Springer; 1975. 31-45p. Available from: https://doi.org/10.1007/978-1-4684-2145-3_3

[36]   Bainbridge P. Wound healing and the role of fibroblasts. J Wound Care [Internet]. 2013;22(8):407-412. Available from: https://doi.org/10.12968/jowc.2013.22.8.407

[37]   Chhabra P, Mehra L, Mittal G, Kumar A. A Comparative Study on the Efficacy of Chitosan Gel Formulation and Conventional Silver Sulfadiazine Treatment in Healing Burn Wound Injury at Molecular Level. Asian J Pharm [Internet]. 2017;11(3):489-496. Available from: https://dx.doi.org/10.22377/ajp.v11i03.1449

[38]   Takzare N, Hosseini MJ, Hasanzadeh G, Mortazavi H, et al. Influence of Aloe Vera Gel on Dermal Wound Healing Process in Rat. Toxicol Mech Methods [Internet]. 2009;19(1):73-77. Available from: https://doi.org/10.1080/15376510802442444

[39]   Cheng KY, Lin ZH, Cheng YP, Chiu HY, et al. Wound Healing in Streptozotocin-Induced Diabetic Rats Using Atmospheric-Pressure Argon Plasma Jet. Sci Rep [Internet]. 2018;8(1):12214. Available from: https://doi.org/10.1038/s41598-018-30597-1

[40]   Bravo-Sánchez E, Peña-Montes D, Sánchez-Duarte S, Saavedra-Molina A, et al. Effects of Apocynin on Heart Muscle Oxidative Stress of Rats with Experimental Diabetes: Implications for Mitochondria. Antioxidants [Internet]. 2021;10(3):335. Available from: https://doi.org/10.3390/antiox10030335

[41]   Sánchez-Duarte S, Márquez-Gamiño S, Montoya-Pérez R, Villicaña-Gómez EA, et al. Nicorandil decreases oxidative stress in slow- and fast-twitch muscle fibers of diabetic rats by improving the glutathione system functioning. J Diabetes Investig [Internet]. 2021;12(7):1152-1161. Available from: https://doi.org/10.1111/jdi.13513

[42]   Oryan A, Mohammadalipour A, Moshiri A, Tabandeh MR. Topical Application of Aloe vera Accelerated Wound Healing, Modeling, and Remodeling. Ann Plast Surg [Internet]. 2016;77(1):37-46. Available from: https://doi.org/10.1097/SAP.0000000000000239

[43]   Ignat'eva NY, Danilov NA, Averkiev SV, Obrezkova MV, et al. Determination of hydroxyproline in tissues and the evaluation of the collagen content of the tissues. J Anal Chem [Internet]. 2007;62(1):51-7. Available from: https://doi.org/10.1134/S106193480701011X

[44]   Van Lenten, L. Automated Analysis of Amino Sugars using the Elson-Morgan Reaction [Internet]. [Dissertation]. [Connecticut]: Yale School of Medicine, 1966. 107p. Available from: https://elischolar.library.yale.edu/ymtdl/6/

[45]   Cheng PT. An Improved Method for the Determination of Hydroxyproline in Rat Skin. J Invest Dermatol [Internet]. 1969;53(2):112-115. Available from: http://dx.doi.org/10.1038/jid.1969.116

[46]   Reissig JL, Storminger JL, Leloir LF. A modified colorimetric method for the estimation of N-acetylamino sugars. J Biol Chem [Internet]. 1955;217(2):959-966. Available from: https://doi.org/10.1016/S0021-9258(18)65959-9

[47]   Movaffagh J, Bazzaz BSF, Yazdi AT, Sajadi-Tabassi A, et al. Wound Healing and Antimicrobial Effects of Chitosan-hydrogel/Honey Compounds in a Rat Full-thickness Wound Model. Wounds [Internet]. 2019;31(9):228-235. Available from: https://pubmed.ncbi.nlm.nih.gov/31298661/

[48]   Duran V, Matic M, Javanovć M, Mimica N, et al. Results of the clinical examination of an ointment with marigold (Calendula Officinalis) extract in the treatment of venous leg ulcers. Int J Tissue React [Internet]. 2005;27(3):101-106. Available from: https://europepmc.org/article/MED/16372475

[49]   Li J, Chen J, Kirsner R. Pathophysiology of acute wound healing. Clin Dermatol [Internet]. 2007;25(1):9-18. Available from: https://doi.org/10.1016/j.clindermatol.2006.09.007

[50]   Elegbede RD, Ilomuanya MO, Sowemimo AA, Nneji A, et al. Effect of fermented and green Aspalathus linearis extract loaded hydrogel on surgical wound healing in Sprague Dawley rats. Wound Med [Internet]. 2020;29:100186. Available from: https://doi.org/10.1016/j.wndm.2020.100186

[51]   Ghatak S, Maytin EV, MacK JA, Hascall VC, et al. Roles of Proteoglycans and Glycosaminoglycans in Wound Healing and Fibrosis. Int J Cell Biol [Internet]. 2015;2015:834893. Available from: https://doi.org/10.1155/2015/834893

[52]   Abatangelo G, Brun P, Cortivo R. Collagen Metabolism and Wound
       Contraction. In: Altmeyer P, Hoffman K, el Gammal S, Hutchinson J
       (eds). Wound Healing and Skin Physiology [Internet]. Berlin:
       Springer; 1995. 71-88p. Available from:
       https://doi.org/10.1007/978-3-642-77882-7_7

[53]   Monaco JAL, Lawrence WT. Acute wound healing: An overview.
       Clin Plast Surg [Internet]. 2003;30(1):1-12. Available from:
       https://doi.org/10.1016/S0094-1298(02)00070-6

[54]   Nunes PS, Albuquerque-Júnior RLC, Cavalcante DRR, Dantas MDM,
       et al. Collagen-Based Films Containing Liposome-Loaded Usnic
       Acid as Dressing for Dermal Burn Healing. Biomed Res Int
       [Internet]. 2011;2011:761593. Available from:
       https://doi.org/10.1155/2011/761593

[55]   Quave CL. Wound Healing with Botanicals: a Review and Future
       Perspectives. Curr Dermatol Rep [Internet]. 2018;7(4):287-295.
       Available from: **https://doi.org/10.1007/s13671-018-0247-4**

[56]   Muley BP, Khadabadi SS, Banarase NB. Phytochemical Constituents
       and Pharmacological Activities of Calendula officinalis Linn
       (Asteraceae): A Review. Trop J Pharm Res [Internet].
       2009;8(5):455-465. Available from:
       https://doi.org/10.4314/tjpr.v8i5.48090

[57]   Fonseca YM, Catini CD, Vicentini FTMC, Nomizo A, et al. Protective
       effect of Calendula officinalis extract against UVB-induced
       oxidative stress in skin: Evaluation of reduced glutathione levels
       and matrix metalloproteinase secretion. J Ethnopharmacol
       [Internet]. 2010;127(3):596-601. Available from:
       https://doi.org/10.1016/j.jep.2009.12.019

[58]   Majumder R, Das CK, Mandal M. Lead bioactive compounds of Aloe
       vera as potential anticancer agent. Pharmacol Res [Internet].
       2019;148:104416. Available from:
       https://doi.org/10.1016/j.phrs.2019.104416

[59]   Radha MH, Laxmipriya NP. Evaluation of biological properties and
       clinical effectiveness of Aloe vera: A systematic review. J Tradit
       Complement Med [Internet]. 2015;5(1):21-26. Available from:
       https://doi.org/10.1016/j.jtcme.2014.10.006

A Chitosan-based Hydrogel with PLCL, ZnO NPs, and Oligoelements: A Promising Antibiotic Scaffold for Tissue Engineering

Hidrogel de Quitosano con PLCL, ZnO NPs y Oligoelementos: Un Andamio Antibacteriano Prometedor para Ingeniería de Tejidos

Yvain de los Ángeles Salinas Delgado[1] (iD), Stephanie Soria Sánchez[1] (iD), Gabriela Guadalupe Esquivel Barajas[1] (iD),
Eduardo Leos Quiñonez[2] (iD), Luis Alberto Bretado Aragón[1] (iD)

[1]Universidad de La Ciénega del Estado de Michoacán de Ocampo

[2]Hospital Materno Infantil, Durango, Dgo.

ABSTRACT

Tissue engineering involves anchorage-dependent cells cultured on scaffolds, with growth factors added to facilitate cell proliferation. Its use in transplants implies the risk of bacterial infection. The current contribution describes the preparation and antibacterial evaluation of a chitosan-based hydrogel physically cross-linked with poly(l-lactic-co-ε-caprolactone) (PLCL) and enriched with zinc oxide nanoparticles (ZnO NPs) and trace elements (potassium and magnesium). The material was developed as a scaffold with built-in antibacterial properties. Chitosan and PLCL are biocompatible support materials applied in medicine for the repair and regeneration of damaged tissues, objectives promoted by ZnO NPs and the aforementioned trace elements. The ZnO NPs were elaborated by chemical coprecipitation. The materials were characterized by XRD, FT-IR, and SEM. Antibacterial testing was performed with strains of *Escherichia coli* and *Staphylococcus aureus* by the Kirby-Bauer method, in accordance with the NCCLS and CLSI guidelines. It was possible to obtain a homogeneous hydrogel with adequate morphology and distribution of elements. The hydrogel with 300 mM of Mg, K, and ZnO NP's showed antibacterial inhibition halos of 13 mm for *S. aureus* and 19 mm for *E. coli*. This innovative biomaterial with trace elements holds promise for tissue engineering by considering the challenge of bacterial infection.

KEYWORDS: Chitosan, PLCL, ZnO nanoparticles, Antibacterial, Tissue engineering

RESUMEN

La ingeniería de tejidos involucra el uso de células cultivadas en andamios con adiciones de factores de crecimiento para facilitar la proliferación celular. Su uso en trasplantes implica riesgo de infección bacteriana. La contribución actual describe la preparación y evaluación antibacteriana de un hidrogel a base de quitosano físicamente reticulado con poli (l-láctico-co-ε-caprolactona) (PLCL) enriquecido con nanopartículas de óxido de zinc (NP de ZnO) y oligoelementos (potasio y magnesio). El material se desarrolló como un andamio con propiedades antibacterianas. El quitosano y el PLCL son materiales de soporte biocompatibles aplicados en medicina para la reparación y regeneración de tejidos dañados, propiedades promovidas por las NP´s de ZnO y los oligoelementos antes mencionados. Las NP de ZnO se elaboraron mediante coprecipitación química. Los materiales se caracterizaron por DRX, FT-IR y SEM. Las pruebas antibacterianas se realizaron con cepas de *Escherichia coli* y *Staphylococcus aureus* por el método de Kirby-Bauer de acuerdo con las guías NCCLS y CLSI. Se pudo obtener un hidrogel homogéneo con adecuada morfología y distribución de elementos. El hidrogel con 300 mM de NP ZnO y oligoelementos mostró halos de inhibición antibacteriana de 13 mm para *S. aureus* y 19 mm para *E. coli*. Este biomaterial innovador con oligoelementos es prometedor para la ingeniería de tejidos al considerar el desafío de la infección bacteriana.

PALABRAS CLAVE: Quitosano, PLCL, Nanopartículas ZnO, Antibacterial, Ingeniería de Tejidos

Corresponding author

TO: **Luis Alberto Bretado Aragón**

INSTITUTION: **Universidad de La Ciénega del Estado de Michoacán de Ocampo**

ADDRESS: **Av. Universidad #3000, Col. Lomas de la Universidad, C. P. 59103, Sahuayo de Morelos, Michoacán, México**

CORREO ELECTRÓNICO: **labretado@ucemich.edu.mx**

INTRODUCTION

Tissue engineering aims to establish, restore, or increase the function of tissues by means of the in vitro culturing of anchorage-dependent cells (either differentiated or undifferentiated) on scaffolds made of biomaterials. Growth factors are added to facilitate cell proliferation.

The in vitro tissues are then transplanted to a target organ [1] [2] with tissue injury. Such an injury is susceptible to infection by pathogenic microorganisms, which can lead to the loss or alteration of transplanted tissue, thus complicating tissue recovery and sometimes causing implant failure [1].

The biomaterials utilized in tissue engineering are biocompatible polymers, such as chitosan, that elicit robust cell proliferation [3]. The latter biopolymer is biocompatible, biodegradable, non-toxic, non-mutagenic, bioactive, cationic, antibacterial, and antifungal. It has been of great interest in developing drug-delivery scaffolds for tissue engineering and has been classified as "generally recognized as safe" (GRAS) by the US Food and Drug Administration (FDA) [4] [5]. Another material approved by the FDA to foster cell proliferation and adhesion is the poly(l-lactide-co-ε-caprolactone) (PLCL) polymer, due to its biocompatibility and mechanical properties [6].

Chitosan can be combined with certain trace elements essential for biological, physiological, and enzymatic processes. Consequently, zinc (Zn), potassium (K), and magnesium (Mg) [7] are added to improve certain functions, including protection against bacteria or fungi, bone regeneration, the synthesis of proteins, the absorption of Fe^{3+}, the protection of tooth enamel, and the production of skin collagen [8] [9] [10]. ZnO nanoparticles (NPs), on the other hand, promote cell proliferation, growth, and differentiation. Additionally, their nanometric size affords high reactivity and thus favors an antibacterial effect [11].

During a surgical intervention for organ or tissue implantation, the main agents of infection are bacteria, which are able to generate septicemia, impetigo, cellulitis, skin abscesses, and even patient death [12]. The combination of chitosan, PLCL, ZnO NPs, and trace elements has an exciting future in tissue engineering. Apart from biocompatibility, this complex has the capacity for cell proliferation as well as inhibition of infection by nosocomial pathogens (e.g., *Staphylococcus aureus*, *Escherichia coli*, *Pseudomonas aeruginosa*, and *Serratia marcescens*) in surgical incisions and other medical conditions (e.g., diabetic foot and venous ulceration) [13].

The aim of the present study was to develop an HQT hydrogel with chitosan physically cross-linked to PLCL, with the addition of ZnO NPs and trace amounts of K and Mg. The ZnO NPs were obtained by chemical coprecipitation. The HQT hydrogel and its components were characterized with X-ray diffraction (XRD), Fourier transformed infrared spectroscopy (FT-IR), and scanning electron microscopy (SEM).

The antibacterial behavior of the HQT hydrogel was assessed with *S. aureus* ATCC® 25923 and *E. coli* ATCC® 25922 by means of the Kirby-Bauer method, in accordance with the international standards recommended by the Antimicrobial Susceptibility Testing Subcommittee of the National Committee for Clinical Laboratory Standards (NCCLS) [14] and the Clinical & Laboratory Standards Institute (CLSI) [15].

MATERIALS AND METHODS

a) Synthesis of ZnO NPs

Nanoparticles were synthesized by the coprecipitation method. A 4.46 mmol solution of zinc acetate (Sigma Aldrich, 99%) was prepared in 42 mL of methanol (Meyer, 99%) by magnetic stirring at 600 rpm and 60 °C. A 7.22 mmol solution of

potassium hydroxide (KOH) (Sigma Aldrich, 99%) was prepared in 23 ml of methanol as a precipitating agent. The resulting mixture was added dropwise to the zinc solution, followed by stirring at 600 rpm and 60 °C for 3 h. The white precipitate was washed with acetone and water, and then heated at 60 °C in an oven for 12 h.

b) Characterization of ZnO NPs and the hydrogel by XRD, FT-IR, and SEM

The ZnO nanoparticles were characterized by X-ray diffraction with a Bruker D8 Advance diffractometer, with a Cu kα source at 30 mA and 30 kV and a scanning speed of 1.2° steps/min (in the range of 10-80 2θ degrees). The size of the crystallites was determined by means of the Scherrer equation. FT-IR analysis of the samples was carried out in a PerkinElmer Frontier FT-IR spectrometer at a wavelength of 4000 to 400 cm^{-1}. Scanning electron microscope analysis of the ZnO NPs and the hydrogel were performed on a JEOL JSM 6100 SEM at 20 kV, after coating the materials with gold for 40 s.

c) Preparation of the HQT hydrogel

The concentration of the elements contained in the hydrogel was previously defined by considering the bactericidal effect. A 2% (w/v) solution of chitosan (Sigma Aldrich, at a medium molecular weight and 85% deacetylated) was prepared in 1 M glacial acetic acid (Sigma Aldrich) and stirred at 600 rpm until dissolved. Subsequently, ZnO NPs, K, and Mg were each adjusted to a concentration of 300 mM. KCl$_2$ and MgCl$_2$ (Sigma Aldrich, 99%) were the precursors of K and Mg. PLCL (Sigma Aldrich) at 0.2 % (w/v) was added and the mixture was stirred at 600 rpm for 12 h. The hydrogel was heated in an oven at 40 °C for 48 h to promote the crosslinking reaction.

d) Antibacterial evaluation

The antibacterial activity of the HQT hydrogel was assessed with *E. coli* ATCC® 25922 and *S. aureus* ATCC® 25923 by means of the disk diffusion (Kirby Bauer) method in BD Mueller Hinton agar, following the CLSI guidelines. The turbidity of the bacterial suspension was adjusted to a 0.5 McFarland standard (1.5x10^8 CFU/ml) and then incubated for 24 h at 37 °C. Inhibition was shown as a clear circular zone and the diameter was measured in mm, indicating bacterial susceptibility to the sample under study. BD BBL Sensi-DiscTM antimicrobial sensitivity test discs (Becton Dickinson) of amoxicillin/clavulanic acid (30 μg) were used as the positive control for inhibition.

RESULTS AND DISCUSSION

a) Characterization by XRD, FT-IR, and SEM

ZnO NPs were characterized by SEM and XRD (Figure 1). The micrograph (Figure 1a) of the surface of the ZnO powder, viewed at 5000X, displays agglomerates of particles with irregular morphology. By analyzing the energy-dispersive X-ray spectroscopy (EDS, Fig. 1b) and elemental mapping (Figs. 1c, d), peaks corresponding to oxygen and zinc were identified on the surface of the material. Hence, the synthesis was successful. Moreover, the product had no contaminants. The diffractogram (Fig. 1e) exhibits peaks corresponding to the zincite phase (according to PDF #04-003-2106) in space group P63mc, with lattice parameters a=3.25010Å and c=5.20710Å. Characteristic reflections were observed in the (100), (002), (101), (102), (110), (103), (112), and (202) lattice planes, similar to those found by Purwaningsih *et al.* 2016 [16]. The size of the crystallites was 30 nm, calculated with the Scherrer equation. No secondary phases were formed during synthesis.
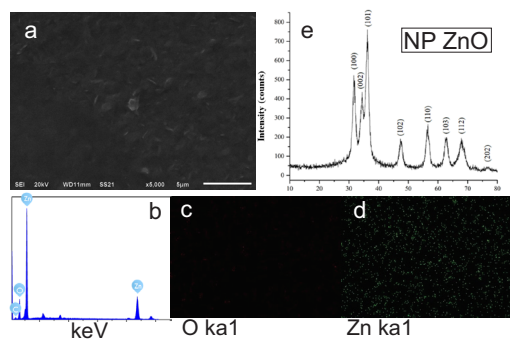
FIGURE 1. **Characterization of ZnO NPs:**
a) Surface micrograph at 5000X; b) EDS spectrum;
elemental mapping for c) oxygen and d) zinc;
and e) the XRD pattern.

The hydrogel was morphologically characterized by SEM before and after adding the trace elements and the ZnO NPs (Figure 2). Before adding anything, chitosan displayed a smooth texture and large pores distributed all along the surface (Figure 2.1 a). The porosity of the hydrogel is a critical factor since it allows for the anchoring of cells and the loading of different drugs, elements, or biologically relevant substances. After adding the trace elements and the ZnO NPs (Figure 2.2 a), the surface had a distinct appearance. The particles were coated by a chitosan matrix. By comparing the results of EDS and elemental mapping (Figs. 2.1 b and 2.2 b), it was possible to identify carbon (C), nitrogen (N), and oxygen (O) (Figs. 2.1 c, d and e) in the hydrogel without trace elements. With the addition of these elements, a good distribution of Mg, K, and Zn existed on the surface of the hydrogel (Figs. 2.2 c, d and e). A chlorine (Cl) peak was also found for the inadequately washed hydrogels.
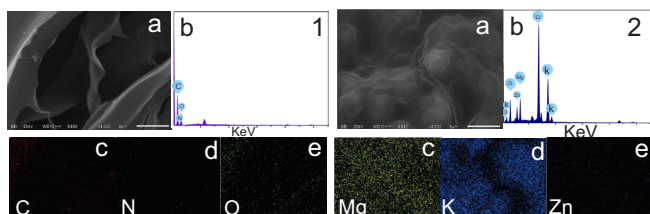
FIGURE 2. **SEM spectra of the hydrogel. 1) Before adding**
trace elements, and 2) after adding them. Micrographs (a),
EDS spectra (b), and elemental mapping (c, d, e, and f).

Correct washing eliminates the Cl residues derived from the precursors of the trace elements (KCl_2 and $MgCl_2$). During the microscopy analysis, no damaged or detached zones were detected on the hydrogel, which indicates that the physical crosslinking with PLCL was optimal.

The FT-IR spectra are shown for trace elements, PLCL, and the hydrogel (Figure 3). All samples were dissolved in 1 M acetic acid. The vibrational bands of ~3398-3300 cm^{-1} and 1637 cm^{-1} in spectra 1, 2, and 3 can be attributed to the OH group in the solvent [17]. The spectrum of chitosan (Figure 3.4) exhibits a band at ~3323 cm^{-1} for the OH/NH groups, at ~1644 cm^{-1} for C-N, at ~1392 cm^{-1} for C=O, and at ~1288 cm^{-1} for C-O-C (corresponding to amine 1), C-H vibrations, and C-C and C-O stretching (corresponding to amine 3), respectively [18] [19].
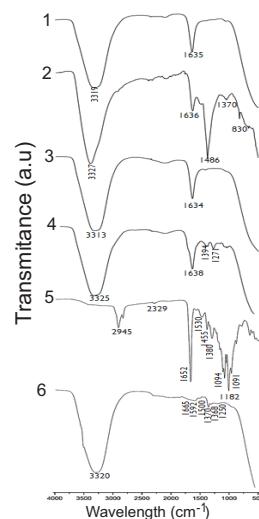
FIGURE 3. **FT-IR spectra for the Mg precursor (1),**
the K precursor (2), ZnO NPs (3), chitosan (4),
PLCL (5), and the HQT hydrogel (6).

The main contributions of PLCL are seen in Figure 3.5. The band at ~2980 cm^{-1} is assigned to alkyl stretching, at ~1750 cm^{-1} to carbonyl stretching, at ~1700 cm^{-1} to carbonyl ester stretching, and at ~1450 cm^{-1} to CH_2 bending. The bands at ~1380 cm^{-1} were ascribed to C=O, at ~1189 cm^{-1} and ~1182 cm^{-1} to C-O-O and asymmetric CH_2, and at ~1091 cm^{-1} to the stretching vibrations of C-O [20].

The FT-IR absorption bands of the HQT hydrogel (with all its components) are shown in Figure 3.6, observing a clear difference in the interaction of the functional groups. The bands at ~3300 cm^{-1} were designated as the NH$_2$ and OH groups, at ~1750 cm^{-1} as the stretching of the carbonyl groups in PLCL, at ~1600 cm^{-1} as the CH$_2$ and CH$_3$ groups, and at ~1250 cm^{-1} as a stretching of the C-O-C present in chitosan. Finally, the band at ~1420 cm^{-1} may be due to the chitosan CH$_2$ groups or PLCL-COO- groups [18] [19] [20].

b) Antibacterial activity

The antibacterial effect of the HQT hydrogel was evaluated with *E. coli* and *S. aureus*. The inhibition zones were more evident for *S. aureus* (25 mm for chitosan and 14 mm for ZnO NPs) than *E. coli* (14 mm for chitosan and 7 mm for ZnO NPs) (Figure 4). This result is attributed to the innate antimicrobial activity of chitosan and the oxidative stress caused by ZnO nanoparticles. Regarding the latter, reactive oxygen species (ROS) interact with the cell wall of bacteria and destroy the intracellular content, damaging proteins and lipids. Hence, positively charged nanoparticles bind to the negatively charged bacterial membrane, fomenting its disintegration or rupture [21]. Additionally, the size of ZnO NPs is effective against Gram-positive and Gram-negative bacteria because of the large surface area available to interact with the bacterial wall [22].
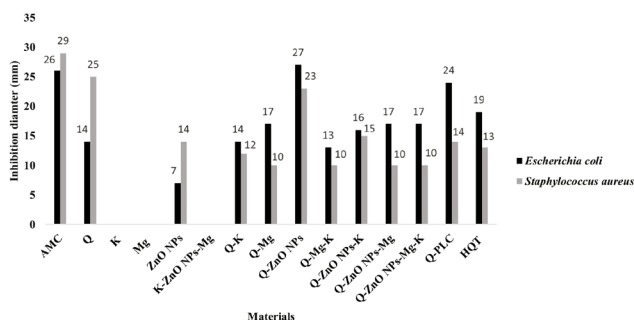
FIGURE 4. Inhibition zones (in mm) of *E. coli* and *S. aureus* exposed to the biomaterials herein tested.

For the biomaterials with trace elements, the inhibition of *E. coli* was more significant than that of *S. aureus*. The content of K and Mg affect the antibacterial activity of ZnO NPs, as can be appreciated by the lack of inhibition of both microorganisms. Concerning *E. coli*, the inhibition diameters resulting from K combined with Q (Q-K) materials were very similar to those found with chitosan alone (14 mm). The antibacterial effect of Q-K materials on *S. aureus* was reduced by about 50% (to 12 mm) (Figure 4).

K is required by microorganisms for the metabolism of carbohydrates, the activation of some enzymes, and bacterial osmoregulation [23]. Therefore, it is herein inferred that K was mainly used as a nutrient by the bacteria rather than a growth inhibitor. For *E. coli*, the inhibition diameter was greater with Q-Mg (17 mm) than chitosan alone (14 mm). Thus, Mg increased the antibacterial potential of chitosan. Mg and K did not show any antibacterial activity separately. They participate in vital functions as nutrients [23], which was probably their primary role. Q-PLCL generates a good antibacterial effect on *E. coli*, with an inhibition diameter of 24 mm. Finally, the HQT hydrogel significantly inhibited *S. aureus* (13mm) and *E. coli* (19mm), the latter being more susceptible.

The values of the inhibition diameters are observed in Figures 4 and 5. In both, the importance of the inhibitory activity of chitosan is evidenced by its greater inhibition diameter for all combinations. The concentration of 300 mM of the trace elements promoted bacterial inhibition in some of the materials. This concentration was determined in a previous study employing the same bacteria. The tests were conducted by means of the Kirby-Bauer method, exposing each bacteria to the biomaterials presently evaluated.

E. coli and *S. aureus* are common pathogens responsible for tissue infection. Due to the structural and chemical differences of their cell walls, it was relevant

to evaluate the inhibitory effect of the present biomaterials on both species [13]. According to the literature, chitosan, PLCL and ZnO NPs are non-toxic materials and have been used in various biomedical applications. The current results indicate that combining biomaterials on a chitosan hydrogel scaffold holds promise for combatting tissue infection caused by bacteria. Future research is necessary to examine the cytotoxicity of the hydrogel.
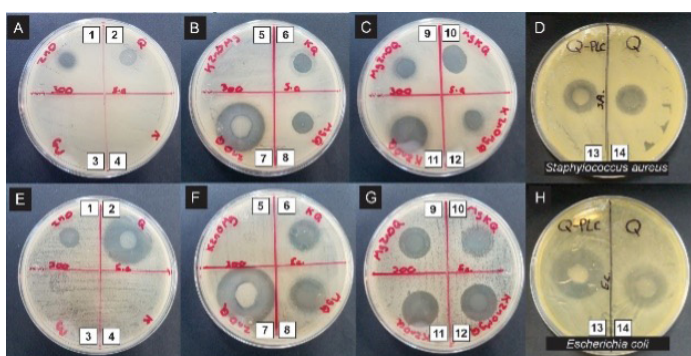
FIGURE 5. Results of the Kirby-Bauer method to examine the antibacterial effect of the HQT hydrogel with distinct combinations of trace elements and ZnO NPs. *S. aureus*: A, B, C, and D; *E. coli*: E, F, G, and H. 1) ZnO NPs; 2) Q; 3) Mg; 4) K; 5) K-ZnO NPs-Mg; 6) Q-K; 7) Q-ZnO NPs; 8) Q-Mg; 9) Q-ZnO NPs-Mg; 10) Q-Mg-K; 11) Q-ZnO NPs-K; 12) HQT; 13) Q-PLCL; and 14) Q.
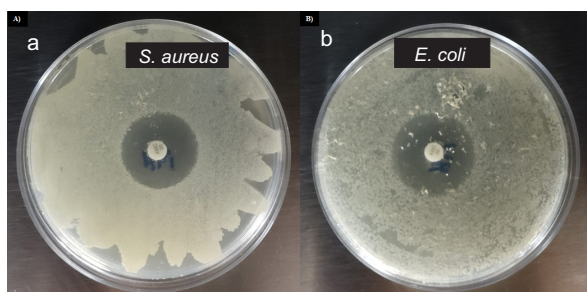
FIGURE 6. Inhibition produced by the antibiotic disc (the positive control), containing amoxicillin/clavulanic acid (30 μg). A) *S. aureus*; B) *E. coli*.

CONCLUSIONS

Zinc oxide nanoparticles of 30 nm were obtained in the zincite phase. It was possible to elaborate an adequately homogenized chitosan-based hydrogel physically cross-linked with PLCL and enriched with ZnO NPs as well as trace amounts of Mg and K. In vitro testing showed that this hydrogel has antibacterial activity. Since these biomaterials are organic, FDA-approved, and biocompatible with different biological systems, the resulting hydrogel represents a potentially useful antibiotic scaffold for tissue engineering.

ETHICAL STATEMENT

The test and experiments realized with bacteria are conducted under strict protocols and procedures approved internationally; before, during and after the test were carried out.

AUTHOR CONTRIBUTIONS

Y.A.S.D. designed the original project, carried out analyses like spectroscopic characterization, bacterial tests, contributed to the writing of the several stages of the manuscript, attended editorial reviews and provided materials and reagents. S.S.S. synthesized materials and carried out bacterial assays and spectroscopic characterization, participated in writing the original manuscript. G.G.E.B. participated in doing research and characterization of materials and in writing the original manuscript. E.L.Q. assisted in the analysis of the bacterial testing results and participated in writing the original manuscript. L.A.B.A. designed the original project, supervised, and validated the synthesis and characterization of the hydrogel, carried out several analyses and contributed to the writing of the several stages of the manuscript and attended editorial reviews and provided materials and reagents. All authors approved the final version of the manuscript.

REFERENCES

[1] Serrato Ochoa D, Nieto Aguilar R, Aguilera Méndez A. Ingeniería de tejidos. Una nueva disciplina en medicina regenerativa. Investig Cienc [Internet]. 2015;23(64):61-69. Available from: *https://www.redalyc.org/articulo.oa?id=67441039009*

[2] Abdulghani S, Mitchell GR. Biomaterials for In Situ Tissue Regeneration: A Review. Biomolecules [Internet]. 2019;9(11):750. Available from: **https://doi.org/10.3390/biom9110750**

[3] Gough JE, Scotchford CA, Downes S. Cytotoxicity of glutaraldehyde crosslinked collagen/poly(vinyl alcohol) films is by the mechanism of apoptosis. J Biomed Mater Res [Internet]. 2002;61(1):121-130. Available from: **https://doi.org/10.1002/jbm.10145**

[4] Patrulea V, Ostafe V, Borchard G, Jordan O. Chitosan as a starting material for wound healing applications. Eur J Pharm Biopharm [Internet]. 2015;97(Part B):417-26. Available from: **https://doi.org/10.1016/j.ejpb.2015.08.004**

[5] Ortega Cardona CE, Aparicio Fernández X. Quitosano: una alternativa sustentable para el empaque de alimentos. RDU [Internet]. 2020; 21(5):1-9. Available from: **https://doi.org/10.22201/cuaieed.16076079e.2020.21.5.4**

[6] He Y, Liu W, Guan L, Chen J, et al. A 3D-Printed PLCL Scaffold Coated with Collagen Type I and Its Biocompatibility. BioMed Res Int [Internet]. 2018;2018:5147156. Available from: **https://doi.org/10.1155/2018/5147156**

[7] Spears JW, Engle TE. Feed Ingredients: Feed Supplements: Microminerals. Encyclopedia of Dairy Sciences [Internet]. 2011. 378-383. Available from: **https://doi.org/10.1016/B978-0-08-100596-5.00760-5**

[8] Bhattacharya PT, Misra SR, Hussain M. Nutritional Aspects of Essential Trace Elements in Oral Health and Disease: An Extensive Review. Scientifica [Internet]. 2016;2016:5464373. Available from: **https://doi.org/10.1155/2016/5464373**

[9] Silva CS, Moutinho CG, Vinha AF, Matos CM. Trace Minerals in Human Health: Iron, Zinc, Copper, Manganese and Fluorine. Int J Sci Res Methodol [Internet]. 2019;13(3):57-80. Available from: *https://bdigital.ufp.pt/bitstream/10284/8105/1/5.Customer-IJSRM_HUMAN-13_8-19-27-08-2019%20%282%29.pdf*

[10] Gao C, Peng S, Feng P, Shuai C. Bone biomaterials and interactions with stem cells. Bone Res [Internet]. 2017;5:17059. Available from: **https://doi.org/10.1038/boneres.2017.59**

[11] Laurenti M, Cauda V. ZnO Nanostructures for Tissue Engineering Applications. Nanomaterials [Internet]. 2017;7(11):374. Available from: **https://doi.org/10.3390/nano7110374**

[12] Ribeiro M, Monteiro FJ, Ferraz MP. Infection of orthopedic implants with emphasis on bacterial adhesion process and techniques used in studying bacterial-material interactions. Biomatter [Internet]. 2012;2(4):176-194. Available from: **https://dx.doi.org/10.4161%2Fbiom.22905**

[13] Blanes JI, Clará A, Lozano F, Alcalá D, et al. Consensus document on the treatment of diabetic foot infections. Angiología [Internet]. 2012;64(1):31-59. Available from: **https://doi.org/10.1016/j.angio.2011.11.001**

[14] National Committee for Clinical Laboratory Standards. Methods for determining bactericidal activity of antimicrobial agents: approved guideline [Internet]. Wayne, PA: National Committee for Clinical Laboratory Standards; 1999. Available from: *https://webstore.ansi.org/preview-pages/CLSI/preview_M26-A.pdf*

[15] Clinical and Laboratory Standards Institute. Performance Standards for Antimicrobial Susceptibility Testing. CLSI supplement M100 [Internet]. Wayne, PA: Clinical and Laboratory Standards Institute; 2017. Available from: *https://file.qums.ac.ir/repository/mmrc/clsi%202017.pdf*

[16] Purwaningsih SY, Pratapa S, Triwikantoro, and Darminto. Nano-sized ZnO powders prepared by co-precipitation method with various pH. AIP Conf Proc [Internet]. 2016;1725:020063.1-020063.6. Available from: **https://doi.org/10.1063/1.4945517**

[17] Colomer MT. Straightforward synthesis of Ti-doped YSZ gels by chemical modification of the precursors alkoxides. J Sol-Gel Sci Technol [Internet]. 2013;67:135-144. Available from: **https://doi.org/10.1007/s10971-013-3059-9**

[18] Maldonado Lara K, Luna Bárcenas G, Luna Hernández E, Padilla Vaca, et al. Preparation and characterization of Copper Chitosan Nanocomposites with Antibacterial Activity for Applications in Tissue Engineering. Rev Mex Ing Biomed [Internet]. 2017;38(1):306-313. Available from: **https://dx.doi.org/10.17488/RMIB.38.1.26**

[19] Varma R, Vasudevan S. Extraction, Characterization, and Antimicrobial Activity of Chitosan from Horse Mussel Modiolus modiolus. ACS Omega [Internet]. 2020;5(32):20224–20230. Available from: **https://doi.org/10.1021/acsomega.0c01903**

[20] Garkhal K, Verma S, Jonnalagadda S, Kumar N. Fast degradable poly(L-lactide-co-e-caprolactone) microspheres for tissue engineering: Synthesis, characterization, and degradation behavior. J Polym Sci A: Polym Chem [Internet]. 2007;45(13):2755–2764. Available from: **https://doi.org/10.1002/pola.22031**

[21] Zavaleta EG, Saldaña JJ, Jáuregui RSR, Pacherrez GMD, et al. Antibacterial effect of ZnO nanoparticles on Staphylococcus aureus and Salmonella typhi. Arnaldoa [Internet]. 2019;26(1):421-432. Available from: **http://dx.doi.org/10.22497/arnaldoa.261.26122**

[22] Yamamoto O. Influence of particle size on the antibacterial activity of zinc oxide. Int J Inorg Mater [Internet]. 2001;3(7):643-646. Available from: **https://doi.org/10.1016/S1466-6049(01)00197-0**

[23] Stautz J, Hellmich Y, Fuss MF, Silberberg JM, et al. Molecular Mechanisms for Bacterial Potassium Homeostasis. J Mol Biol [Internet]. 2021;433(16):166968. Available from: **https://doi.org/10.1016/j.jmb.2021.166968**

Effect of the Unilateral Breast Cancer Surgery on the Shoulder Movement: Electromyographic and Motion Analysis

Efecto de la cirugía unilateral del cáncer de mama en el movimiento del hombro: análisis electromiográfico y de movimiento

Israel Miguel-Andrés[1] (iD), Silvia Beatríz García-González[2] (iD), José de Jesús Mayagoitia-Vázquez[1] (iD),

Karla Barrera-Beltrán[3] (iD), Didier Samayoa-Ochoa[4] (iD), Miguel León-Rodríguez[5] (iD), Leonardo Azael García-García[6] (iD)

[1]Centro de Innovación Aplicada en Tecnologías Competitivas (CIATEC, A. C.)

[2]Clinical Research, University of Guanajuato, León, Guanajuato, México

[3]Hospital Regional de Alta Especialidad del Bajío, León, Guanajuato, México

[4]ESIME Zacatenco, Instituto Politécnico Nacional, México City, México

[5]Universidad Politécnica de Guanajuato, Campus Cortazar, Guanajuato, México

[6]University of Sussex, Falmer, Brighton, United Kingdom

ABSTRACT

After breast cancer surgery, women might develop musculoskeletal impairments that affect movements of the upper limbs and reduce the quality of life. The objective of this research was to analyze the effect of the unilateral breast cancer surgery on the kinematics of the shoulder and the electrical activity of the upper trapezius, middle deltoid and pectoralis major muscles. Eight right-handed female participants, mean age 46.5 ± 5.45 years and mean body mass 71.21 ± 13.33 kg, with unilateral breast cancer surgery, without breast reconstruction and without lymphedema symptoms were included in the research. Flexion-extension and abduction-adduction movements of the shoulder were evaluated with infrared cameras and the electrical activity was measured using surface electromyography. The statistical analysis of the direction angles showed a significant reduction of the flexion-extension and abduction-adduction movements in the affected side in most of the participants (p<0.05). The muscle electrical activity did not present a significant difference between the two sides for the flexion-extension and abduction-adduction movements (p>0.05). The results suggest that the surgical procedure could compromise the range of motion of the affected side. Furthermore, this research contributes to clarify the effect of the surgical procedure in the range of motion of the upper limbs.

KEYWORDS: Breast cancer, Electromyography, Mastectomy, Shoulder, Rehabilitation

RESUMEN

Después de la cirugía de cáncer de mama, las mujeres pueden desarrollar deficiencias musculoesqueléticas que afectan los movimientos de las extremidades superiores y reducen la calidad de vida. El objetivo de esta investigación fue analizar el efecto de la cirugía unilateral del cáncer de mama sobre la cinemática del hombro y la actividad eléctrica de los músculos trapecio superior, deltoides medio y pectoral mayor. Se incluyeron ocho participantes diestras, edad promedio 46.5 ± 5.45 años y masa promedio 71.21 ± 13.33 kg, con cirugía de cáncer de mama unilateral, sin reconstrucción mamaria y sin síntomas de linfedema. Los movimientos de flexión-extensión y abducción-aducción del hombro se evaluaron con cámaras infrarrojas y se midió la actividad eléctrica mediante electromiografía de superficie. El análisis estadístico de los ángulos de dirección mostró una reducción significativa del movimiento de flexión-extensión y abducción-aducción en el lado afectado en la mayoría de las participantes ($p<0.05$). La actividad eléctrica muscular no presentó diferencia significativa entre los dos lados para los movimientos de flexión-extensión y abducción-aducción ($p>0.05$). Los resultados sugieren que el procedimiento quirúrgico podría comprometer el rango de movimiento del lado afectado. Además, esta investigación contribuye a esclarecer el efecto del procedimiento quirúrgico en el rango de movimiento de los miembros superiores.

PALABRAS CLAVE: Cáncer de mama, Electromiografía, Mastectomía, Hombro, Rehabilitación

Corresponding author

TO: **Israel Miguel-Andrés**

INSTITUTION: **Centro de Innovación Aplicada en Tecnologías Competitivas (CIATEC, A. C.)**

ADDRESS: **Omega #201, Col. Industrial Delta, C. P. 37545, León, Guanajuato, México**

CORREO ELECTRÓNICO: **imiguel@ciatec.mx**

INTRODUCTION

Breast cancer is the most common type of cancer in women in the world, with an incident of 1.7 million of new cases in 2016 [1]. For women, it was the most common cancer in 131 countries and cause of cancer deaths in 112 countries [1] [2] [3] [4] [5] [6]. In 2018 the International Agency for Research on Cancer estimated 2.08 million of new breast cancer cases worldwide [7].

After breast cancer surgery, women might develop musculoskeletal impairments that affect movements of the upper limbs and reduce the quality of life. Complications following breast cancer surgery include infection, swelling, hematoma, seroma and psychological factors such as, anxiety or depression [3] [8] [9] [10] [11]. The complications are not always localized on the region of the surgery, as many of the treatments have larger regional systemic effects on body structures and functions [3] [8] [11] [12] [13]. Although women report upper limb symptoms between 6 months and 3 years after breast cancer, some of the comorbidities could remain for a longer-term. The etiology of morbidity seems to be multifactorial, with the most consistent risk factors being those associated with extension of cancer treatment [14].

The mastectomy produces dysfunctions on the upper limbs in a mid or long term, causes lymphedema, persistent pain [9] [15], weakness and restricts the movement of the shoulder [10] [14] [16]. Furthermore, it has been found that muscle activation can be affected after breast cancer surgery. The effect depends on the type of surgery and type of reconstruction of the breast [17] [18] [19] [20] [21]. It has been thought that the most frequent complications include long-term weakening of muscles within the shoulder and upper limb at the affected side [4]. It is believed that if one muscle is compromised, then other muscles might become more active to compensate for the lost movement. However, the muscle electrical activity can be influenced by age, dominance or pain on the limb [20].

Movements of the upper limbs and head are recommended as rehabilitation after a breast cancer surgery. Upper-body morbidity may be treatable with physical therapy. It has been found a 50-53% reduction in the risk of breast cancer deaths in women who are physically active after a breast cancer diagnosis [6] [14]. Although rehabilitation represents an alternative to reduce the complication after breast cancer surgery, many of the patients do not receive the appropriate treatment to address the complications [22] [23] [24].

The complications after mastectomy are well known, evaluated and treated from measurements such as goniometry, observation and strength tests with manual resistance [8] [10]. However, they do not provide specific scenarios for kinematic discontinuities of the shoulder movement. Moreover, there are few studies focused on the analysis of the biomechanics of the upper limbs on a three-dimensional space after breast cancer treatment [20] [25] [26] [27]. Biomechanical and muscular activation studies with equipment with higher accuracy are required to recognize these affectations and identify areas of opportunity to improve physiotherapeutic intervention plans.

Therefore, the objective of this research is to analyze the movement of the shoulder and the electrical activity of the trapezius, deltoid and pectoralis major muscles in patients with unilateral breast cancer surgery.

MATERIALS AND METHODS

Experimental protocol

Eight right-handed female participants, mean age 46.5 ± 5.45 years and mean body mass 71.21 ± 13.33 kg with unilateral breast cancer surgery (mastectomy), without breast reconstruction and without lymphedema symptoms after the surgery were included in the research, see Table 1. The sampled population was selected with non-probabilistic sampling. After the surgery, all the participants performed a rehabilitation

process of the upper limbs. This rehabilitation was performed for 60 days and involved series of active movements of the head, flexion-extension and abduction-adduction of the arms. Participants which could not follow instruction, presented post-surgery issues or did not complete the rehabilitation were excluded.

TABLE 1. Anthropometric data and affected side of the patients. SD means Standard Deviation.

Subject	Age (years)	Mass (kg)	Height (m)	Affected Arm	Dominant Hand
1	36	61.35	1.62	Left	Right
2	50	53.6	1.5	Right	Right
3	50	57.6	1.48	Right	Right
4	51	82.3	1.56	Left	Right
5	45	64.05	1.55	Right	Right
6	52	84.3	1.64	Right	Right
7	42	86.1	1.72	Left	Right
8	46	80.4	1.6	Right	Right
Mean	46.50	71.21	1.58	--	--
SD	5.45	13.33	0.078	--	--

Once the rehabilitation was completed, the participants continue with the evaluation of the flexion-extension, abduction-adduction movements and the electrical activity of the upper trapezius, middle deltoid, and pectoralis major muscles. The motion of the arms was measured with seven infrared cameras of the VICON system at a sampling frequency of 100Hz (Nexus version 2.8.1.111866h x86, Vicon Motion System Ltd. Oxford UK). The muscle electrical activity was measured with surface electromyography (EMG) at a sampling frequency of 1000Hz (Myomonitor IV EMG System Bagnoli Delsys Inc, Boston MA, USA).

All the participants were asked to wear comfortable clothes to allow free execution of the movements. The participants were informed about the function and main parts of the motion capture system and the EMG equipment. They were allowed to perform exercises prior to the experimental tests to familiarize themselves with the equipment and the protocol. Simultaneously, personal data were recorded and saved on an encrypted computer for safekeeping. Then, the participants performed three trials of bilateral flexion-extension and abduction-adduction movement of the arms. Each trial consisted of ten cycles performed over a period of 20 seconds paced using a metronome. Three minutes were allowed among trials to give rest to the patients and avoid fatigue.

Subject preparation

First, the setup of the infrared cameras of the VICON system was performed. Then, 39 spherical markers (10mm of diameter) were placed on anatomical bony landmarks of each participant, Figure 1a. The passive markers (inactive) were attached to the skin with double-sided tape following the VICON manual and the markers were labeled following the PlugInGait FullBody template. Thereafter, the skin on the upper trapezius, middle deltoid and pectoralis major muscles was cleaned with exfoliating cream and isopropyl alcohol for the placement of the electrodes. The placement of the electrodes was done following the recommendations of Surface Electromyography for the Non-Invasive Assessment of Muscles (SENIAM). Furthermore, a ground/reference electrode was placed on the lateral epicondyle of the left arm.

Data processing

The data of the markers were exported to Matlab R2015a (version 8.5.0.197613, The MathWorks Inc., Natick, Massachusetts, USA) in a txt file for processing. An orthogonal coordinate system was created in the 10th thoracic vertebra (T10) using the markers of the 7th cervical vertebra (C7) and the sternum (STRN). The *X* axis pointed to the lateral side, the Y axis pointed backwards and the *Z* axis pointed upwards as shown in Figure 1b. Then, a rotation matrix 3x3 with the three-unit vectors was created. Furthermore, a vector was created between the upper arm and the elbow markers in order to describe the movement of
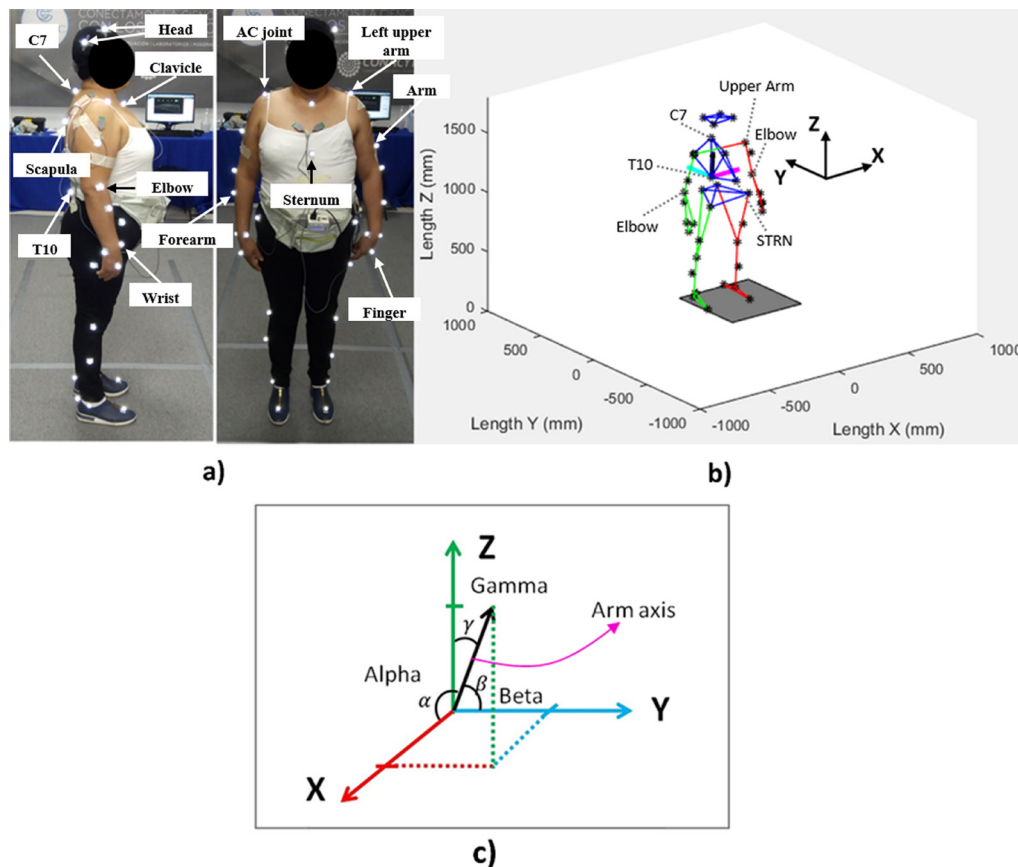
FIGURE 1. An orthogonal coordinate system on the thorax was created as a reference system for measuring the rotation of both arms: a) Patient preparation, b) Isometric view of the markers, and c) Direction angles for the arm axis.

the arm. Finally, the vector of each arm was orientated with respect to the coordinate system of the thorax. This was done by multiplying the inverse matrix times the vector of the arm. Once the transformation of the vector was done, the direction angles Alpha (X), Beta (Y) and Gamma (Z) were calculated as shown in Figure 1c. All the cycles from the three trials undertaken by each participant for each motion were averaged and time normalized from zero to 100% of the movement time.

The raw EMG data was filtered with a 2-pole zero-lag Butterworth band pass filter with cut-off frequencies of 5 and 400Hz in order to retain as much as possible of the electrical activity data and reject high frequency noise. The cut-off frequencies were obtained from a frequency spectrum analysis of the raw EMG data [28]. Then, the root mean square (RMS) value of every muscle burst for all the trials was calculated within a window of 100ms. The RMS window was calculated at the maximum peak of each burst (50ms forwards and 50ms backwards). Finally, the RMS values of the muscles were averaged and then, the healthy side was compared versus the affected side.

Statistical analysis

In order to determine the effect of the unilateral breast cancer surgery on the shoulder, a Student's t-test for dependent samples was performed. The comparison of the direction angles and the electrical activity of the muscles was done for both sides. The significance level was taken to be $p < 0.05$.

RESULTS AND DISCUSSION

Flexion-Extension movement

The direction angles from Figure 2a show the movement of the arms during the flexion-extension motion (subject 8). As the movement is executed mainly in the sagittal plane, the direction angle of the X axis (alpha) does not change significantly. However, the movement of the arms with respect to the Y and Z axes (beta and gamma) changes. Figure 2a shows that the affected arm (subject 8-right arm) reduces the direction angles (beta and gamma) when the arm is reaching the maximum elevation level. The direction angle with respect to the Y axis at 50% of the cycle was 118.52 ± 5.28 and 136.76 ± 2.56 degrees for the left and right arm respectively. This means that the right arm (affected) does not elevate as much as the left arm.

Similarly, the comparison of both arms with respect to the vertical Z axis showed that the right arm did not elevate as much as the left one. The direction angle with respect to the vertical Z axis at 50% of the cycle was 28.77 ± 4.98 and 48.27 ± 2.45 degrees for the left and right arm respectively, Figure 2a.
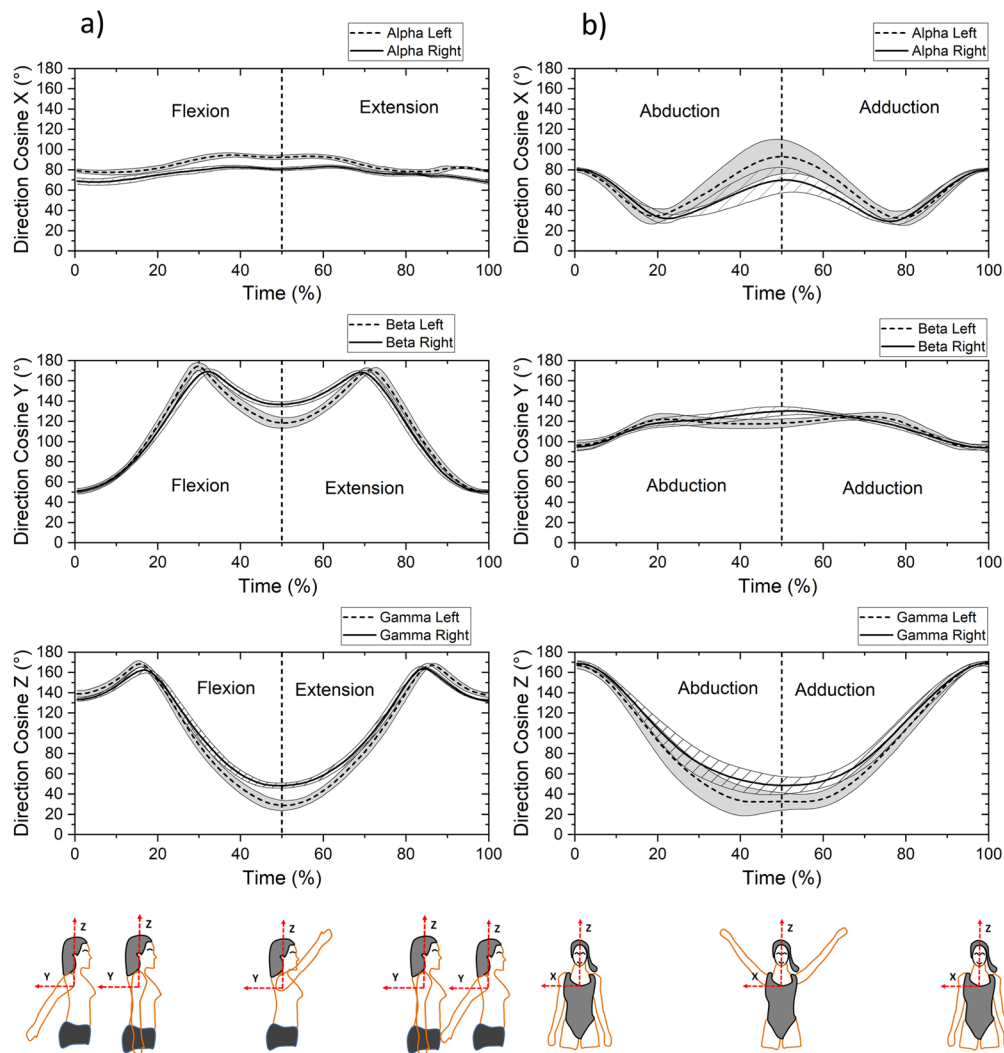

FIGURE 2. **a) Direction angles of the flexion-extension movement of one subject and b) Direction angles of the abduction-adduction movement of one subject. Comparison of both sides, affected and non-affected side (Subject 8).**

Table 2 shows the mean and standard deviation values (alpha, beta and gamma) of the eight subjects during the flexion-extension motion of both arms. In general, it was found that the affected side presented less amplitude of motion, excluding subject 5. The statistical analysis showed a significant reduction of the movement in the affected side ($p < 0.05$).

Abduction-Adduction movement

Figure 2b shows the three direction angles (alpha, beta and gamma) of the abduction-adduction movement of the arms in subject number 8. The movement was performed mainly in the frontal plane. Therefore, the beta angle behaved almost like a flat line. Thinking that the major effect of the surgery could be found at the maximum elevation level of the arms, the analysis of the direction angles was done at 50% of the cycle. The direction angle with respect to the X axis at 50% of the cycle for this subject was 92.95 ± 16.81 and 69.9 ± 12.65 degrees for the left and right arm respectively. This means that the right arm (affected) does not elevate as much as the left arm. Similarly, the comparison of both arms with respect to the vertical Z axis showed that the right arm did not elevate as much as the left one. The direction angle with respect the Z axis at the 50% of the cycle was 32.67 ± 8.61 and 48.55 ± 8.86 degrees for the left and right arm respectively, Figure 2b.

The mean and standard deviation values (direction angles) of the eight subjects during the abduction-adduction movement are presented in Table 2. The gamma angles at 50% of the cycle motion indicate that the affec-

TABLE 2. Direction angles of the flexion-extension and abduction-adduction movement of all participants. The mean and standard deviation values are from the 50% of the cycle motion.

Direction angles: Flexion-Extension movement									
	ALPHA (°)		*p*	BETA (°)		*p*	GAMMA (°)		*p*
Subject	Left (SD)	Right (SD)	0.05	Left (SD)	Right (SD)	0.05	Left (SD)	Right (SD)	0.05
1	56.72 (3.02)	48.02 (2.84)	0.000	116.86 (2.95)	97.72 (1.94)	0.000	45.44 (2.84)	43.06 (2.77)	0.000
2	84.24 (1.14)	86.86 (3.81)	0.010	108.52 (5.86)	113.87 (7.21)	0.000	19.6 (5.45)	24.6 (6.30)	0.000
3	71.60 (2.31)	77.65 (1.60)	0.000	114.35 (2.25)	144.61 (1.98)	0.000	31.32 (3.18)	57.48 (1.83)	0.000
4	56.86 (1.44)	82.71 (0.90)	0.000	117.09 (1.70)	115.47 (4.05)	0.030	45.4 (1.52)	26.71 (3.75)	0.000
5	77.95 (3.00)	86.51 (1.14)	0.000	135.59 (4.11)	124.2 (2.70)	0.000	48.23 (3.19)	34.46 (2.71)	0.000
6	83.21 (3.33)	70.92 (2.55)	0.000	139.62 (9.20)	144.82 (6.78)	0.000	50.63 (8.82)	61.92 (6.47)	0.000
7	62.19 (3.48)	81.98 (2.52)	0.000	125.71 (2.34)	115.24 (3.71)	0.000	48.49 (2.52)	26.8 (3.50)	0.000
8	92.43 (2.18)	80.79 (1.57)	0.000	118.52 (5.28)	136.76 (2.56)	0.000	28.77 (4.98)	48.27 (2.45)	0.000
Direction angles: Abduction-Adduction movement									
	ALPHA (°)		*p*	BETA (°)		*p*	GAMMA (°)		*p*
Subject	Left (SD)	Right (SD)	0.05	Left (SD)	Right (SD)	0.05	Left (SD)	Right (SD)	0.05
1	29.30 (3.81)	31.66 (3.32)	0.008	101.42 (2.64)	78.45 (2.27)	0.000	63.52 (3.47)	61.11 (4.05)	0.007
2	102.43 (2.61)	116.24 (3.47)	0.000	102.48 (2.92)	111.99 (2.96)	0.000	17.88 (3.31)	35.5 (3.90)	0.000
3	21.52 (3.97)	32.36 (2.48)	0.000	101.51 (2.30)	121.09 (1.70)	0.000	72.21 (3.81)	82.99 (4.45)	0.000
4	60.40 (2.29)	90.07 (0.91)	0.000	116.33 (2.75)	113.71 (2.23)	0.000	41.7 (1.96)	23.73 (2.22)	0.000
5	80.88 (2.82)	82.46 (2.21)	0.030	119.86 (1.23)	114.53 (1.10)	0.000	31.64 (1.29)	25.9 (1.13)	0.000
6	78.60 (10.92)	64.29 (7.01)	0.000	118.04 (2.19)	126.53 (4.96)	0.000	32.23 (6.52)	48 (1.14)	0.000
7	47.36 (11.7)	73.82 (15.15)	0.000	115.01 (5.63)	110.63 (4.71)	0.000	53.62 (9.08)	28.8 (10.90)	0.000
8	92.95 (16.81)	69.9 (12.65)	0.000	118.23 (4.22)	130.08 (4.37)	0.000	32.67 (8.61)	48.55 (8.85)	0.000

ted arm does not elevate as much as the non-affected arm, excluding subject 5. Similarly, the direction angle alpha indicates that the affected arm does not elevate as much as the opposite one, excluding subjects 2, 3, and 5. The statistical analysis showed a significant reduction of the movement in almost all affected sides ($p < 0.05$).

Muscle electrical activity during the flexion-extension movement

For flexion-extension movement, the trapezius showed the highest electrical activity followed by the deltoid muscle. Although the electrical activity was higher in some cases, the statistical analysis did not show a significant difference, as shown in Table 3 ($p > 0.05$). The trapezius in subject one was the only muscle with a significant statistical difference between the affected and non-affected side ($p = 0.047$). However, there was not a specific trend of the data to justify that the affected side increases or decreases the electrical activity after the rehabilitation post-surgery.

Muscle electrical activity during the abduction-adduction movement

The RMS and the standard deviation values of the three muscles during the abduction-adduction movement are registered in Table 3. Although it was expected to find a significant difference among the muscles, the statistical analysis did not show a significant effect. The electrical activity of the trapezius muscle in subject one presented a significant statistical difference ($p = 0.043$). However, it could not be established a specific trend of the EMG behavior.

TABLE 3. **Root mean square values of the electrical activity during the flexion-extension and abduction-adduction movement.**

RMS of the EMG: Flexion-Extension movement											
	TRAPEZIUS (mV)		*p*	DELTOID (mV)		*p*	PECTORALIS (mV)		*p*
Subjects	Left (SD)	Right (SD)	0.05	Left (SD)	Right (SD)	0.05	Left (SD)	Right (SD)	0.05
1	0.411 (0.089)	0.139 (0.018)	0.047	0.043 (0.019)	0.021 (0.008)	0.669	0.010 (0.005)	0.015 (0.005)	0.839
2	0.362 (0.057)	0.175 (0.044)	0.072	0.195 (0.058)	0.200 (0.051)	0.930	0.009 (0.002)	0.011 (0.002)	0.869
3	0.061 (0.009)	0.069 (0.026)	0.894	0.057 (0.015)	0.065 (0.017)	0.846	0.026 (0.015)	0.014 (0.007)	0.740
4	0.277 (0.038)	0.141 (0.042)	0.170	0.099 (0.015)	0.025 (0.008)	0.153	0.006 (0.005)	0.006 (0.002)	0.997
5	0.204 (0.039)	0.099 (0.025)	0.240	0.041 (0.006)	0.027 (0.004)	0.665	0.010 (0.006)	0.018 (0.004)	0.794
6	0.146 (0.014)	0.151 (0.035)	0.940	0.037 (0.007)	0.030 (0.010)	0.824	0.007 (0.002)	0.008 (0.002)	0.966
7	0.234 (0.055)	0.170 (0.028)	0.509	0.059 (0.009)	0.071 (0.010)	0.797	0.041 (0.010)	0.011 (0.004)	0.397
8	0.091 (0.013)	0.108 (0.015)	0.682	0.035 (0.006)	0.020 (0.005)	0.705	0.018 (0.004)	0.007 (0.003)	0.709
RMS of the EMG: Abduction-Adduction movement											
	TRAPEZIUS (mV)		*p*	DELTOID (mV)		*p*	PECTORALIS (mV)		*p*
Subjects	Left (SD)	Right (SD)	0.05	Left (SD)	Right (SD)	0.05	Left (SD)	Right (SD)	0.05
1	0.389 (0.077)	0.144 (0.019)	0.043	0.061 (0.014)	0.112 (0.067)	0.609	0.017 (0.008)	0.015 (0.006)	0.935
2	0.246 (0.064)	0.159 (0.057)	0.348	0.159 (0.056)	0.160 (0.028)	0.992	0.007 (0.002)	0.008 (0.002)	0.930
3	0.117 (0.013)	0.036 (0.008)	0.059	0.077 (0.010)	0.064 (0.013)	0.787	0.003 (0.001)	0.004 (0.002)	0.972
4	0.357 (0.055)	0.218 (0.019)	0.143	0.144 (0.023)	0.028 (0.003)	0.061	0.006 (0.005)	0.005 (0.001)	0.975
5	0.250 (0.059)	0.103 (0.018)	0.092	0.054 (0.010)	0.060 (0.010)	0.882	0.009 (0.005)	0.019 (0.022)	0.845
6	0.147 (0.031)	0.141 (0.055)	0.933	0.056 (0.014)	0.074 (0.014)	0.703	0.009 (0.005)	0.013 (0.005)	0.894
7	0.250 (0.059)	0.181 (0.023)	0.478	0.061 (0.009)	0.073 (0.012)	0.770	0.040 (0.031)	0.010 (0.006)	0.613
8	0.116 (0.018)	0.115 (0.016)	0.986	0.054 (0.007)	0.039 (0.005)	0.653	0.007 (0.003)	0.007 (0.003)	0.990

The results show the effect of the breast cancer surgery on the shoulder movement and the muscle electrical activity between the affected and non-affected side. There was a significant reduction of the range of motion (ROM) in the affected side in most of the patients for flexion-extension and abduction-adduction movements. These outcomes agree with other studies which have reported the reduction of the ROM during the first year after breast cancer surgery [10] [11] [14] [27] [29]. Furthermore, the reduction of the ROM could restraint the performance of some activities and then, have an impact on the quality of life of the patients [8] [9] [10] [26]. It has been mentioned that the scar tissue formation and protecting posturing after the breast cancer surgery could lead to shortening of the anterior chest wall. Therefore, the reduction of the ROM of the upper limbs found in this study could be related to the shortening of the breast chest [13] [16].

Some studies have found a significant reduction in the ROM of the upper limbs after breast cancer surgery using goniometry [8] [10] [17]. Our study used infrared cameras and provided more accuracy and a deeper analysis of the ROM of the shoulder joint in the sagittal and frontal planes. Although the markers and electrodes could produce discomfort to the participants, time and practice of movements were given to get used to the materials and perform the movements in a natural way. It has been reported that the mayor impairments in the upper limbs occur in the first or second year after the surgery. The development of the current study two months after the surgery allows us to identify the effects of the surgery on the kinematics of the shoulder in a short term. In a longer period of time, the effects of breast cancer surgery could be hidden due to the fact that the patients tend to adopt strategies and try to cope with the morbidities [10] [11].

The electrical activity of the muscles did not present a significant difference between the affected and non-affected side. Perhaps this could be produced due to the fact that the patients unconsciously try to elevate the upper limbs without too much effort. Furthermore, from the anthropometric data (Table 1), most of the participants were overweight or obese. We believe that overweight or obese participants will have different muscle electrical activity than the normal weight participants as the fat tissue could attenuate the EMG signal. This could be hidden the real effect of the muscle electrical activity when the affected and non-affected sides are compared. On the other hand, it has been suggested that humeral elevation of the arm, upward movement on the affected side, and left shoulder movement will increase the electrical activity of the muscles regardless of which side is affected [17]. Some studies have found significant difference in the EMG activity and muscle strength reduction after breast cancer surgery [19] [21] [30]. Although our study considers patients without pain, all of them were treated with coadjutant therapy (chemotherapy), which could have an effect on the electrical activity [18] [21]. Furthermore, it has been found that the EMG activity depends on parameters such as age, dominant hand, affected side, type of surgery, abnormal activation patterns and breast cancer treatment [17].

It has been recognized that exercise training part of the rehabilitation program will reduce the risk of breast cancer deaths in women who are physically active after breast cancer diagnosis [6]. Therefore, it is recommended to continue with the practice of physical therapy for improving the ROM of the affected side [6]. Although there are several studies related to the upper limb dysfunction after breast cancer surgery [4] [10] [11] [23], to the authors knowledge, this is the first study developed in the female Mexican population using infrared cameras and reflective markers. In addition, the results found in the study provide new knowledge to understand the impact of the breast cancer surgery on the upper limb dysfunction, so understanding the kinematics and electromyogra-

phy of the upper limbs could help practitioners to improve patient education and influence treatment decisions [31].

The current study presents some limitations. First, the results cannot be generalized due to the sample size considered in the analysis. Second, some of the complications after mastectomy occur in a longer period of time, therefore, the results found in this study in the first two months could have a different effect beyond this date. Third, although different search engines were used to seek articles related to the research (google scholar, web of science and ScienceDirect), few works with conclusive information were found, making a comparison of the results difficult. However, although there are some limitations in the study, the results indicate a clear significant trend in the reduction of the ROM of the affected side after two months of the mastectomy, mainly when the arm is trying to reach the maximum elevation level. In future work, we expect to develop a study comparing the kinematics of the upper limbs before and after the surgical procedure. Furthermore, a sample of healthy participants without surgery but with similar demographic and anthropometric characteristics will be considered in the study.

CONCLUSIONS

The results suggest that the surgical procedure could compromise the range of motion of the affected side. This research contributes to clarify the effect of the surgical procedure in the ROM of the upper limbs after two months and provides new knowledge to understand the biomechanics of the upper limbs after mastectomy. Furthermore, from the results found in this study, it is reasonable that the patients with breast cancer surgery continue the rehabilitation program for a longer period of time.

AUTHOR CONTRIBUTIONS

ACKNOWLEDGEMENTS

ETHICAL STATEMENT

The participants were informed about the procedures, risks and benefits in order to obtain the informed consent of voluntary participation, in accordance with the General Health Law of Mexico, and taking care of the principles of the Declaration of Helsinki [32]. The protocol was approved by the ethics and research committee of the Hospital Regional de Alta Especialidad del Bajío (approval number CI/HRAEB/001/2019).

CONFLICT OF INTEREST

The authors declare that they have no conflict of interest.

REFERENCES

[1] Sharma R. Breast cancer incidence, mortality and mortality-to-incidence ratio (MIR) are associated with human development, 1990-2016: evidence from Global Burden of Disease Study 2016. Breast Cancer [Internet]. 2019;26(4):428-445. Available from: **https://doi.org/10.1007/s12282-018-00941-4**

[2] Dey B, Kumar A. A review article on breast Cancer. Int J Pharm Pharm Res [Internet]. 2018;11(2):284-98. Available from: *https://ijppr.humanjournals.com/wp-content/uploads/2018/02/25. Biplob-Dey-Arun-Kumar.pdf*

[3] Smoot B, Wampler M, Topp KS. Breast Cancer Treatments and Complications: Implications for Rehabilitation. Rehabil Oncol [Internet]. 2009;27(3):16-26. Available from: **https://doi.org/10.1097/01893697-200927030-00004**

[4] Liszka M, Samborski W. Assessment of biomechanical parameters of the shoulder joint at the operated side versus non-operated side in patients treated surgically for breast cancer. Rep Pract Oncol Radiother [Internet]. 2018;23(5):378-383. Available from: **https://doi.org/10.1016/j.rpor.2018.07.001**

[5] Global Burden of Disease Cancer Collaboration. Global, Regional, and National Cancer Incidence, Mortality, Years of Life Lost, Years Lived With Disability, and Disability-Adjusted Life-Years for 29 Cancer Groups, 1990 to 2016: A Systematic Analysis for the Global Burden of Disease Study. JAMA Oncol [Internet]. 2018;4(11):1553-1568. Available from: **https://doi.org/10.1001/jamaoncol.2018.2706**

[6] Volaklis KA, Halle M, Tokmakidis SP. Exercise in the prevention and rehabilitation of breast cancer. Wien Klin Wochenschr [Internet]. 2013;125:297-301. Available from: **https://doi.org/10.1007/s00508-013-0365-8**

[7] Bray F, Ferlay J, Soerjomataram I, Siegel RL, et al. Global cancer statistics 2018: GLOBOCAN estimates of incidence and mortality worldwide for 36 cancers in 185 countries. CA Cancer J Clin [Internet]. 2018;8:(6):394-424. Available from: **https://doi.org/10.3322/caac.21492**

[8] Hayes SC, Rye S, Battistutta D, DiSipio T, et al. Upper-body morbidity following breast cancer treatment is common, may persist longer-term and adversely influences quality of life. Health Qual Life Outcomes [Internet]. 2010;8:92. Available from: **https://doi.org/10.1186/1477-7525-8-92**

[9] Beyaz SG, Ergönenç JŞ, Ergönenç T, Sönmez ÖU, et al. Postmastectomy painA Cross-sectional Study of Prevalence, Pain Characteristics, and Effects on Quality of Life. Chin Med J [Internet]. 2016;129(1):66-71. Available from: **https://doi.org/10.4103/0366-6999.172589**

[10] Boquiren VM, Hack TF, Thomas RL, Towers A, et al. A longitudinal analysis of chronic arm morbidity following breast cancer surgery. Breast Cancer Res Treat [Internet]. 2016;157(3):413-425. Available from: **https://doi.org/10.1007/s10549-016-3834-8**

[11] Crosbie J, Kilbreath SL, Dylke E, Refshauge KM, et al. Effects of Mastectomy on Shoulder and Spinal Kinematics During Bilateral Upper-Limb Movement. Phys Ther [Internet]. 2010;90(5):679-692. Available from: **https://doi.org/10.2522/ptj.20090104**

[12] Rietman JS, Dijkstra PU, Hoekstra HJ, Eisma WH, et al. Late morbidity after treatment of breast cancer in relation to daily activities and quality of life: A systematic review. Eur J Surg Oncol [Internet]. 2003;29(3):229-238. Available from: **https://doi.org/10.1053/ejso.2002.1403**

[13] Kärki A, Simonen R, Mälkiä E, Selfe J. Impairments, activity limitations and participation restrictions 6 and 12 months after breast cancer operation. J Rehabil Med [Internet]. 2005;37(3):180-188. Available from: **https://doi.org/10.1080/16501970410024181**

[14] Hayes SC, Johansson K, Stout NL, Prosnitz R, et al. Upper-body morbidity after breast cancer: Incidence and evidence for evaluation, prevention, and management within a prospective surveillance model of care. Cancer [Internet]. 2012;118(S8):2237-2249. Available from: **https://doi.org/10.1002/cncr.27467**

[15] Gong Y, Tan Q, Qin Q, Wei C. Prevalence of postmastectomy pain syndrome and associated risk factors: A large single-institution cohort study. Medicine (Baltimore) [Internet]. 2020;99(20):e19834. Available from: **https://doi.org/10.1097/MD.0000000000019834**

[16] Lee CH, Chung SY, Kim WY, Yang SN. Effect of breast cancer surgery on chest tightness and upper limb dysfunction. Medicine (Baltimore) [Internet]. 2019;98(19):e15524. Available from: **https://doi.org/10.1097/MD.0000000000015524**

[17] Yang EJ, Kwon YO. Changes in shoulder muscle activity pattern on surface electromyography after breast cancer surgery. J Surg Oncol [Internet]. 2018;117(2):116-123. Available from: **https://doi.org/10.1002/jso.24800**

[18] Shamley D, Lascurain-Aguirrebeña I, Oskrochi R. Clinical anatomy of the shoulder after treatment for breast cancer. Clin Anat [Internet]. 2014;27(3):467-477. Available from: **https://doi.org/10.1002/ca.22267**

[19] Shamley DR, Srinanaganathan R, Weatherall R, Oskrochi R, et al. Changes in shoulder muscle size and activity following treatment for breast cancer. Breast Cancer Res Treat [Internet]. 2007;10:19-27. Available from: **https://doi.org/10.1007/s10549-006-9466-7**

[20] Oskrochi G, Lesaffre E, Oskrochi Y, Shamley D. An Application of the Multivariate Linear Mixed Model to the Analysis of Shoulder Complexity in Breast Cancer Patients. Int J Environ Res Public Health [Internet]. 2016;13(3):274. Available from: **https://doi.org/10.3390/ijerph13030274**

[21] Prieto-Gómez V, Navarro-Brazález B, Sánchez-Méndez Ó, de-la-Villa P, et al. Electromyographic Analysis of Shoulder Neuromuscular Activity in Women Following Breast Cancer Treatment: A Cross-Sectional Descriptive Study. J Clin Med [Internet]. 2020;9(6):1804. Available from: **https://doi.org/10.3390/jcm9061804**

[22] Cheville AL, Troxel AB, Basford JR, Kornblith AB. Prevalence and Treatment Patterns of Physical Impairments in Patients With Metastatic Breast Cancer. J Clin Oncol [Internet]. 2008;26(16):2621-2629. Available from: **https://doi.org/10.1200/jco.2007.12.3075**

[23] Chrischilles EA, Riley D, Letuchy E, Koehler L, et al. Upper extremity disability and quality of life after breast cancer treatment in the Greater Plains Collaborative clinical research network. Breast Cancer Res Treat [Internet]. 2019;175:675-689. Available from: https://doi.org/10.1007/s10549-019-05184-1

[24] Hernanz F, Paz L, Jimeno J, Tolaretxipi E, et al. Patient-reported outcomes in breast conserving treatment. Information given by breast surgeon. What to improve. Rev Senol y Patol Mamar [Internet]. 2021; 34(2):122-124. Available from: https://doi.org/10.1016/j.senol.2020.04.003

[25] Shamley D, Srinaganathan R, Oskrochi R, Lascurain-Aguirrebeña I, et al. Three-dimensional scapulothoracic motion following treatment for breast cancer. Breast Cancer Res Treat [Internet]. 2009;118(2):315 Available from: https://doi.org/10.1007/s10549-008-0240-x

[26] Ribeiro IL, Camargo PR, Alburquerque-Sendín F, Ferrari AV, et al. Three-dimensional scapular kinematics, shoulder outcome measures and quality of life following treatment for breast cancer – A case control study. Musculoskelet Sci Pract [Internet]. 2019;40:72-79. Available from: https://doi.org/10.1016/j.msksp.2019.01.012

[27] Lang AE, Dickerson CR, Kim SY, Stobart J, et al. Impingement pain affects kinematics of breast cancer survivors in work-related functional tasks. Clin Biomech [Internet]. 2019;70:223-230. Available from: https://doi.org/10.1016/j.clinbiomech.2019.10.001

[28] Miguel-Andres I, Alonso-Rasgado T, Walmsley A, Watts AC. Effect of Anconeus Muscle Blocking on Elbow Kinematics: Electromyographic, Inertial Sensors and Finite Element Study. Ann Biomed Eng [Internet]. 2017;45(3):775-788. Available from: https://doi.org/10.1007/s10439-016-1715-2

[29] Brookham RL, Cudlip AC, Dickerson CR. Examining upper limb kinematics and dysfunction of breast cancer survivors in functional dynamic tasks. Clin Biomech [Internet]. 2018;55:86-93. Available from: https://doi.org/10.1016/j.clinbiomech.2018.04.010

[30] Akoochakian M, Davari HA, Alizadeh MH, Rahnama N. Evaluation of shoulder girdle strength more than 12 month after modified radical mastectomy and axillary nodes dissection. J Res Med Sci [Internet]. 2017;22(3):81. Available from: https://doi.org/10.4103/jrms.JRMS_649_16

[31] Bellavance EC, Kesmodel SB. Decision-Making in the Surgical Treatment of Breast Cancer: Factors Influencing Women's Choices for Mastectomy and Breast Conserving Surgery. Front Oncol [Internet]. 2016;6:74. Available from: https://doi.org/10.3389/fonc.2016.00074

[32] World Medical Association. World Medical Association Declaration of Helsinki: Ethical Principles for Medical Research Involving Human Subjects. JAMA [Internet]. 2013;310(20):2191-2194. Available from: https://doi.org/10.1001/jama.2013.281053

Biomechanics Assessment of Kinematic Parameters of Low-Sprint Start in High-Performance Athletes Using Three Dimensional Motion Capture System

Mirvana Elizabeth Gonzalez Macias[1] (ID) *, Carlos Villa Angulo[2]* (ID) *, Emilio Manuel Arrayales Millan[1]* (ID) *,*
Karla Raquel Keys Gonzalez[1] (ID)

[1]Laboratory Biomechanics, Faculty of Sports, Autonomous University of Baja California, Mexicali, B. C., México
[2]Laboratory of Bioinformatics and Biofotonics, Engineering Institute, Autonomous University of Baja California, Mexicali, B. C., México

ABSTRACT

In a sprint start, the athlete takes up a position with their hands just behind a line, arms vertical, feet generally placed about a shoe length apart, and the hips rising above the line of the head. Mistakes in this position influence the execution of the low-sprint start, and can drastically influence the initial running speed and acceleration achieved by the athlete. Common mistakes occur due to the misconception that athletes must also lean forward, bringing the shoulders ahead of their hands and putting pressure on them. A standard approach to identify sprint start mistakes is to use a stick or weighted string to drop down from the shoulders. The effective implementation of this approach depends on the coach's experience and remains a significant challenge. In this study, a three-dimensional motion capture system with the Vicon® Plug-in-Gait model was used to characterize the kinematic parameters that influence the execution of low-sprint start in six high-performance athletes. The main kinematic parameters are reaction time, stride length, and stride time. The obtained results demonstrate the potential utility of a three-dimensional motion capture system to assess the kinematic parameters of low-sprint start in high-performance athletes.

Corresponding author

TO: Mirvana Elizabeth Gonzalez Macias

INSTITUTION: Laboratory Biomechanics, Faculty of Sports, Autonomous University of Baja California

ADDRESS: Ave. Monclova S/N, Ex Ejido Coahuila, C. P. 21280, Mexicali, Baja California, México

CORREO ELECTRÓNICO: gonzalez.mirvana@uabc.edu.mx

INTRODUCTION

In the 100 m and 200 m sprint, the success of the sprint start performance depends on the capacity of the athlete to establish a large impulse over the shortest time, reaching the highest running speed as soon as possible [1] [2]. During this step, the sprinters take their positions at the blocks at the set command, and the mechanics of leaving the blocks at the sound of the gun strongly influences the acceleration at the start of a race [3] [4]. When a starter's command is given, the athlete takes up a position with their hands just behind the line, arms vertical, and feet generally placed about a shoe length apart. In the set position, the athlete understands that the hips should rise above the line of the head. The is a misconception that they must lean forward, bringing their shoulders ahead of their hands and putting pressure on them. This position influences the execution of the low-sprint start and can drastically influence the initial running speed and acceleration achieved by the athlete. This is because when the gun goes off, it becomes impossible for the athlete to instantly drive their arms forward or backward without first lifting them off the ground, and they can lose time in the process [5]. According to Schot PK and Knutzen KM, an efficient sprint start depends on the start block positioning and joint angles of the lower limbs in the position [6]. In addition, the pushing time on the blocks and the forces generated by the front and rear legs during the pushing phase depend on the reaction time, stride length, and stride time [7]. The average external power calculated based on horizontal motion and normalized to participant characteristics, provides a single measure that accounts for the change in velocity and the time taken to achieve this change [2]. However, this parameter is more commonly adopted for measurements during early and mid-acceleration after the low-sprint start process.

In practice, an efficient sprint start integrates temporal and spatial acyclic movements into a cyclic action, whose success depends on the athlete's ability and coach experience and is still a big challenge. Different authors have reported studies related to the optimal relationship between body position and initial acceleration. For example, Coh *et al.* reported the dependence of the angular velocity and maximal force of the sprinter during the start on the body positioning and associated start block settings [7]. Mero *et al.* found that block velocity is strongly correlated with the horizontal and vertical forces exerted on the front and rear starting blocks [8]. Gutierrez-Davila, and Prampero *et al.* reported biomechanical variables and their interdependencies with specific motor abilities, energy processes, anthropometric characteristics, and the central processes of motor regulation [9]. There are few previous, reports on the biomechanics of kinematic parameters such as reaction time, stride length, and stride time. All authors state that "a single optimal set position" for all athletes is not recommended because of varying physical factors; therefore, athletes must find their preferred distance between the blocks according to sensations or outcomes.

On the other hand, different technologies have been used to assess the kinematic parameters of sprint start in high-performance athletes. Bezodis *et al.* published in 2019 a clear review of the current biomechanics of track and field sprint starts that can be used to provide current recommendations for both researchers and practitioners [10]. Bezodis *et al.* proposed the use of a laser distance measurement (LDM) device to determine the measurement error in velocity data obtained during different phases of a maximal sprint, and consequently, to evaluate the usability of LDM devices to analyze the velocity profiles of sprinters [11]. Their results recommend that laser data should not be used during the first 5 m of a sprint and are likely to have limited use for assessing within-subject variation in performance during a single session. Bergamini *et al.* reported the use of a lower trunk-mounted inertial measurement unit (IMU) to identify consistent features in the waveforms of the signals

supplied by the IMU and estimate stance and stride duration during the maintenance phase of sprint running. Their results proved that the IMU is suitable for estimating stance and stride durations during sprint running, providing the opportunity to collect information in the field without constraining or limiting athletes' and coaches' activities [12]. Falbriard *et al.* reported the use of foot-worn inertial sensors to investigate different algorithms to detect initial contact (IC) and terminal contact (TC) from different features measured by foot-worn IMU kinematic signals and estimated the main inner-stride temporal parameters. The performance metrics (bias and precision) of each algorithm were assessed in comparison with a reference system (instrumented force plate treadmill), which allowed the validation of the inner-stride temporal parameters over a large number of steps and a large range of running speeds. Their results showed that running speed can significantly affect the estimation bias, suggesting that speed-dependent correction should be applied to improve the accuracy of the systems [13]. Seidl *et al.* reported the use of a radio-based local position measurement system, RedFIR (Grün *et al.*, 2011) to obtain spatio-temporal information during sprinting based on lightweight transmitters attached to the athletes. Based on their results, a methodology capable of automatically providing step length, step time, and ground contact time during sprinting was developed. Different transmitter positions were tested, and the accuracy of the derived spatiotemporal parameters was evaluated by comparing them to those from an optoelectronic system [14]. Nagahara *et al.* reported the use of two different global positioning system (GPS) units to obtain mechanical properties during sprint acceleration [15]. However, in their results, they remarked that for the current state of GPS devices' accuracy for speed–time measurements over a maximal sprint acceleration, it is recommended that radar, laser devices, and timing gates remain the reference methods for implementing the computation methods reported by Samozino *et al.*

[16]. Bergamini *et al.* validated an adapted sensor-fusion algorithm in a trunk-mounted IMU to estimate trunk inclination and angular velocity during sprint start. A Bland-Altman analysis was carried out using parameters extracted from the historical data of the estimated variables, and analysis of similar curves. Their results indicate agreement between the reference and IMU estimates, which opens a promising scenario for accurate in-field use of IMUs for sprint start performance assessment [17]. Di-Kiat *et al.* proposed the use of an optical motion capture system as a benchmark to validate a new approach for defining running gait. They presented a new gait event identification method, that uses foot acceleration to determine the foot-stroke (FS) and foot-off (FO) times. Temporal parameters such, as contact time and flight time can then be derived from this information [18]. This study also aimed to demonstrate that spatial parameters, such as running speed and stride length, can be estimated accurately using the method presented in [19]. However, most of the technologies described above are only applicable to one athlete, limited to straight runs, and need to be placed directly on the running track. This prohibits their use in competitions and runs including curved sections. Emergency three-dimensional (3D) kinematic analysis computer vision systems use hardware/software processing units with real-time optoelectronic video cameras to measure and quantitatively analyze 3D human segmental movement [20] [21]. Retro-reflective markers placed on the body surface are used to calculate with high precision of the body segments as well as the kinematic joints [22] [23]. The data obtained from these systems are clear and detailed, and the user is able to move freely because there are no cables attached to the computer. In addition, this allows movements in a large volume and observations of more users at one time [22] [23]. The major problem with these systems is the interference. Sometimes, the light reflected from a specific marker has insufficient intensity, which causes inaccuracy in the output. In

addition, the user can sometimes cover the markers, producing an occlusion effect on the camera, which causes inaccuracy of the output. Moreover, the system can be expensive depending on the required sensors, cameras, and software [24].

Although, most kinematic parameters can be obtained from measurements with floor sensors in combination with wearable sensors, no real-time calculations and visualization of 3D segmental movements can be performed. Hence, the aim of this study was to use the Vicon Plug-in-Gait model (Vicon®, Oxford, UK) to characterize the kinematic parameters that influence the execution of low-sprint start in six high-performance athletes [25]. The main kinematic parameters are reaction time, stride length, and stride time. Average external power was not considered in this study because vertical movement and vertical velocity play an important role in the low sprint-start process. The obtained results demonstrate the potential utility of the system in assessing the kinematic parameters of a low-sprint start.

MATERIALS AND METHODS

Participants

Six high-performance athletes, three women, and three men, who compete in 100 meters passing hurdles, were evaluated. All athletes wore tight training shorts, and the women wore a sports female bra. During testing, athletes wore the footwear that they used for competition. No accessories that hindered or introduced variations in athlete performance were permitted during testing. The demographic data (age, height, body mass) are as follows: (mean ±SD, age = 17 ± 2.09 years); the height of the athletes was measured with a wall stadiometer graduated in centimetres, presenting a scale from 0 to 250cm(SECA), without shoes, straight back, front view, (Height = 1.69 ± 0.06 m) and the body mass was obtained using the AMTI platform, (Body mass = 59.77 ± 6.65 kg).

Anthropometric dimensions were measured according to the provisions of the Vicon® Plug-in Gait product guide [25] as shown in Table 1. Flexible tape and Vernier tape were used for measurements. This study conformed to the recommendations of the Declaration of Helsinki and was approved by the research and postgraduate ethics and evaluation committee of the Faculty of Sports of the Autonomous University of Baja California, México.

TABLE 1. The averages of the anthropometric and demographic measures of the participants.

Variable	Male	Female
Age (years)	16 ± 1	18 ± 2.64
Height (m)	1.73 ± 0.02	1.66 ± 0.07
Body mass (kg)	61.56 ±3.17	57.97 ± 9.52
LPI (cm)	90.6 ± 6.03	86.53 ± 5.85
LPD (cm)	89.66 ± 5.57	86.76 ± 5.56
DRI (cm)	9.56 ± 0.47	8.6 ± 0.34
DRD (cm)	9.46 ± 0.55	8.63 ± 0.35
DTI (cm)	6.73 ± 0.35	6.7 ± 0.36
DTD (cm)	6.76 ± 0.46	6.86 ± 0.45
DHI (cm)	6.7 ± 0.52	5.26 ± 0.30
DHD (cm)	5.53 ± 0.57	5.3 ± 0.79
DCI (cm)	6.73 ± 0.057	5.76 ± 0.20
DCD (cm)	6.9 ± 0.10	5.96 ± 0.15
DMI (cm)	5.58 ± 0.27	4.73 ± 0.25
DMD (cm	5.56 ± 0.32	4.76 ± 0.11
EMI (cm)	2.73 ± 0.11	2.16 ± 0.1
EMD (cm)	2.7 ± 0.1	2.1 ± 0.1

LPI = Left Leg Length, LPD = Right Leg Length,
DRI = Left Knee Diameter, DRD = Right Knee Diameter,
DTI = Left Ankle Diameter, DTD = Right Ankle Diameter,
DHI = Left Shoulder Displacement, DHD = Right Shoulder
Displacement, DCI = Left Elbow Diameter,
DCD = Right Elbow Diameter, DMI = Left Wrist Diameter,
DMD = Right Wrist Diameter, EMI = Left hand Thickness,
EMD = Right Hand Thickness.

Marker placement and Motion Capture

The evaluations were performed at the Biomechanics Laboratory of the Faculty of Sports at the Autonomous University of Baja California, Mexico. 39 passive reflective markers, 24 mm in diameter, were placed on each

participant as shown in Figure 1. The position of each reflective marker followed the standard Plug-in-Gait model, as described in Table 2. To characterize complete body movement, the markers were divided into upper-body and lower-body markers. The upper body markers contained four head markers, two for the front side and two for the backside. The torso markers contained five markers, two for vertebrae, a clavicle marker, a sternum marker and a scapula marker. The arm markers contain a marker for the shoulder and, markers for the upper arms, elbow, forearm, wrist, and fingers. Similarly, the lower body markers contained five pelvis markers, two for the left anterior superior side and two for the right anterior superior side of the iliac spine. The leg contained five markers, a knee marker, thigh marker, ankle marker, and tibial marker. The foot contained a toe and heel marker.
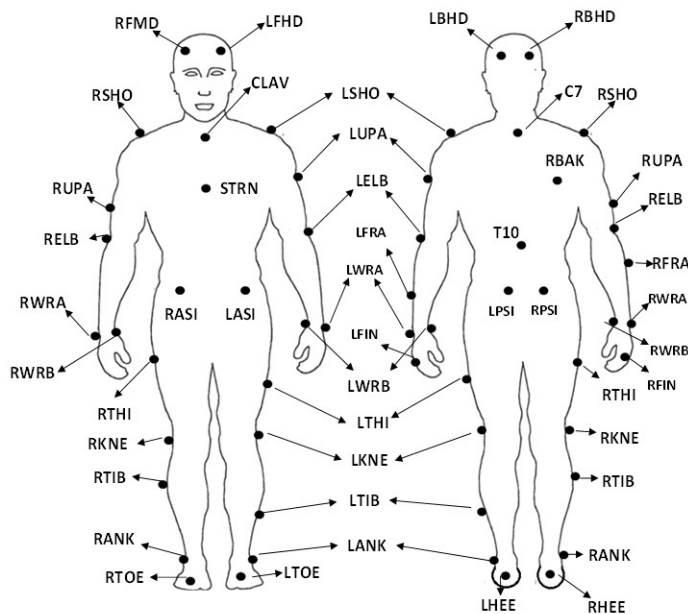
FIGURE 1. **Skeleton model illustrating the placement of the passive reflective markers (anterior and posterior view).**

The three-dimensional motion capture system used contained eleven optoelectronics infrared cameras (Bonita B10) up to one megapixel (1024 x 1024) high resolution, which accurately captures up to 0. 5 mm

for a 4 m x 4 m volume, with variable focal length, and speed of 250 frame rate (fps), and two video cameras (Bonita 720c) of a 1280 x 720 HD resolution, with an impressive 120 Hz fully synchronized frame rate. The cameras were distributed in the capture volume to measure all possible details in the athlete's movement in 3D. In addition, the system includes a Giganet camera switch (POE) in an Ethernet network, a Vicon lock for analog signal observation, a host PC with Vicon Nexus 2 software, and two force platforms at 1000 Hz (AMTI, Waterdown, MA, USA). Figure 2 illustrates the setup of the capture system. In addition, all demographic and anthropometric dimensions of the participants were captured using the Nexus 2 software.
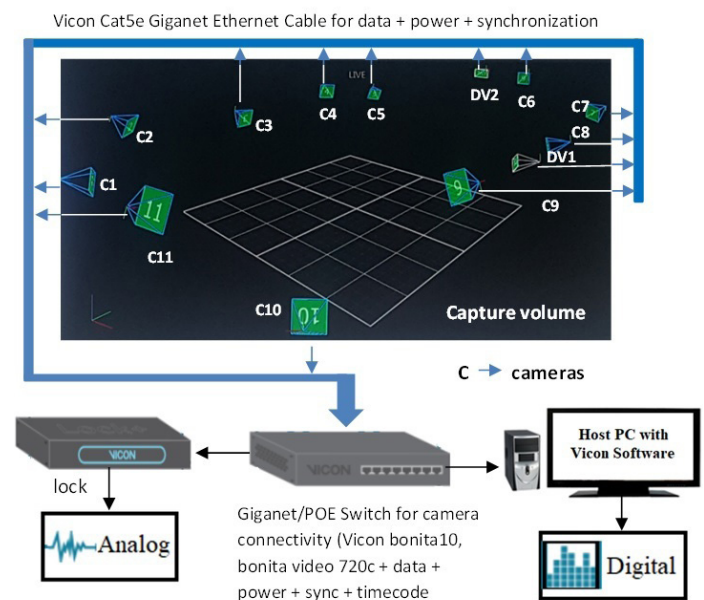
FIGURE 2. **Set-up of the athlete movement captures system.**

Figure 3 shows a general diagram of the Vicon Nexus 2 system. Before starting the test, it was necessary to calibrate the video and infrared cameras using the T-rod tool. The T-rod tool carries five LEDs, and this tool moves at the area work of 6 x 4m. Is was then necessary to place this at the origin point on the floor, according to the method described [25] in Figure 3(a).

TABLE 2. Plug-in-Gait model, markers placement.

Upper Body		
	Head Markers	
LFHD	Left front head	Located approximately over the left template
RFHD	Right front head	Located approximately over the right template
LBHD	Left-back head	Placed on the back of the head
RBHD	Right-back head	Placed on the back of the head
	Torso Markers	
C7	7th Cervical Vertebrae	Spinous process of the 7th cervical vertebrae
T10	10th Thoracic Vertebrae	Spinous process of the 10th thoracic vertebrae
CLAV	Clavicle	Jugular Notch where the clavicles meet the sternum
STRN	Sternum	Xiphoid process of the Sternum
RBAK	Right Back	Placed in the middle of the right scapula
	Arms Markers	
LSHO	Left shoulder marker	Placed on the Acromio-clavicular joint
LUPA	Left upper arm marker	Placed on the upper arm
LELB	Left elbow	Placed on the lateral epicondyle
LFRA	Left forearm marker	Placed on the lower arm
LWRA	Left wrist marker A	Left wrist bar thumb side
LWRB	Left wrist marker B	Left wrist bar pinkie side
LFIN	Left fingers	Placed on the dorsum of the hand
RSHO	Right shoulder marker	Placed on the Acromio-clavicular joint
RUPA	Right upper arm marker	On the lateral area in the lower third of the arm
RELB	Right elbow	On the lateral epicondyle
RFRA	Right forearm marker	On the lateral area in the upper third of the forearm
RWRA	Right wrist marker A	Next to the thumb on the wrist
RWRB	Right wrist marker B	Next to the pinky on the wrist
RFIN	Right fingers	Placed on the dorsum of the hand
Lower Body		
	Pelvis	
LASI	Left ASIS	Placed directly over the left anterior superior iliac spine
RASI	Right ASIS	Placed directly over the right anterior superior iliac spine
LPSI	Left PSIS	Placed directly over the left posterior superior iliac spine
RPSI	Right PSIS	Placed directly over the right posterior superior iliac spine
	Leg Markers	
LKNE	Left knee	Placed on the lateral epicondyle of the left knee
LTHI	Left thigh	Placed over the lower lateral 1/3 surface of the thigh
LANK	Left ankle	Placed on the lateral malleolus along an imaginary line that passes through the transmalleolar axis.
LTIB	Left tibial wand marker	Similar to the thigh markers, these are placed over the lower 1/3 of the shank to determine the alignment of the ankle flexion axis
RKNE	Right knee	Placed on the lateral epicondyle of the right knee
RTHI	Right thigh	Placed on the upper lateral 1/3 surface of the thigh
RANK	Right ankle	Placed on the lateral malleolus along an imaginary line that passes through the transmalleolar axis.
RTIB	Right tibial wand marker	Placed on the upper 1/3 of the lateral surface of the stem
	Foot Markers	
LTOE	Left toe	Placed over the second metatarsal head, on the mid-foot side of the equinus break between fore-foot and mid-foot
LHEE	Left heel	Placed on the calcaneous at the same height above the plantar surface of the foot as the toe marker
RTOE	Right toe	Placed over the second metatarsal head, on the mid-foot side of the equinus break between fore-foot and mid-foot
RHEE	Right heel	Placed on the calcaneous at the same height above the plantar surface of the foot as the toe marker

When the markers were placed, the athlete was notified to enter into a static position, as shown in Figure 3(b), to perform static capture. The system then detected the markers, as shown in Figure 3(c), and performed the reconstruction model, as shown in Figure 3(d). Once the reconstruction model was obtained, the athlete performed the movement, and the trajectories of the markers were labeled and filtered using a Butterworth low-pass filter with a frequency of 100Hz.
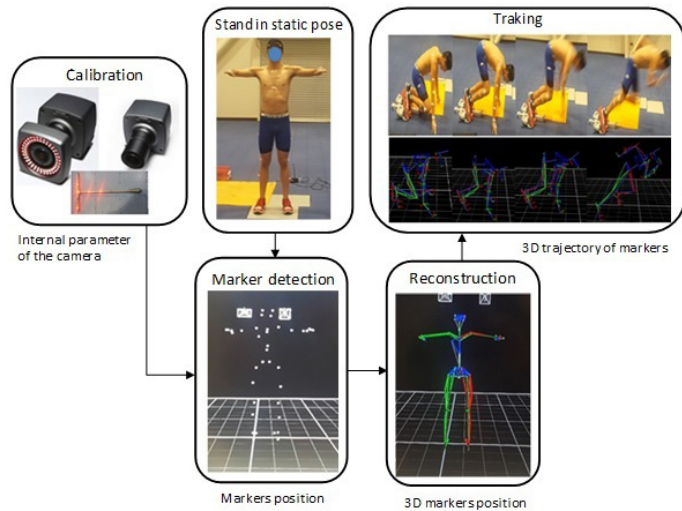

FIGURE 3. The general operation of the system. (a) Calibration of the cameras (b) athlete static starting position (c) markers detectio (d) Reconstruction 3D markers.

Description of the applied exercise

In this study, the reaction time (RT) is defined as the time between the sound emitted by the timing system and the time the foot of the athlete leaves the starting block. The wireless Brower Timing Systems TS-T17 was used to measure the RT. To avoid the risk of injury and achieve maximum performance, the athletes realized a standardized dynamic warm-up before the tests. To capture the movement of the athletes during the start of running three critical steps were performed. The first step is positioning the athlete at the starting block. Once the athlete is placed in the correct

position, the athlete hears the first beep emitted by the Brower Timing Systems, which means being prepared. The second step is when a second beep is emitted, which indicates being ready for the athlete, and the third step is when a third beep is emitted and the start is executed, as shown in Figure 4. Once the start is executed, the RT is obtained, the first impact of the reaction force from the ground in three steps 1) moment of release of the foot from the block, 2) maximum extension of the leg behind and 3) the first contact of the foot with the ground. At that moment, the stride length and stride time were determined by the motion capture system.
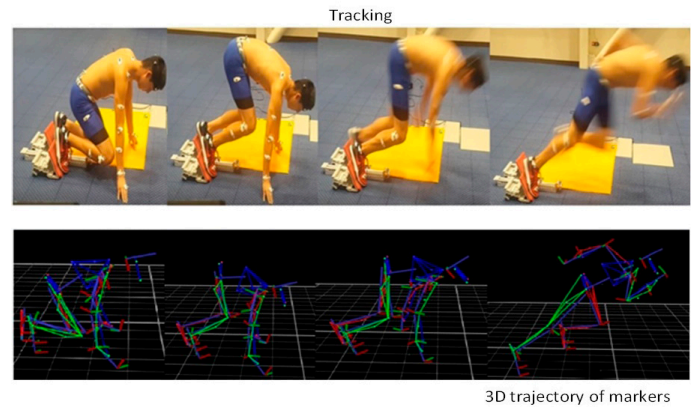
FIGURE 4. The capture of 3D trajectory of markers in the system.

Data processing

The 3D trajectories of the passive reflective markers were corrected using a low pass filter (100Hz Butterworth filter) and then imported into Matlab R2019b (The MathWorks, Inc).

Stride length

Stride length is the distance from the point where the toe leaves the starting block until it touches the ground again (after the swing phase). The TOE marker was used to calculate stride length using equation (1) [26].

$$L = \sqrt{(X_{end} - X_{start})^2 + (Y_{end} - Y_{start})^2 + (Z_{end} - Z_{start})^2} \tag{1}$$

$$T = (0.01 \times N_F)$$

where L is the stride length.

Stride time

Stride time was calculated using the total number of frames and the elapsed time between frames. The square where the foot takes off is considered to be the square with which it first impacts the ground. In this case, the time between frames is 0.01 s. Therefore, it was calculated using equation (2) as follows [26].

$$T = \left(0.01 \times N_F\right) \qquad (2)$$

Where T is the stride time and NF is the number of frames.

Statistical analysis

R software was used for statistical analysis [27]. Descriptive statistics (mean ± SD) were determined for each variable. The Shapiro-Wilk test was applied because the sample size was less than fifty which complies with the normal principle (p> 0.05). In this sense, the parametric test was used, the Student's t-test was used for independent samples.

RESULTS AND DISCUSSION

Table 3 shows the results of the three variables evaluated in men. In this group, M1 obtained the shortest reaction time of 0.19 s and a stride length of 1.36 m with the right leg behind, while with the left leg behind, which is the leg that normally performs the

TABLE 3. Obtained results of the 3 evaluated variables for male.

Participant	Reaction time (LLB)	Stride length (m)	Stride time (S)	Reaction time (RLB)	Stride right (m)	Stride time (S)
M1	0.32	1.357	0.34	0.19	1.369	0.36
M1	0.32	1.120	0.34	0.19	1.130	0.36
M1	0.35	1.070	0.37	0.20	1.140	0.38
M2	0.28	0.950	0.28	0.30	1.074	0.30
M2	0.30	1.020	0.32	0.32	1.070	0.30
M2	0.28	0.950	0.29	0.31	1.100	0.34
M3	0.23	1.227	0.31	0.28	1.264	0.28
M3	0.23	1.120	0.30	0.28	1.020	0.27
M3	0.25	1.100	0.30	0.30	1.120	0.30

TABLE 4. Obtained results of the 3 evaluated variables for female.

Participant	Reaction time (LLB)	Stride length (m)	Stride time (S)	Reaction time (RLB)	Stride right (m)	Stride time (S)
F1	0.34	1.010	0.32	0.32	0.870	0.30
F1	0.36	1.100	0.35	0.35	1.010	0.30
F1	0.24	1.110	0.32	0.32	1.047	0.31
F2	0.25	1.115	0.28	0.28	1.106	0.32
F2	0.25	1.110	0.27	0.27	1.010	0.33
F2	0.25	0.980	0.28	0.28	1.080	0.33
F3	0.25	1.100	0.34	0.27	1.010	0.33
F3	0.25	1.200	0.34	0.26	1.288	0.31
F3	0.25	0.980	0.33	0.26	1.080	0.30

Variable	Participants	Mean	SD

Reaction time (LLB)	Stride length (m)	Stride time (S)	Reaction time (RLB)	Stride right (m)	Stride time (S)
0.32	1.157	0.34	0.18	1.369	0.36
0.32	1.120	0.34	0.19	1.130	0.36
0.35	1.070	0.37	0.20	1.140	0.38
0.28	0.950	0.28	0.30	1.074	0.30
0.30	1.020	0.32	0.32	1.070	0.30
0.28	0.950	0.29	0.31	1.100	0.34
0.23	1.227	0.31	0.28	1.264	0.27
0.23	1.120	0.30	0.28	1.020	0.30
0.25	1.100	0.30	0.30	1.120	0.30

Reaction time (LLB)	Stride length (m)	Stride time (S)	Reaction time (RLB)	Stride right (m)	Stride time (S)
0.34	1.010	0.32	0.32	0.870	0.36
0.36	1.100	0.35	0.35	1.010	0.30
0.24	1.110	0.32	0.32	1.047	0.30
0.25	1.115	0.28	0.28	1.106	0.31
0.25	1.110	0.27	0.27	1.010	0.32
0.23	0.980	0.28	0.28	8.080	0.33
0.25	1.100	0.34	0.27	1.010	0.53
0.25	1.200	0.34	0.26	1.288	0.35
0.25	0.980	0.33	0.26	1.080	0.30

start; he obtained the longest reaction time of 0.32s. Besides, the group of men obtained a mean of 0.276 with a standard deviation of 0.04 in reaction time using the left leg behind while a mean of 0.256 with a standard deviation of 0.05 in reaction time was obtained with the right leg behind. Similarly, Table 4 shows the results of the 3 variables evaluated in women. In this group, F1 obtained the best reaction time of 0.24s and a stride length of 1.11 m with the left leg behind, while with the left leg behind, which is not the leg that normally performs the start, she obtained the longest reaction time of 0.32s. In addition, the group of women obtained a mean of 0.28 with a standard deviation of 0.05 in reaction time using the left leg behind while a mean of 0.263 with a standard deviation of 0.03 in reaction time was obtained using the right leg behind. From Tables 3 and 4, it is observed that men performed better in reaction times, as well as greater stride length than to women. Table 5 presents the descriptive statistics of each variable evaluated in men and women.

TABLE 5. Descriptive statistics for each variable evaluated.

Variable	Participants	Mean	SD
Reaction Time (LLB)	Male	.28	.046
	Female	.27	.036
Stride length (m)	Male	1.10	.112
	Female	1.07	.013
Stride time (S)	Male	.31	.029
	Female	.31	.032
Reaction time (RLB)	Male	.26	.061
	Female	.29	.035
Stride right (m)	Male	1.14	.066
	Female	1.05	.075
Stride time (S)	Male	0.32	0.42
	Female	0.31	0.12

The Student's t-test for independent samples indicates that Ho is acceptable, that is, there are no significant differences between men and women.

Table 6 shows the results obtained from the Student´s T-test, degrees of freedom, and p-values >0.05.

TABLE 6. Independent samples of Student´s t-test results.

Variable	t	gl	p
Reaction Time (LLB)	.401	4	.709
Stride length (m)	.357	4	.739
Stride time (S)	.079	4	.941
Reaction time (RLB)	-.647	4	.553
Stride right (m)	1.506	4	.207
Stride time (S)	.261	4	.807

Figure 5 shows the left toe speed obtained for the male and female participants. It is observed that all participants reached their highest left toe speed between 13 and 20 s. It is also observed that male participants (M2) reached the highest speed of 7.5 m/s at 16s while the female participants (F3) reached the lowest speed of 7.1 m/s at 18 s.
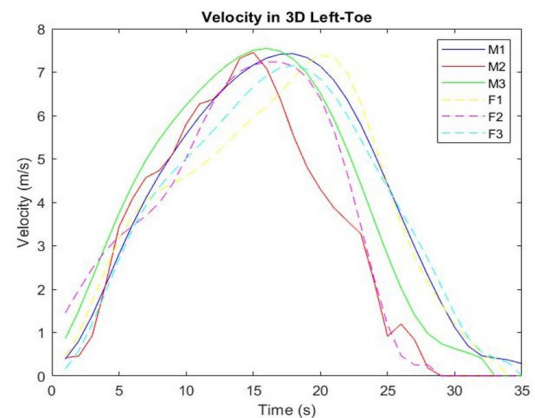

FIGURE 5. Speed obtained for male and female participants on the left-toe.

Similarly, Figure 6 shows the right-toe speed obtained for male and female participants.

It is observed that the participants reached the highest speed on the right toe between 15 and 25 s. It is also observed that male (M2) reached the highest speed of
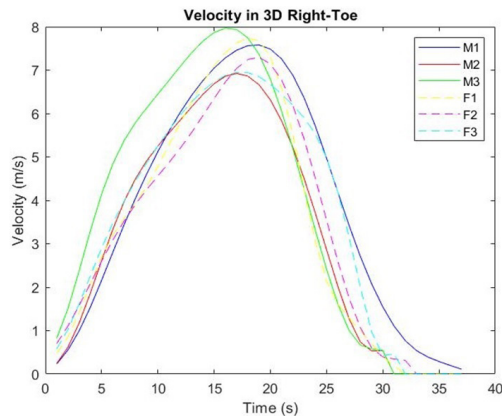
Speeds were obtained for male and female participants on the right-toe.

7.96 m/s at 16 s while the male (M1) reached the lowest speed of 6.9 m/s at 17 s. Besides, the female participant (F3) obtained the lowest speed of 6.9 m/s at 17 s while the participant (F1) obtained the maximum speed of 7.7 m/s at 18 s. From Figure 5 and Figure 6 it is observed that the best speeds are obtained on the right toe, which is in contrast with the common practice that indicates the left toe behind is the toe that participants normally perform the start.

In this study, the Helen-Hayes PGM for snatch output motion analysis was used to determine the reaction time, stride length, and stride time of both legs of the six athletes. The Vicon® Plug-in-Gait model (PGM) is one of the most widely used models for evaluating different kinematic and kinetic parameters of different motor or sports gestures [28] [29] [30]. Remi K. reported that stride length, determined when the rear leg moves forward in the frontal plane, ranges from 100 to 120 cm [31]. Considering this range, in the group of men, (M2) in two of the three repetitions of the left leg behind, obtained 0.950 m, while with the right leg behind, all values were within the range. In the group of women (F2) and (F3) with the left leg behind in the last repetition did not obtain (100-120cm). With respect to the right leg behind (F1) was the only one, where the value was not within the reported Remi K. range.

Slawinski J *et al*. used an optoelectronic motion analysis system containing 12 digital cameras (250 Hz) to characterize four repetitions of sprint snatches of six elite sprinters and six well-trained sprinters. The average RT of the elite sprinters was 0.151 ± 0.016 s, and that of the six well-trained sprinters was 0.158 ± 0.033 s [32].

In comparison with the results obtained by Slawinski J *et al*., the sprinters characterized in this study obtained a higher performance. For three repetitions, they obtained an average RT of 0.2767 ± 0.045 s using the right leg back, and an average RT of 0.2778 ± 0.042 s using the left leg back. There is a difference in their RT averages, however, it is not significant considering that they are elite and well-trained sprinters. Despite the small sample size, this study aimed to characterize the snatch output, using a motion analysis system, and make pertinent corrections to obtain the RT, stride length, and stride time for each leg of the athletes.

CONCLUSIONS

In this study, a 3D motion capture system was used to characterize the kinematic parameters that influence the execution of a low-sprint start in high-performance athletes. The Vicon 3D capture system is precise and highly accurate for performing biomechanical evaluations of body motor gestures. The high reliability obtained data is not just empirical, but also numerical ones. Although a small number of samples were used, the results provide evidence of the effectiveness of using 3D capture technology to quantify kinematic parameters of low-sprint starts. The characterized kinematic parameters can be used to identify improvements for the athlete, such as errors in the execution of the start to avoid possible injuries in the athlete. The Student's t-test for independent samples indicates that Ho is accepted, and there are no significant differences between men and women (p-value > 0.05), for all the variables. However, with this technology, it was found that three athletes obtained better times with the nondominant leg. In addition, this study illustrated the importance of

coaches and the athletes understanding of the use of 3D motion capture system technology and its scope. This technology can be part of their evaluations to avoid possible injuries, detect errors in the execution of precision movements, and improve performance.

ETHICAL STATEMENT

The present study followed the ethical principles regarding human experimentation proposed by the Helsinki declaration; all the subjects provided a written consent in order to participate in the study, that was approved by the research and postgraduate ethics and evaluation committee of the Faculty of Sports of the Autonomous University of Baja California, México. Protocol #149/2569.

AUTHOR CONTRIBUTIONS

M.E.G.M performed data curation, designed, and developed methodology, applied techniques to analyze or synthesize data, validated and tested the models employed, oversaw implementation of software for biomechanical analysis, elaborated images, carried out statistical analysis, provided material and computer resources, and participated in all the writing stages of the manuscript. C.V.A oversaw the development of the methodology, validated the models employed, participated in the writing of the manuscript, and reviewed and edited the final version. E.M.A.M performed data curation, analyzed data, and implemented software for data analysis. K.R.K.G. performed data curation and implemented software for data analysis. All authors conceptualized the project, reviewed and approved the final version of the manuscript.

ACKNOWLEDGMENTS

CONFLICTS OF INTEREST

The authors do not report any conflict of interest.

REFERENCES

[1]   Fortier S, Basset FA, Mbourou G, Favérial J, Teasdale N. Starting block performance in sprinters: A statistical method for identifying discriminative parameters of the performance and an analysis of the effect of providing feedback over a 6-week period. J Sport Sci Med [Internet]. 2005;4(2):134-143. Available from: *https://www.jssm.org/jssm-04-134.xml%3EFulltext#*

[2]   Bezodis NE, Salo AI, Trewartha G. Choice of sprint start performance measure affects the performance-based ranking within a group of sprinters: Which is the most appropriate measure? Sports Biomech [Internet]. 2010;9(4):258-269. Available from: **https://doi.org/10.1080/14763141.2010.538713**

[3]   Guissard N, Duchateau J, Hainaut K.. EMG and mechanical changes during sprint starts at different front block obliquities. Med Sci Sports Exerc [Internet]. 1992;24(11):1257-1263. Available from: *https://journals.lww.com/acsm-msse/Abstract/1992/11000/EMG%20 and%20mechanical%20changes%20during%20sprint%20starts%20 at.10.aspx*

[4]   Slawinski J, Dumas R, Cheze L, Ontanon G, et al. 3D Kinematic of Bunched, Medium and Elongated Sprint Start. Int J Sports Med [Internet]. 2012;33(7):555-560. Available from: **https://doi.org/10.1055/s-0032-1304587**

[5]   Theophilos P, Nikolaos M, Kiriakos A, Athanasia S, et al. Evaluation of sprinting performance in adolescent athletes with running shoes, spikes and barefoot. J Phys Educ Sport [Internet]. 2014;14(4):593-598. Available from: **http://dx.doi.org/10.7752/jpes.2014.04092**

[6]   Schot PK, Knutzen KM. A Biomechanical Analysis of Four Sprint Start Positions. Res Q Exerc Sport [Internet]. 1992;63(2):137-147. Available from: **https://doi.org/10.1080/02701367.1992.10607573**

[7]   Čoh M, Peharec S, Bačić P, Mackala K. Biomechanical Differences in the Sprint Start between Faster and Slower High-Level Sprinters. J Hum Kinet [Internet]. 2017;56(1):29-38. Available from: **https://dx.doi.org/10.1515%2Fhukin-2017-0020**

[8]   Mero A, Komi PV, Gregor RJ. Biomechanics of Sprint Running. Sports Med [Internet]. 1992;13(6):376-392. Available from: **https://doi.org/10.2165/00007256-199213060-00002**

[9]   Gutiérrez-Dávila M, Dapena J, Campos J. The Effect of Muscular Pre-Tensing on the Sprint Start. J Appl Biomech [Internet]. 2006;22(3):194-201. Available from: **https://doi.org/10.1123/jab.22.3.194**

[10]   Bezodis NE, Willwacher S, Salo AIT. The Biomechanics of the Track and Field Sprint Start: A Narrative Review. Sports Med [Internet]. 2019;49(9):1345-1364. Available from: **https://doi.org/10.1007/s40279-019-01138-1**

[11]   Bezodis NE, Salo AIT, Trewartha G. Measurement Error in Estimates of Sprint Velocity from a Laser Displacemeny Measurement Device. Int J Med [Internet]. 2012;33(6):439-444. Available from: **https://doi.org/10.1055/s-0031-1301313**

[12]   Bergamini P, Picerno P, Pillet H, Natta F, et al. Estimation of temporal parameters during sprint running using a trunk-mounted inertial measurement unit. J Biomech [Internet]. 2012;45(6):1123-1126. Available from: **https://doi.org/10.1016/j.jbiomech.2011.12.020**

[13]   Falbriard M, Meyer F, Mariani B, Millet GP, et al. Accurate Estimation of Running Temporal Parameters Using Foot-Worn Inertial Sensors. Front Physiol [Internet]. 2018;9:610. Available from: **https://dx.doi.org/10.3389%2Ffphys.2018.00610**

[14]   Seidl T, Linke D, Lames M. Estimation and validation of spatio-temporal parameters for sprint running using a radio-based tracking system. J Biomech [Internet]. 2017;65:89-95. Available from: **https://doi.org/10.1016/j.jbiomech.2017.10.003**

[15]   Nagahara R, Botter A, Rejc E, Koido M, et al. Concurrent Validity of GPS for Deriving Mechanical Properties of Sprint Acceleration. Int J Sports Physiol Perform [Internet]. 2017;12(1):129-132. Available from: **https://doi.org/10.1123/ijspp.2015-0566**

[16]   Samozino P, Rabita G, Dorel S, Slawinski J, et al. A simple method for measuring power, force, velocity properties, and mechanical effectiveness in sprint running. Scand J Med Sci Sports [Internet]. 2016;26(6):648-658. Available from: **https://doi.org/10.1111/sms.12490**

[17]   Bergamini E, Guillon P, Camomilla V, Pillet H, et al. Trunk Inclination Estimate During the Sprint Start Using an Inertial Measurement Unit: A Validation Study. J Appl Biomech [Internet]. 2013;29(5):622-627. Available from: **https://doi.org/10.1123/jab.29.5.622**

[18]   Chew D-K, Ngoh KJH, Gouwanda D, Gopalai AA. Estimating running spatial and temporal parameters using an inertial sensor. Sports Eng [Internet]. 2018;21:115-122. Available from: **https://doi.org/10.1007/s12283-017-0255-9**

[19]   Yang S, Mohr C, Li Q. Ambulatory running speed estimation using an inertial sensor. Gait Posture [Internet]. 2011;34(4):462-466. Available from: **https://doi.org/10.1016/j.gaitpost.2011.06.019**

[20]   Savoie P, Cameron JAD, Kaye ME, Scheme EJ. Automation of the Timed-Up-and-Go Test Using a Conventional Video Camera. IEEE J Biomed Health Inform [Internet]. 2020;24(4):1196-205. Available from: **https://doi.org/10.1109/jbhi.2019.2934342**

[21]   Thomas G, Gade R, Moeslund TB, Carr P, et al. Computer vision for sports: Current applications and research topics. Comput Vis Image Underst [Internet]. 2017;159:3-18. Available from: **https://doi.org/10.1016/j.cviu.2017.04.011**

[22]   Begon M, Colloud F, Fohanno V, Bahuaud P, et al. Computation of the 3D kinematics in a global frame over a 40 m-long pathway using a rolling motion analysis system. J Biomech [Internet]. 2009;42(16):2649-2653. Available from: **10.1016/j.jbiomech.2009.08.020**

[23]   Bernardina GRD, Monnet T, Pinto HT, de Barros RML, et al. Are Action Sport Cameras Accurate Enough for 3D Motion Analysis? A Comparison With a Commercial Motion Capture System. J Appl Biomech [Internet]. 2019;35(1):80-86. Available from: **https://doi.org/10.1123/jab.2017-0101**

[24]   Guerra-Filho G. Optical Motion Capture: Theory and Implementation. Theor App Inform. 2005;12:61-90.

[25]   Vicon. Plug-In Gait modelling instructions. Vicon® Manual, Vicon® Motion Systems [Internet]. Oxford Metrics Ltd; 2002. Available from: *https://www.vicon.com/software/oxford-foot-model/*

[26] Arellano-González JC, Medellin-Castillo HI, Cardenas-Galindo JA. Analysis of the kinematic variation of human gait under different walking conditions using computer vision. Rev Mex Ing Biomed [Internet]. 2017;38(2):437-457. Available from: **https://doi.org/10.17488/rmib.38.2.2**

[27] GNU. The R Project for Statistical Computing [Internet]. R;2016. Available from: *https://www.R-project.org/*

[28] Nair SP, Gibbs S, Arnold G, Abboud R, et al. A method to calculate the centre of the ankle joint: A comparison with the Vicon® Plug-in-Gait model. Clin Biomech [Internet]. 2010;25(6):582-587. Available from: **https://doi.org/10.1016/j.clinbiomech.2010.03.004**

[29] Khamis S, Danino B, Springer S, Ovadia D, et al. Detecting Anatomical Leg Length Discrepancy Using the Plug-in-Gait Model. Appl Sci [Internet]. 2017;7(9):926. Available from: **https://doi.org/10.3390/app7090926**

[30] Duffell LD, Hope N, McGregor AH. Comparison of kinematic and kinetic parameters calculated using a clusterbased model and Vicon's plug-in gait. Proc Inst Mech Eng H [Internet]. 2014;228(2):206-210. Available from: **https://doi.org/10.1177/0954411913518747**

[31] Korchemny R. A new concept for sprint start and acceleration training. New Stud Athl [Internet]. 1992;7(4):65-72. Available from: *http://centrostudilombardia.com/wp-content/uploads/IAAF-Corsa-Velocita/1992-A-new-concept-for-sprint-start-and-acceleration-training.pdf*

[32] Slawinski J, Bonnefoy A, Levêque J-M, Ontanon G, et al. Kinematic and Kinetic Comparisons of Elite and Well-Trained Sprinters During Sprint Start. J Strength Cond Res [Internet]. 2010;24(4):896-905. Available from: **https://doi.org/10.1519/jsc.0b013e3181ad3448**